

# Extended fully coupled analysis of consolidation using the finite element method

**Doctoral Dissertation**

Doctoral thesis approved in fulfillment of the requirements  
for the degree of Doktor-Ingenieur (Dr.-Ing.)  
at the  
Department of Material and Earth Sciences,  
Technische Universität Darmstadt



TECHNISCHE  
UNIVERSITÄT  
DARMSTADT

Submitted by  
Hung Tien Pham, MSc  
born on 20. July, 1988 in Hai Duong, Vietnam

Date of submission: 19.12.2019  
Date of defence: 29.01.2020

Supervisor Prof. Dr. Ingo Sass  
Co-supervisor PD Dr. Wolfram Rühaak

Darmstadt 2020

Pham, Hung Tien: Extended fully coupled analysis of consolidation using the finite element method

Thesis written in: Darmstadt, Technische Universität Darmstadt

Year thesis published in TUprints 2020

Date of the viva voce: 29.01.2020

Published under CC BY-SA 4.0 International

<https://creativecommons.org/licenses/>

---

## Board of examiners

**Head:** Prof. Dr. Rafael Ferreiro Mählmann

**Supervisor:** Prof. Dr Ingo Sass

**Co-supervisor:** PD Dr. Wolfram Rühaak

**Examiner:** Prof. Dr.-Ing. Hauke Zachert

**Examiner:** Prof. Dr. Andreas Henk

---



---

---

## **Declaration**

---

I hereby declare that this presented dissertation is based on original research, and is the result of my own work. It has not been submitted for any other degree in my name, to any other university or institution. The dissertation contains no material previously published or written by another person, except for references that are cited.

Darmstadt, December 2019

---



---

*To*  
*Hai Yen and Hai Minh*

*“The real world needs simple, cheap, and robust geotechnical technologies to be applied in large infrastructural projects.”- Jaroslaw Rybak*

---



---

## Abstract

---

The thesis focuses on consolidation analysis using the poroelasticity theory, or Biot's theory. It is written with a cumulative form including three research publications. The first two chapters of the thesis introduce briefly the topic, the poroelasticity theory, and finite element codes.

Chapter 3 presents a fully coupled plug-in for FEFLOW software that aims to analyse land subsidence problem due to groundwater extraction. The plug-in was developed using the C++ programming language with FEFLOW APIs and Qt IDE. It is distributed freely on GitHub. Two techniques were used to increase the speed of the plug-in. First, the boundary conditions are applied for local stiffness matrices before they are assembled to the global stiffness matrix. Second, the global stiffness matrix is assembled using multicores of the central processing unit (CPU).

Chapter 4 proposes a new approach to process data from the constant rate of strain test (CRST) for consolidation analysis. Instead of plotting test data on  $e$ - $\log(\sigma')$  graph (where  $e$  is the void ratio and  $\sigma'$  is the effective stress) to obtain the compression index  $C_c$  and the compression index  $C_r$ , the back-analysis method is used to obtain stress-dependent parameters for finite element models based on Biot's theory. An open-source software called CONAXIS was developed for this purpose. Codes and algorithms for CONAXIS were partly taken from previous FEFLOW plug-in. The proposed approach was compared with a commercial software named PLAXIS and was verified with data of two soft soil improvement projects in Mekong Delta, Vietnam. Both projects used prefabricated vertical drains (PVD) combining with surcharge loading and vacuum pumping as the improvement method. Each PVD has an influence zone that is idealised as a cylinder called a unit cell. Consolidation analyses for both projects were performed with axisymmetric models of unit cells in CONAXIS. In the first project, nine CRSTs from the same borehole with various depth were used to set up the model in CONAXIS. The soft soil thickness was 17.5 m. For the second project, six CRSTs from three boreholes were used, and the thickness of soft soils was about 35.0 m. Model results from CONAXIS were compared to field monitoring data. Both models showed a good agreement with field data.

Finally, chapter 5 deals with radial flows in 3D models of PVD systems. To capture radial flows around PVDs, finite element meshes around PVDs must be discrete with small element sizes that lead to a heavy computational effort, especially for 3D models. A new approach based on Vimoke-Taylor concept was proposed to overcome this difficulty. Instead of modelling both the PVD boundary and the smear-zone around PVD, a drained-zone was used to represent both PVD and the smear-zone. The horizontal hydraulic conductivity of the drained-zone was modified with a correction factor that was determined by fitting numerical results with analytical solutions of the unit cell. Factors related to characteristics of PVDs and soils affecting the correction factor  $C_d$  were investigated with six patch tests. The results of the patch tests indicate that the  $C_d$  value depends mainly on three factors: the size of the drained-zone, the size of the PVD and the smear-zone, and the mesh characteristic of the drained-zone. When one of these factors changes,  $C_d$  must be recalculated. Conversely,  $C_d$  is not affected by changes in the soil properties and the discharge capacity of the PVD.

---

---

## Preface

---

Consolidation analysis of saturated porous media can be categorised into three main groups:

- (1) Investigate subsidence problems related to fluid withdrawal
- (2) Design of soft soil improvement
- (3) Examination of waste material consolidation by own weight (such as dredged materials, mine tailings, waste sludge, and slurry).

This dissertation focuses on aspects to improve fully coupled models for consolidation analysis using Biot's theory (i.e. poroelasticity theory) with the small strain assumption (E. Detournay & A. H. D. Cheng, 1993). Hence, self-weight consolidation of soft soils, which have very high void ratios and large deformation, is not the subject of this dissertation. Instead, for such type of materials, the nonlinear consolidation theory is commonly used (Been & Sills, 1981; Radhika, Krishnamoorthy, & Rao, 2017).

The dissertation is written in a cumulative form including three peer-reviewed publications given herein in as chapters 3, 4 and 5. Each chapter has its own introduction, methodology and results. Each of these chapters contains the unchanged content of the original publication. Hence, chapter 1 is a brief introduction that aims to introduce the topic. Chapter 2 provides more details about Biot's theory and verifications of finite element codes used in three later chapters.

- Chapter 3: Pham, H.T., R uhaak, W., Schuster, V., Sass, I., 2019. *Fully hydro-mechanical coupled Plug-in (SUB+) in FEFLOW for analysis of land subsidence due to groundwater extraction*. *SoftwareX* 9, 15-19
- Chapter 4: Pham, H.T., R uhaak, W., Nguyen, O.C., Ngo, D.H., Sass, I., 2019. *Fully coupled analysis of consolidation by prefabricated vertical drains with applications of constant strain rate tests: case studies and open-source program*. *Geotextiles and Geomembranes*. doi:<https://doi.org/10.1016/j.geotexmem.2019.12.009>
- Chapter 5: Pham, H.T., R uhaak, W., Schulte, D., Sass, I., 2019. *Application of the Vimoke–Taylor concept for fully coupled models of consolidation by prefabricated vertical drains*. *Computers and Geotechnics* 116, 103201

As shown in Figure 1, chapter 3 presents code development for a fully hydro-mechanical coupled plugin for FEFLOW based on Biot's theory. The application is feasible for analysis of land subsidence triggered by artificial or natural pore water pressure decrease. Codes and algorithms used to develop this plug-in were also applied to develop models and software in chapter 4 and chapter 5. Next, chapter 4 proposed a new approach to process data from the constant rate of strain test for consolidation analysis. Then, chapter 5 is adding another new approach to use Vimoke–Taylor concept to deal with radial flows in 3D consolidation models.

Although chapter 3 and chapter 4 focus on consolidation analysis for prefabricated vertical drain (PVD) arrays, those applications are not limited to PVDs. The methodology in chapter 4 can be used for a general consolidation analysis, and ideas from chapter 5 are capable of being used for other problems that have radial flows such as modelling bore heat exchangers (Diersch, Bauer, Heidemann, R uhaak, & Sch atzl, 2011).

Chapter 3 and chapter 4 include the plug-in for FEFLOW and the software CONAXIS, which are open-source and are distributed on GitHub (<https://github.com/pham-hung>). The user manuals of these are not included in this dissertation but can be accessed via GitHub. Additionally, in chapter 4 and chapter 5, field and laboratory data were collected from two soft soil treatment projects in Mekong Delta Vietnam (section 1.6).

Because Biot's theory was used for all three publications and similar field data was used for chapter 4 and 5, it is unavoidable to have some repetitions among these chapters.

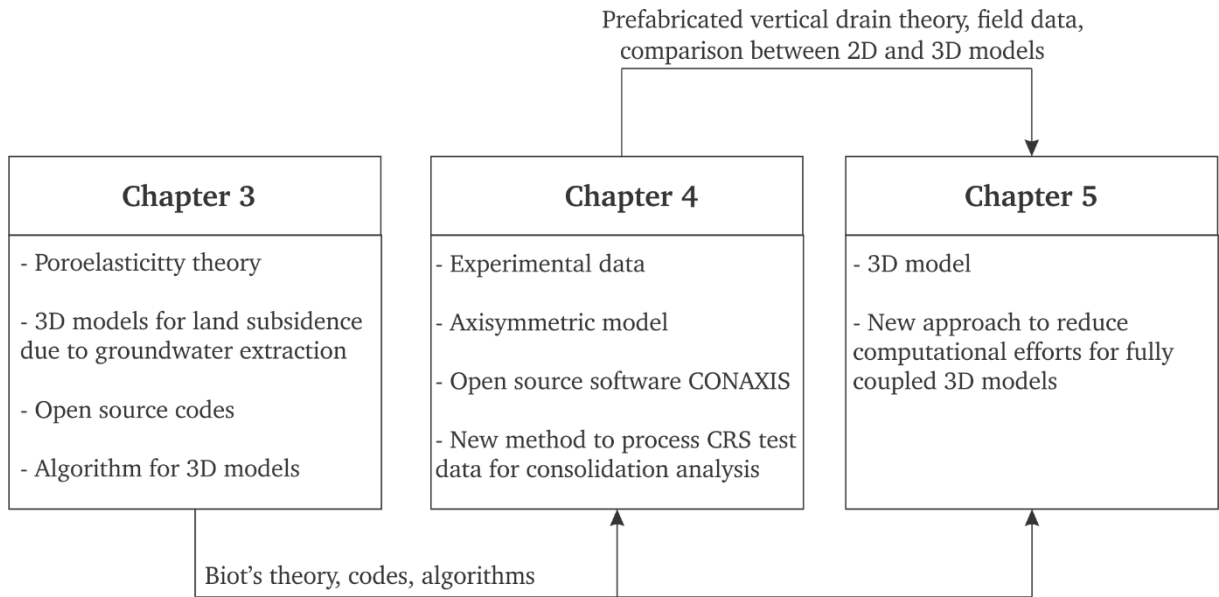


**Figure 1: Relations between research publications**

---

---

## Acknowledgement

---

*“One word is a teacher; half a word is still a teacher.”*

First, I would like to express my gratitude to both Prof. Dr. Ingo Sass and PD Dr. Wolfram Rühaak for their supervisions and supports. There would not be this dissertation without them. Even I failed many times, they are still there and believe me.

Second, I would like to acknowledge DAAD, especially ST43, for the NaWaM scholarship. Also, with their excellent administrative works, I have never encountered any difficulty within nearly four years of my scholarship.

Third, thanks to my colleague Dr. Oanh Cong Nguyen for laboratory data, field monitoring data and technical discussions that are crucial parts of this dissertation. I would also like to appreciate all colleagues who helped me a lot to integrate into a completely different culture and shared with me fun and difficulties. I have learnt many things from them.

Finally, this dissertation is dedicated to my family, especially to my wife, who sacrifices everything to journey with me and to support me.

---

---

## Table of content

---

Declaration .....	iii
Abstract .....	vii
Preface.....	viii
Acknowledgement .....	x
Table of content.....	xi
List of figures.....	xiii
Index of Abbreviations and Symbols .....	xiv
<b>1. .... Introduction .....</b>	<b>1</b>
1.1. Consolidation process .....	1
1.2. Consolidation process in land subsidence due to fluid withdrawal .....	2
1.2.1. Causes of land subsidence .....	2
1.2.2. Consolidation analysis of land subsidence .....	2
1.3. Consolidation process in soft soil treatment .....	3
1.3.1. Soft soil treatment using PVD.....	3
1.3.2. Consolidation analysis for PVD systems .....	4
1.4. Soil properties and laboratory measurements for consolidation analysis .....	5
1.5. Aims of the work .....	7
1.6. Field data .....	7
<b>2. .... Poroelasticity theory and development of finite element codes .....</b>	<b>9</b>
2.1. Poroelasticity theory .....	9
2.1.1. 3D Cartesian coordinate.....	9
2.1.2. Axisymmetric coordinate.....	10
2.1.3. Uncoupled approach – a simple form of the poroelasticity theory .....	11
2.2. Backward time integration.....	12
2.3. Galerkin approximation method .....	13
2.3.1. 3D Cartesian coordinate.....	13
2.3.2. Axisymmetric coordinate.....	14
2.4. Finite element code development .....	14
2.5. Finite element code verifications.....	15
2.5.1. 1D Terzaghi’s problem (Axisymmetric and 3D models) .....	15
2.5.2. De Leeuw’s problem (Axisymmetric and 3D models) .....	16
2.5.3. Mandel’s problem (3D model) .....	17
2.5.4. Cryer’s problem (3D model) .....	19
<b>3. .... Fully hydro-mechanical coupled Plug-in (SUB+) in FEFLOW for analysis of land subsidence due to groundwater extraction .....</b>	<b>21</b>
<b>4. .... Fully coupled analysis of consolidation by prefabricated vertical drains with applications of constant strain rate tests .....</b>	<b>27</b>

<b>5.....Application of the Vimore-Taylor concept for fully coupled models of consolidation by prefabricated vertical drains .....</b>	<b>41</b>
<b>6.....Discussion and outlook.....</b>	<b>53</b>
<b>Appendix .....</b>	<b>54</b>
Appendix A: Stiffness matrices of 3D models .....	54
Appendix B: Stiffness matrices of axisymmetric models .....	56
Appendix C: Shape functions and their derivations .....	57
C.1. Tetrahedron 4 nodes (Tet4) .....	57
C.2. Tetrahedron 10 nodes (Tet10) .....	57
C.3. Hexahedron 8 nodes (Hex8) .....	58
C.4. Hexahedron 20 nodes (Hex20) .....	59
C.5. Prism 6 nodes (Prism6) .....	64
C.6. Prism 15 nodes (Prims15) .....	64
C.7. Pyramid 5 nodes (Pyra6).....	66
C.8. Pyramid 13 nodes (Pyra13).....	67
C.9. Rectangle 4 nodes (Quad4).....	70
C.10. Rectangle 8 nodes (Quad8).....	71
C.11. Triangle 3 nodes (Tri3) .....	72
C.12. Triangle 6 nodes (Tri6) .....	72
Appendix D: Gaussian points .....	73
Tet4 and Tet10: 4 Gaussian points .....	73
Hex8: 8 Gaussian points.....	74
Hex20, Pyra5 and Pyra13: 27 Gaussian points.....	74
Prism6 and Prism15: 9 Gaussian points.....	75
Tri3 and Tri6: 3 Gaussian points .....	75
Quad4 and Quad8: 4 Gaussian points.....	75
<b>References.....</b>	<b>76</b>
<b>Curriculum Vitae .....</b>	<b>81</b>

---

---

## List of figures

---

Figure 1: Relations between research publications.....	ix
Fig. 1-1: Scheme of the incremental loading test-ILT (a) and the constant rate of strain test-CRST (b).....	6
Fig. 1-2: Processing data from ILT and CRST; (a)-results of a ILT; (b)-results of a CRST; (c)- $e \sim \log(\sigma')$ graph to determine the compression index, recompression index and pre-consolidation stress; (d)-stress-dependent parameters obtained from the CRST using ASTM D4186.....	6
Fig. 1-3: a-Locations of the Ca Mau Gas Processing Plant and Saigon-Hiep Phuoc Port Terminal projects; b-installing PVDs; c-the piston sampler.....	8
Fig. 2-1: A representative element in the Cartesian coordinate system with total stress components.....	9
Fig. 2-2: Axisymmetric coordinate system.....	11
Fig. 2-3: Terzghi's problem, 2D axisymmetric model and 3D model.....	15
Fig. 2-4: Comparison results of the pore pressure at the bottom boundary among numerical models and the analytical solution. ....	16
Fig. 2-5: De Leeuw's problem, 2D axisymmetric model and 3D models.....	17
Fig. 2-6: Comparison results of the pore pressure at the centre among numerical models and the analytical solution. ....	17
Fig. 2-7: Mandel's problem and 3D model .....	18
Fig. 2-8: Comparison of pore pressure results at $t = 10000$ s and $t = 200000$ s between the analytical solution and 3D model .....	18
Fig. 2-9: Cryer's problem and 3D model .....	19
Fig. 2-10: Pore pressure at the centre of the sphere, comparison between the 3D model and the analytical solution. ....	19

---

---

## Index of Abbreviations and Symbols

---

### *Abbreviations*

CRST	Constant rate of strain test
ILT	Incremental loading test
ASTM	American Society for Testing and Materials
PVD	Prefabricated vertical drain
FEM	Finite element method
FDM	Finite difference method
CONAXIS	Consolidation of axisymmetric models

### *Formula symbols*

$K$	$\text{kN/m}^2$	Bulk modulus
$G$	$\text{kN/m}^2$	Shear modulus
$\nu$	-	Poisson's ratio
$g$	$\text{m/s}^2$	Gravity acceleration
$m_v$	$\text{m}^2/\text{kN}$	Compressibility
$n$	-	Porosity
$e$	-	Void ratio
$u, v, w$	$\text{m}$	Displacement in x, y, z-direction, respectively
$p$	$\text{kN/m}^2$	Pore pressure, initial pore pressure
$H$	$\text{m}$	Total Head, or the model height
$z_e$	$\text{m}$	Elevation
$\gamma_f$	$\text{kN/m}^3$	Unit weight of water
$C_f, C_m, C_s$	$\text{m}^2/\text{kN}$	Compressibility of water, porous media and solid grain, respectively
$S, S_s$	$\text{m}^2/\text{kN}$	Storativity
$\delta$	-	Kronecker delta
$\alpha$	-	Biot's coefficient
$x, y, z$	-	3D Cartesian coordinate
$r, z$	-	Axisymmetric coordinate
$\sigma_{ii}$	$\text{kN/m}^2$	Stress component
$\varepsilon_{ii}$	-	Strain component
$k_{ii}$	$\text{m/s}$	Hydraulic conductivity
$t$	$\text{s}$	Time
$\theta$	-	Time integration factor
$f_i$	$\text{kN/m}^3$	Body force

### *Math notations*

$\{\}$	Vector
$[\ ]$	Matrix
$\Delta$	Incremental form
$T$	Matrix transformation
$V$	Volume domain
$R$	Area domain

---

### *Subscripts and superscripts*

$'$	Effective stress component
$ii$ ( $i=x, y, z, r$ )	Coordinate direction
$0$	Value at a time $t_0$ (initial value)
$1$	Value at a time $t$
$u$	Undrained parameter



---

## 1. Introduction

---

### 1.1. Consolidation process

Saturated porous media consist of solid grains and pore space filled with fluid which is normally groundwater. When subjected a pressure, the volume change of such porous media includes the deformation of solid skeletons, water, and pores that leads to the flow of pore fluids (Verruijt, 2016). However, the movement of fluids, which affects the deformation rate, is controlled by the permeability of the soil. This simultaneous hydro-mechanical process is governed by the consolidation theory (Verruijt, 2016).

The one-dimensional consolidation theory was first developed by (Terzaghi, 1943) for soft soils in which the compressibility of water and soil grains was ignored. Terzaghi stated that “*consolidation is any process which involves a decrease in water content of saturated soil without replacement of water by air.*” (Terzaghi, 1943) When the compression of pore fluids and soil particles are disregarded, the volume deformation of soils is equal to the volume change of pores, which is a direct result of changes in effective stress. Instantly after being loaded, all pressure is resisted by pore fluids leading to the development of the excess pore water pressure (EPWP). Then, EPWP dissipates gradually causing increases in effective stress; simultaneously, soil deformation occurs.

Biot generalised Terzaghi’s theory for three dimensional (3D) problems with the consideration of compressibility of fluids and soil particles (M. Biot, 1956; M. A. Biot, 1941). Hence, Biot’s theory can be used to describe behaviours of not only unconsolidated rocks but also other stiffer porous materials such as sandstone. Therefore, the theory has been widely applied for modelling in both the geotechnical field and in deep reservoir engineering.

Consolidation analysis in the meaning of this dissertation is to determine the deformation magnitude, the deformation rate and the EPWP dissipation rate of saturated porous media. Theoretically, the consolidation process can happen with any porous materials. In case of soils with high permeability (such as sands or gravels) and hard porous (meant is matrix porosity herein) rocks, EPWP cannot be built up, or it dissipates very quickly. Therefore, the consolidation analysis is not necessary. However, soils that have low permeability and high compressibility such, consolidation analysis is a mandatory task. Problems whose consolidation process must be taken into account can be categorised into three groups:

1. Land subsidence due to fluid withdrawal
2. Soft ground treatment
3. Self-weight consolidation of waste materials such as dredged materials, mine tailings, waste sludge, and slurry.

Both Terzaghi’s theory (Terzaghi, 1943) and the poroelasticity theory (Verruijt, 2016) assume that the strain during the consolidation process is small (i.e. infinitesimal strain theory). This assumption is valid for the first and second group, but it cannot be applied for the third group, whose materials have very high initial void ratio resulting in large deformation. Instead, a large strain consolidation theory must be used (Been & Sills, 1981; Radhika et al., 2017). Hence, the consolidation analysis of waste materials is not the object of this dissertation.

---

## **1.2. Consolidation process in land subsidence due to fluid withdrawal**

### **1.2.1. Causes of land subsidence**

Withdrawal of oil or gas, water for geothermal usage, or groundwater can cause land subsidence in the order of several meters with many serious consequences such as earth fissures, flood, land loss, or damage to infrastructure. For instance, nearly 9 m subsidence occurred in the Wilmington Oil Field area because of oil extraction (Colazas & Strehle, 1995). Subsidence created a major crisis, destroyed roads and buildings, and created localised earthquakes. Also in America, hydrocarbon withdrawal was the reason for land loss and subsidence along the Texas Gulf Coast (Sharp & Hill, 1995). In the geothermal area, extracting hot water in New Zealand triggered serious subsidence in Wairakei (up to 14 m), Tauhara (2 m), Ohaaki (3 m), and Kawerau (0.8 m) (A.Bloomer & S.Currie, 2001). Concerning overexploitation of groundwater, floods happen more frequently in Ho Chi Minh City Vietnam (Q. T. Nguyen, 2016), Bangkok Thailand (Phien-wej, Giao, & Nutalaya, 2006), and Jakarta Indonesia (Abidin et al., 2011) due to land subsidence combining with the sea level rise. If the land subsidence is not controlled, many areas of these cities will be submerged.

The mechanism of the land subsidence due to fluid withdrawal is related to the consolidation process (Poland, 1984). Extracting fluids lead to decreases in the pore pressure of confined aquifer systems or lowering the groundwater table in the unconfined aquifers. These cause increases in soil effective stress resulting in soil deformation or land subsidence. Aquifers containing gravels and sands have low compressibility and high permeability, hence they respond quickly to changes of pore pressure or effective stress. In contrast, aquitards and soft layers below land surface consisting of fine-grained particles are highly compressible and low permeable. The consolidation process occurring within these stratum takes a long time, and sometimes this phenomenon is called the land subsidence lagging (Chen et al., 2019).

Land subsidence analysis or consolidation analysis of land subsidence, which usually is performed by hydrogeologists, aims to predict the magnitude and the rate of subsidence corresponding to scenarios of fluid withdrawal or injection. From there, decisions for sustainable fluid extraction rates can be made, or methods to control land subsidence can be studied. Land subsidence can be estimated using empirical methods or theoretical approaches including analytical and numerical models based on either the conventional groundwater theory combining with 1D Terzaghi's theory or the poroelasticity theory (Galloway & Burbey, 2011). Among these techniques, numerical modelling has been applied the most (Galloway & Burbey, 2011; Rivera, Ledoux, & De Marsily, 1991; Teatini, Ferronato, Gambolati, & Gonella, 2006; Ye et al., 2016).

### **1.2.2. Consolidation analysis of land subsidence**

Under the assumption that there is no horizontal deformation, land subsidence can be estimated by using two-steps models. First, a groundwater model is set up to determine a drawdown of the phreatic surface resulting in increases in effective stress. Then, the magnitude of the land subsidence is calculated using 1D Terzaghi's consolidation theory. This approach is typically used in the field of hydrogeology because it requires less computational efforts, especially for regional models based on the finite difference method- for instance, MODFLOW with interbed storage packages (Leake & Galloway, 2007).

---

However, land subsidence is a real three-dimensional phenomenon. Generally, ignoring horizontal deformation can lead to overestimating the settlement magnitude, particularly in the vicinity region closed to pumping wells (Galloway & Burbey, 2011). For instance, the horizontal movement of the Wairakei geothermal field was up to 4.3 m that could not be neglected (A. Bloomer & S. Currie, 2001). In the review of regional land subsidence accompanying groundwater extraction, Galloway and Burbey stated that models based on the poroelasticity theory, which is not popular among hydrologists, are necessary to analyse the realistic behaviour of aquifer settings (Galloway & Burbey, 2011).

### **1.3. Consolidation process in soft soil treatment**

Foundations (soil or rock) of infrastructure facility projects need to have sufficient strength and stiffness to carry loads from other structures without causing any problem related to large deformations or instabilities. Hence, when considering a location for a project, from the geotechnical engineering view, it is preferable to choose a location whose natural soils satisfy those requirements. However, besides the geotechnical aspect, there are also many other factors concerning social and economic requirements need to be considered that result in selecting a soft soil site, which has low strength, high compressibility and low permeability soils. For instance, to be easily accessed, a container terminal must be located in a coastal area that lays on a soft clay deposit (Cai Mep International Terminal, Vietnam) (C.-O. Nguyen, Tran, & Dao, 2019). Alternatively, because of the shortage of available land, facilities such as airports and seaports have to be placed on reclaimed land from the sea whose soils are not strong enough to support associated structures (Kansai International airport in Japan, Changi International airport in Singapore) (J. Chai & Carter, 2011). In those cases, a ground improvement method before construction activities is inevitable.

Soft soil improvement techniques aim to prevent large and/or differential settlements and subsequently potential damages to structures. They can be categorised into two main groups (Bergado, 1996). The first group involves works on the soil only such as dewatering (sand drains, PVD, horizontal drains) and compaction (preloading using earth fills, water in tanks, vacuum loading, groundwater lowering). The purpose of these methods is to speed up the consolidation process and to take up soil deformations induced by structures before they are built. The second group requires adding extra materials into soils and utilisation of reinforcements; for instance, deep mixing method using lime and cement, chemical piles, sand compaction piles, stone columns or granular piles. Following these techniques, soils are strengthened to have enough stiffness and strength to withstand structure loads.

#### **1.3.1. Soft soil treatment using PVD**

Among soft soil improvement methods, PVDs combined with surcharge loading and vacuum water extraction have been widely used because of many advantages (Bergado, 1996; Bo, Arulrajah, Horpibulsuk, & Leong, 2015; J. Chai, Horpibulsuk, Shen, & Carter, 2014; Hiep & Chung, 2018; Indraratna, Sathanathan, Rujikiatkamjorn, & Balasubramaniam, 2005; Kumarage & Gnanendran, 2019; Liu & Rowe, 2015; B.-P. Nguyen & Kim, 2019; Rixner, Kramer, & Smith, 1986; C. Rujikiatkamjorn & Indraratna, 2006; Tajuddin et al., 2014; Zhou, Lok, Zhao, Mei, & Li, 2017). PVDs are band-shaped and have channelled plastic cores wrapped with geotextile membranes. When PVDs are installed into a formation, water can pass into the filter and discharges along the channel. PVDs are installed into soils vertically and are arranged in a triangular or a rectangular pattern. On the surface, a permeable sand

---

layer is added, which acts like a drained layer. When vacuum extraction is not used, an earth-fill layer that induces preloading stress is built above the sand layer. In case PVDs are combined with the vacuum pumping, horizontal pipes are connecting from the PVD grid and the sand layer with the pump. An impervious plastic liner (geotextile, mostly made of high-density polyethylene) covers all the treated area; hence, the vacuum pressure can be applied. Additionally, to sustain a hydraulical decoupling of the treated area, a vertical clay wall is usually closing the array to all directions. Theoretically, with the vacuum pump, the maximum suction can be reached close to the air pressure (-98.1kPa). However, in reality, the maximum vacuum pressure is only around -80 kPa. Therefore, if the vacuum pressure is not enough (i.e. required preloading value is greater than the vacuum pressure), another earth fill layer is added on the top of the geotextile.

PVDs combined with surcharge load and vacuum extraction has many advantages (J. Chai & Carter, 2011). First, because of radial soil water flow into the PVDs instead of vertical flow to the surface, the drainage treatment time is shortened; therefore, the consolidation process is thus accelerated which results in enhanced construction time. Second, the method is simple and can be applied to a large area without requiring heavy machinery. A number of drill rigs may be operated simultaneously to save time. Third, dimensions of PVDs are small; hence, drilling PVDs reduces the soil disturbance. Finally, the method is environmentally friendly because no cement and lime e.g. or chemical agents are added into the soil.

### 1.3.2. Consolidation analysis for PVD systems

Consolidation analysis for PVD systems is required to answer fundamental questions for the construction design.

1. What is the maximum settlement?
2. How to characterize the soil deformation over time and what are potential risks?
3. How long does it take until structural construction can be built?
4. What are the dimensioning parameters of the PVD array?
5. What the dimensioning parameters of the earth fill layer?

The performance of a PVD system is analysed by using either an analytical model (S Hansbo, 1981; Indraratna et al., 2005; B.-P. Nguyen & Kim, 2019; Zhou et al., 2017) or a numerical model (Hiep & Chung, 2018; Liu & Rowe, 2015; Pham, Rühaak, Schulte, & Sass, 2019; C. Rujikiatkamjorn & Indraratna, 2006; Cholat Cholat Rujikiatkamjorn, Indraratna, & Chu, 2008; Tajuddin et al., 2014). Each PVD has a specific influence zone that is idealised as a cylinder called unit cell. The radius of the unit cell is determined based on the installed pattern of PVDs and the distance between PVDs. When installing PVDs into soils using a machine with a mandrel, the mandrel can disturb soils and create zones called smear zones. Dimensions of PVDs and smear zones are also converted into equivalent circular zones. When the discharge capacity of the PVD is infinitive, the well resistance is ignored and vice versa.

Because the unit cell is cylindrical, analytical solutions of the unit cell were developed based on the axisymmetric model. Barron first introduced analytical solutions for different cases: free strain with or without the smear zone and the well resistance, equal strain with or without the smear zone and the well resistance (Barron, 1948). Barron's solutions contain

---

Bessel functions that are laborious to compute; hence, Hansbo developed simpler solutions for equal strain cases that have been widely applied (Sven Hansbo, 1976). Afterwards, based on Barron and Hansbo's solutions, other analytical solutions for specific cases have been introduced. For instance, Indraratna developed the solution for PVDs with vacuum preloading (Indraratna et al., 2005) or Zhou et al. presented the solution for multi-layer soil cases (Zhou et al., 2017).

Numerical models of PVD systems can be divided into three main groups: axisymmetric models of the unit cell, 2D plane strain models, and 3D models (J. Chai & Carter, 2011; Walker, 2011). While both the finite element method (FEM) and the finite difference method (FDM) are used for axisymmetric models, FE models based on Biot's theory (i.e. poroelasticity theory) are commonly used for 2D and 3D analyses. Axisymmetric models are the most common and are applied for complicated cases that cannot be solved with analytical solutions. For example, different scenarios of surcharge loads, varied length of PVDs (C.-O. Nguyen et al., 2019), nonlinear soil properties and multi-layers of soils (Zhou et al., 2017).

When PVDs are installed under long embankments and horizontal deformations are essential, 2D plane strain models are frequently utilised (Walker, 2011). According to Chai (J. Chai & Carter, 2011), methods for modelling PVD systems using 2D plane strain models can be divided into four groups. The first group models PVDs with solid elements and matches the consolidation degree of unit cell and plane strain models (Indraratna & Redana, 1997). The second group uses macro elements in FEM. The third group simulates PVDs using 1D elements (Hird, Pyrah, & Russel, 1992). Finally, the fourth group modifies the vertical hydraulic conductivity to combine drainage effects of both PVDs and soils (J.-C. Chai, Shen, Miura, & Bergado, 2001). Along with axisymmetric models, 2D plane strain models are used extensively for practical purposes.

In many cases, because of the essential effects of three-dimensional deformations, 3D models are needed. For instance, when PVDs are used for circular or square embankments or when surcharge loads are not uniform. However, 3D models of PVD systems have been published barely or incompletely. Particular exceptions include Rujikiatkamjorn (C. Rujikiatkamjorn & Indraratna, 2006; Cholachat Rujikiatkamjorn et al., 2008), where a large cylindrical unit cell (450 mm diameter and 850 mm height) and a PVD system (a 14 x 25 x 20 m treated zone with 350 PVDs) were modelled in ABAQUS using solid elements. Limitations of full 3D models for PVD systems arise from three reasons: a large number of PVDs, small sizes of PVDs and smear zones and radial flows into PVDs. These problems lead to significant increases in the number of nodes, the number of elements and the total degrees of freedom in FEM models, especially for fully-coupled 3D models, which results in excessive computational efforts.

#### **1.4. Soil properties and laboratory measurements for consolidation analysis**

Key input parameters consolidation analyses are the soil permeability, the soil compressibility and the soil strength. These parameters are usually obtained from consolidation tests (the oedometer test or the incremental loading test-ILT (ASTM-D2435, 2011), the constant rate of strain test – CRST (ASTM/D4186M-12e1, 2014), Rowe cell test (Sheahan & Watters, 1996)), the permeability test and shear tests (the direct shear test (ASTM-D3080, 2011), the triaxial shear test (ASTM/D7181-11, 2011)). Among these tests, the ILT and the CRST are the most popular and important.

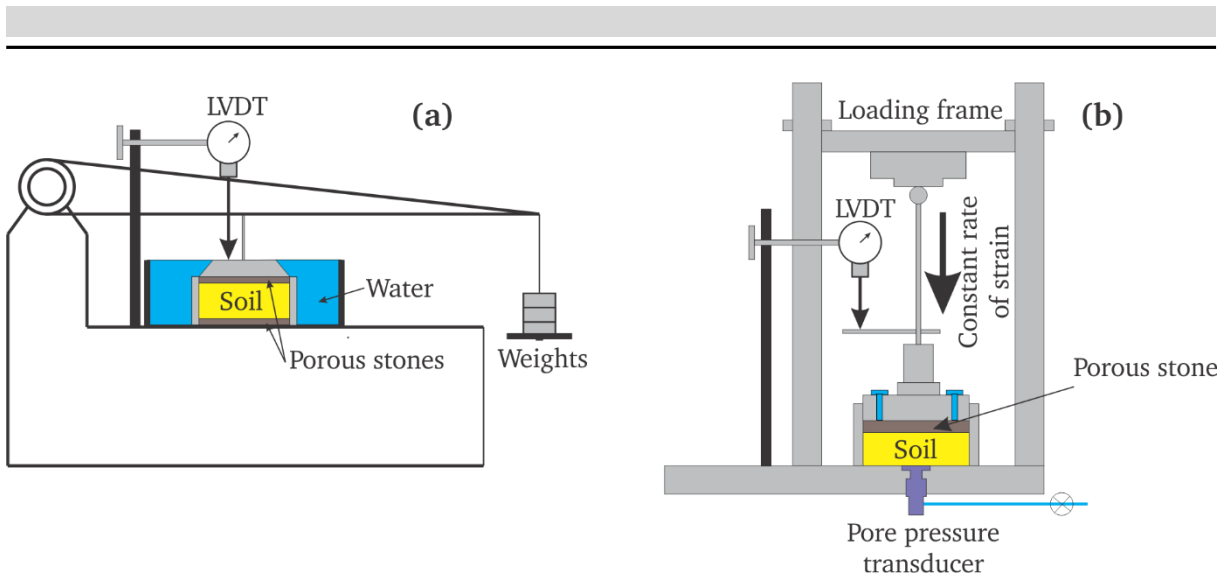


Fig. 1-1: Scheme of the incremental loading test-ILT (a) and the constant rate of strain test-CRST (b)

In the ILT (Fig. 1-1 a), the soil sample is laterally constrained by O-rings and is axially sandwiched between two porous stones on the top and the bottom. Weights are placed on the frame to cause stress on the top of the soil sample. Soil vertical deformations are measured by a dial gauge or a linear variable differential transformer. Usually, each load level is kept constant during 24 hours before the next weight that is double the previous weight is added. Hence, it often takes a week to conduct a test. Meanwhile, in the CRST (Fig. 1-1b), the porous stone on the bottom is replaced by an impermeable rigid plate with a pore pressure transducer that records the excess pore pressure (EPWP) taken place during the test. Furthermore, the loading frame is connected to the motor so that the strain rate is controlled by the computer and is kept constant. In comparison to the ILT, test data of the CRST is continuous and is recorded automatically (Fig. 1-2 a-b). Moreover, the CRST only take one to two days for a test.

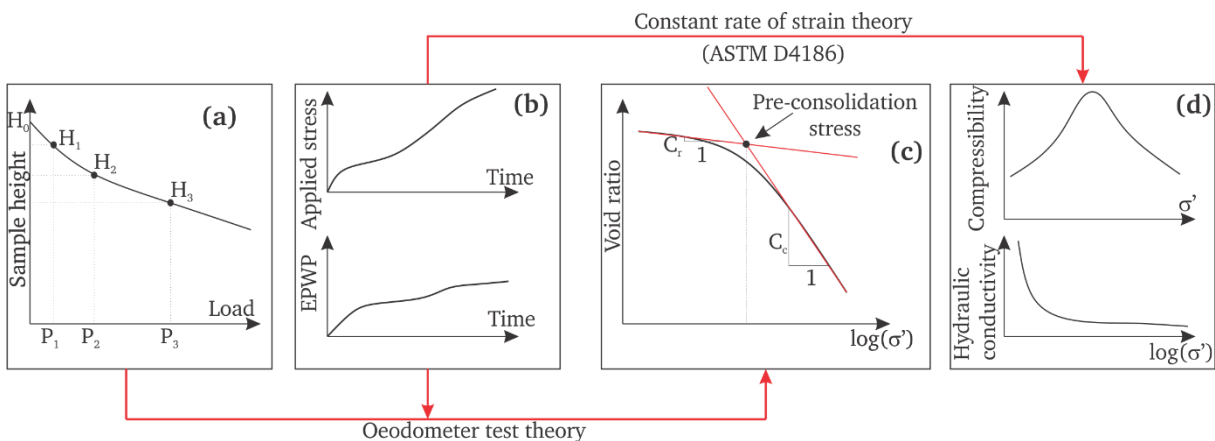


Fig. 1-2: Processing data from ILT and CRST; (a)-results of a ILT; (b)-results of a CRST; (c)- $e \sim \log(\sigma')$  graph to determine the compression index, recompression index and pre-consolidation stress; (d)-stress-dependent parameters obtained from the CRST using ASTM D4186.

As shown in Fig. 1-2, despite the differences between recorded data of the CRST and the ILT, the same oedometer test theory is commonly used for both tests to obtain parameters for FE models (compression index  $C_c$  and recompression index  $C_r$ ) by plotting test data as  $\log(\sigma') \sim e$

---

graph (Fig. 1-2 c), where  $\sigma'$  is the vertical effective stress and  $e$  is void ratio. While the vertical effective stress for the ILT can be computed directly from weights, ASTM-D4186 is used to calculate  $\sigma'$  from the CRST data (ASTM/D4186M-12e1, 2014) based on the theory developed by Wissa (Wissa, 1971). Additionally, dependences of the compressibility and the hydraulic conductivity on the effective stress can also be obtained from CRST data with Wissa's theory (Fig. 1-2 d). These stress-dependent curves can directly be used as input parameters for FE models. However, this approach has not applied yet.

### **1.5. Aims of the work**

The reported research proposes new approaches for consolidation analysis using fully hydro-mechanical coupled FE models based on Biot's theory. The first part of this dissertation (chapter 3) introduces a FEFLOW plug-in called SUB+ for 3D land subsidence analysis. FEFLOW is a well-known finite element software for groundwater, heat transfer, and transport modelling. However, FEFLOW is not capable of modelling land subsidence. The algorithm and codes used to develop the plug-in are used for later works. Then, in chapter 4, a new method to process laboratory data of CRST is proposed. An open-source software called CONAXIS is developed for this purpose. Finally, chapter 5 applies the Vimoke-Taylor concept, which has been widely used in groundwater modelling, to reduce computational efforts of 3D consolidation models that contain radial flows.

Two approaches in chapter 4 and chapter 5 are applied for consolidation analysis of PVD systems because the laboratory data and field monitoring data for this type of problem are available. However, applications of these approaches are not restricted to PVD systems. The laboratory data processing method in chapter 4 can be used for a general consolidation analysis. Ideas in chapter 5 can be applied to other cases that also have radial flows such as consolidation by sand columns or rock columns, flows into bore heat exchangers or geothermal wells.

### **1.6. Field data**

The field data including laboratory data and field monitoring data in chapter 4 and chapter 5 were from two soft soil improvement projects located in Mekong Delta Vietnam. The first project is Ca Mau Gas Processing Plant (CMGPP), and the second project is Saigon-Hiep Phuoc Port Terminal (SHPT) (Fig. 1-3a). In the CMGPP project, the treated area is approximately 330 m x 113 m that has 17.5 m thickness of soft soils. Compared to the CMGPP project, the SHPT project has a larger improvement area (505 m x 222 m) with a double thickness of soft soils (35.0 m). In both projects, PVDs combining with the surcharge loading and the vacuum pumping methods were used to reduce post-construction settlement and construction time (Fig. 1-3b). The high-quality soil samples for the CRST were retrieved by the piston sampler with thin wall tube (Fig. 1-3c).

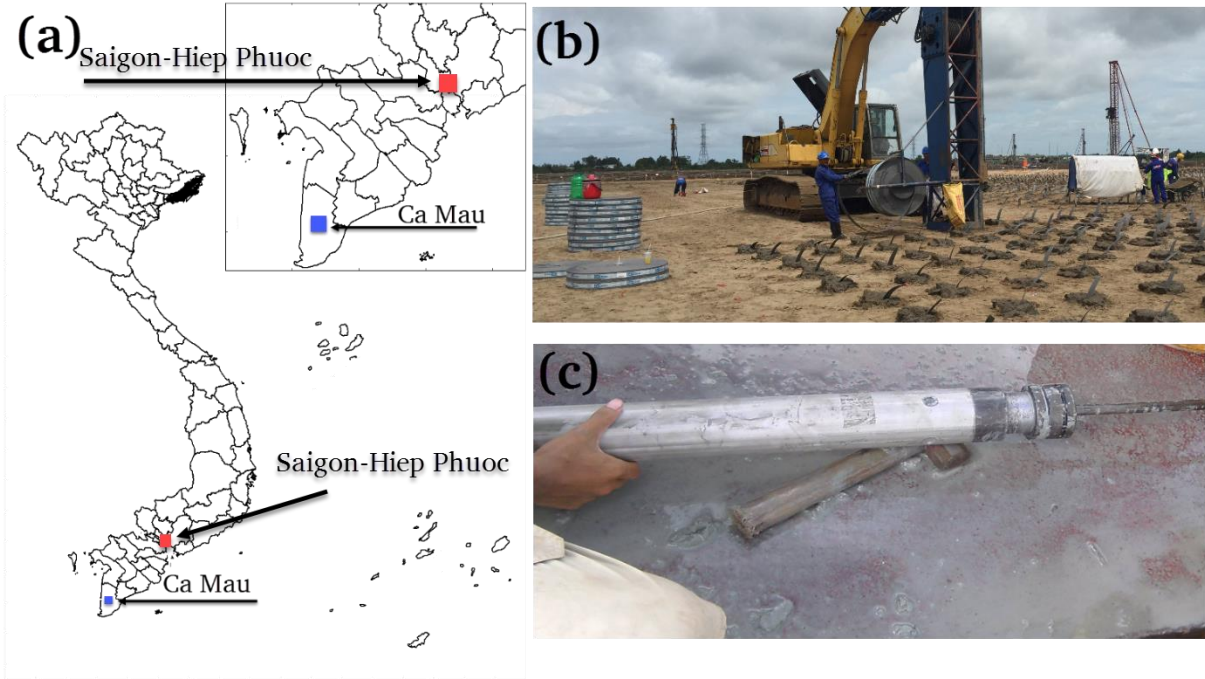


**Fig. 1-3: a-Locations of the Ca Mau Gas Processing Plant and Saigon-Hiep Phuoc Port Terminal projects; b-installing PVDs; c-the piston sampler.**

## 2. Poroelasticity theory and development of finite element codes

### 2.1. Poroelasticity theory

#### 2.1.1. 3D Cartesian coordinate

Fig. 2-1 shows a representative element in Cartesian 3D coordinate system. The displacements in  $x$ ,  $y$ ,  $z$ -direction are denoted as  $u$ ,  $v$  and  $w$ , respectively. The pore water pressure is denoted as  $p$  and the total head is  $H$ . The total head is related to the pore pressure by:

$$H = p\gamma_w + z_e \quad (2.1)$$

where  $\gamma_w$  is the unit weight of water and  $z_e$  is the elevation.

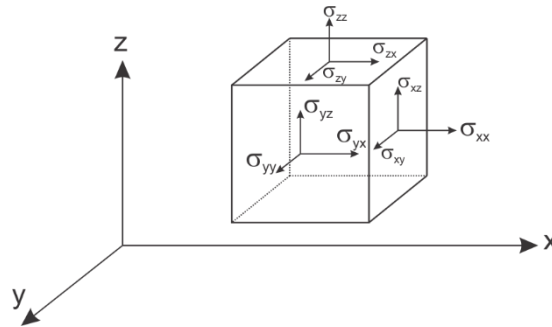


Fig. 2-1: A representative element in the Cartesian coordinate system with total stress components

The poroelasticity theory includes the storage equation and the stress equilibrium equations. The storage equation is defined as (E. Detournay & A. H.-D. Cheng, 1993; Wolfram Rühaak, Bense, & Sass, 2014; W. Rühaak, Pei, Heldmann, & Sass, 2017; Verruijt, 2016):

$$\alpha \frac{\partial \varepsilon}{\partial t} + S \frac{\partial p}{\partial t} - \frac{\partial}{\partial x} \left( \frac{k_x}{\gamma_f} \frac{\partial p}{\partial x} \right) - \frac{\partial}{\partial y} \left( \frac{k_y}{\gamma_f} \frac{\partial p}{\partial y} \right) - \frac{\partial}{\partial z} \left( \frac{k_z}{\gamma_f} \frac{\partial p}{\partial z} \right) = 0 \quad (2.2)$$

where  $\varepsilon = \varepsilon_{xx} + \varepsilon_{yy} + \varepsilon_{zz}$  is the total volume strain;  $\alpha$  is the Biot's coefficient;  $t$  is the time;  $S$  is the storativity;  $k_i$  is the hydraulic conductivity in  $x$ ,  $y$ ,  $z$ -direction;  $\varepsilon_{ii}$  ( $i = x, y, z$ ) is the axial strain components; and  $\gamma_f$  is the unit weight of water. The storativity is defined as (Verruijt, 2016):

$$S = nC_f + (\alpha - n)C_s \quad (2.3)$$

where  $n$  is the porosity;  $C_f$  is the compressibility of water;  $C_s$  is the compressibility of solid grains (or the soil skeletons).

The stress equilibrium equations are (Cheng, 2016; E. Detournay & A. H.-D. Cheng, 1993; Verruijt, 2016):

$$\begin{aligned}
\frac{\partial \sigma'_{xx}}{\partial x} + \frac{\partial \sigma'_{yx}}{\partial y} + \frac{\partial \sigma'_{xz}}{\partial z} + \alpha \frac{\partial p}{\partial x} - f_x &= 0 \\
\frac{\partial \sigma'_{xy}}{\partial x} + \frac{\partial \sigma'_{yy}}{\partial y} + \frac{\partial \sigma'_{yz}}{\partial z} + \alpha \frac{\partial p}{\partial y} - f_y &= 0 \\
\frac{\partial \sigma'_{xz}}{\partial x} + \frac{\partial \sigma'_{yz}}{\partial y} + \frac{\partial \sigma'_{zz}}{\partial z} + \alpha \frac{\partial p}{\partial z} - f_z &= 0
\end{aligned} \tag{2.4}$$

where  $\sigma_{ij}$  and  $\sigma'_{ij}$  are the total stress and the effective stress components respectively and  $f_i$  is the body forces. The total stress is the sum of the effective stress and the pore pressure:

$$\sigma_{ij} = \sigma'_{ij} + \alpha \delta p = \sigma'_{ij} + \alpha \delta (H - z_e) \gamma_w \tag{2.5}$$

where  $\delta$  is the Kronecker delta.

The relation between the effective stress and the strain follows Hook's law (Cheng, 2016; Verruijt, 2016):

$$\begin{aligned}
\sigma'_{xx} &= -\left(K + \frac{4}{3}G\right) \frac{\partial u}{\partial x} - \left(K - \frac{2}{3}G\right) \frac{\partial v}{\partial y} - \left(K - \frac{2}{3}G\right) \frac{\partial w}{\partial z} \\
\sigma'_{yy} &= -\left(K + \frac{4}{3}G\right) \frac{\partial v}{\partial y} - \left(K - \frac{2}{3}G\right) \frac{\partial u}{\partial x} - \left(K - \frac{2}{3}G\right) \frac{\partial w}{\partial z} \\
\sigma'_{zz} &= -\left(K + \frac{4}{3}G\right) \frac{\partial w}{\partial z} - \left(K - \frac{2}{3}G\right) \frac{\partial u}{\partial x} - \left(K - \frac{2}{3}G\right) \frac{\partial v}{\partial y} \\
\sigma'_{xy} = \sigma'_{yx} &= -G \left( \frac{\partial u}{\partial y} + \frac{\partial v}{\partial x} \right); \sigma'_{xz} = \sigma'_{zx} = -G \left( \frac{\partial u}{\partial z} + \frac{\partial w}{\partial x} \right); \sigma'_{yz} = \sigma'_{zy} = -G \left( \frac{\partial w}{\partial y} + \frac{\partial v}{\partial z} \right) \\
\varepsilon_{xx} &= \frac{\partial u}{\partial x}; \varepsilon_{yy} = \frac{\partial v}{\partial y}; \varepsilon_{zz} = \frac{\partial w}{\partial z}
\end{aligned} \tag{2.6}$$

where  $K = 1/C_m$  is the bulk modulus;  $C_m$  is the compressibility of porous media;  $G$  is the shear modulus.

Equation 2.2 and equation 2.4 are the full-coupled equations that contain four variables: a displacement each in  $x$ ,  $y$ ,  $z$ -direction and the pore pressure  $p$ . Equation 2.2 implies that the change of the total volume, which has two components  $\alpha(\partial\varepsilon/\partial\tau)$  and  $S(\partial p/\partial t)$ , is equal to the amount of water that exits the element  $\nabla(k \nabla p)$ . The former component is caused by changes in effective stress, and the latter component is derived from changes in the pore pressure.

### 2.1.2. Axisymmetric coordinate

For the axisymmetric models, the coordinate system is shown in Fig. 2-2. The horizontal and vertical displacement and the excess pore pressure are denoted as  $u$ ,  $v$  and  $p$ , respectively.

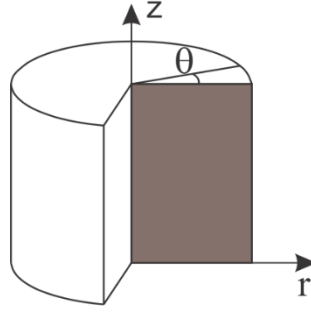


Fig. 2-2: Axisymmetric coordinate system

Equation 2.2 is rewritten for the axisymmetric coordinate system (Verruijt, 2016).

$$\alpha \frac{\partial \varepsilon}{\partial t} + S \frac{\partial p}{\partial t} = \frac{\partial}{\partial r} \frac{k_r}{\gamma_f} \frac{\partial p}{\partial r} + \frac{1}{r} \frac{k_r}{\gamma_f} \frac{\partial p}{\partial r} + \frac{\partial}{\partial z} \frac{k_z}{\gamma_f} \frac{\partial p}{\partial z} \quad (2.7)$$

Similarly, equation 2.4 and equation 2.6 are rewritten as (Verruijt, 2016):

$$\begin{aligned} \frac{\partial \sigma_{rr}}{\partial r} + \frac{\sigma_{rr} - \sigma_{\theta\theta}}{r} + \frac{\partial \sigma_{rz}}{\partial z} - f_r &= 0 \\ \frac{\partial \sigma_{rz}}{\partial r} + \frac{\partial \sigma_{rz}}{r} + \frac{\partial \sigma_{zz}}{\partial z} - f_z &= 0 \end{aligned} \quad (2.8)$$

where  $\sigma_{rr}$ ,  $\sigma_{\theta\theta}$ ,  $\sigma_{rz}$ ,  $\sigma_{zz}$  are the total stress components,  $f_r$  and  $f_z$  are the body force components

$$\begin{aligned} \sigma_{rr} &= \sigma'_{rr} + \alpha p = -(K - 2G/3)\varepsilon - 2G(\partial u / \partial r) + \alpha p \\ \sigma_{zz} &= \sigma'_{zz} + \alpha p = -(K - 2G/3)\varepsilon - 2G(\partial v / \partial z) + \alpha p \\ \sigma_{\theta\theta} &= \sigma'_{\theta\theta} + \alpha p = -(K - 2G/3)\varepsilon - 2G(u/r) \\ \sigma_{rz} &= \sigma'_{rz} = -2G(\partial u / \partial z + \partial v / \partial r) \\ \varepsilon &= \varepsilon_{rr} + \varepsilon_{\theta\theta} + \varepsilon_{zz} = (\partial u / \partial r) + (u/r) + (\partial v / \partial z) \end{aligned} \quad (2.9)$$

where  $\varepsilon_{rr}$ ,  $\varepsilon_{zz}$ , and  $\varepsilon_{\theta\theta}$  are the strain components;  $\sigma'_{rr}$ ,  $\sigma'_{zz}$ , and  $\sigma'_{\theta\theta}$  are the effective stress.

### 2.1.3. Uncoupled approach – a simple form of the poroelasticity theory

Assuming that there is no horizontal deformation, if the gravity direction is the negative  $z$ -direction, we have:

$$\varepsilon_{xx} = \varepsilon_{yy} = 0 \quad (2.10)$$

If porous media behaves as an elastic material, then:

$$\varepsilon = \varepsilon_{zz} = -m_v \sigma'_{zz} = -m_v (\sigma_{zz} - \alpha p) = -m_v [\sigma_{zz} - \alpha \gamma_w (H - z_e)] \quad (2.11)$$

where  $m_v = 1/(K+4G/3)$  is the confined compressibility of porous media. From equation 2.11, we have:

$$\alpha \frac{\partial \varepsilon}{\partial t} = -\alpha m_v \frac{\partial \sigma_{zz}}{\partial t} + \alpha^2 m_v \frac{\partial p}{\partial t} \quad (2.12)$$

Substituting equation 2.12 into equation 2.2 gives:

$$(\alpha^2 m_v + S) \frac{\partial p}{\partial t} = \nabla \left( \frac{k}{\gamma_f} \nabla p \right) + m_v \frac{\partial \sigma_{zz}}{\partial t} \quad (2.13)$$

If the total stress is assumed to be constant over time, the second term of the right-hand side is zero, and equation 2.13 becomes:

$$S_s \frac{\partial p}{\partial t} = \nabla \left( \frac{k}{\gamma_f} \nabla p \right) \quad (2.14)$$

Equation 2.14 is the form of the Jacob equation for confined unsteady groundwater flow (Jacob, 1940). The modified new storativity parameter  $S_s$  includes the compressibility of water, solid grains and porous media. Equation 2.14 has only the pore pressure or total head as the variable or it is an uncoupled form of the coupled equation system of Biot's theory.

## 2.2. Backward time integration

The storage equations (equation 2.2 or equation 2.7) contain the time variable. To solve these equations, they are integrated over a time step  $\Delta t$ . We denote  $t_0$  as the beginning of the time step, and  $t_1 = t_0 + \Delta t$  is the end of the time step.

For 3D models:

$$\alpha [\varepsilon(t_1) - \varepsilon(t_0)] + S [p(t_1) - p(t_0)] - \Delta t \left[ \frac{\partial}{\partial x} \left( \frac{k_x}{\gamma_f} \frac{\partial \bar{p}}{\partial x} \right) + \frac{\partial}{\partial y} \left( \frac{k_y}{\gamma_f} \frac{\partial \bar{p}}{\partial y} \right) - \frac{\partial}{\partial z} \left( \frac{k_z}{\gamma_f} \frac{\partial \bar{p}}{\partial z} \right) \right] = 0 \quad (2.15)$$

where  $\bar{p}$  is the average pressure during the time step  $\Delta t$ .

$$\bar{p} = (1 - \theta) p(t_0) + \theta p(t_1) \quad (2.16)$$

where  $\theta$  is the interpolation parameter.  $\theta=1$  indicates a backward finite difference approximation in time,  $\theta=0$  is the forward approximation scheme (Euler scheme) and  $\theta=0.5$  is the Crank-Nicolson scheme (Butcher, 2016). The backward integration scheme is used in this dissertation. Hence, equation 2.15 with the backward integration scheme becomes:

$$\alpha \Delta \varepsilon + S \Delta p - \Delta t \left[ \frac{\partial}{\partial x} \left( \frac{k_x}{\gamma_f} \frac{\partial p}{\partial x} \right) + \frac{\partial}{\partial y} \left( \frac{k_y}{\gamma_f} \frac{\partial p}{\partial y} \right) - \frac{\partial}{\partial z} \left( \frac{k_z}{\gamma_f} \frac{\partial p}{\partial z} \right) \right] = 0 \quad (2.17)$$

where  $\Delta$  indicates the incremental form of the total strain and the pore pressure, and  $p$  implies  $P_1$ .

Similarly, for axisymmetric models, the incremental form with the backward integration scheme of equation 2.7 is:

$$\alpha\Delta\varepsilon + S\Delta p - \left( \frac{k_r}{\gamma_f} \frac{\partial p}{\partial r} + \frac{1}{r} \frac{k_r}{\gamma_f} \frac{\partial p}{\partial r} + \frac{\partial}{\partial z} \frac{k_z}{\gamma_f} \frac{\partial p}{\partial z} \right) = 0 \quad (2.18)$$

### 2.3. Galerkin approximation method

Within a time step  $\Delta t$ , we denote  $\Delta d$  and  $\Delta p$  as the incremental vectors of the displacement field and the pore pressure field, respectively. For 3D models  $\Delta d = \{\Delta u \ \Delta v \ \Delta w\}^T$  and for axisymmetric models  $\Delta d = \{\Delta u \ \Delta v\}^T$ .

With the FE method, a calculation domain is divided into a number of elements  $noe$ . Incremental vectors of the displacement and the pore pressure field of each element are  $\Delta d_e$  and  $\Delta p_e$ , respectively.

The incremental displacement and the pore pressure of a point inside an element are approximated by Galerkin method:

$$\Delta u = N_d u_e; \Delta v = N_d v_e; \Delta w = N_d w_e; \Delta p = N_p p_e \quad (2.19)$$

where  $N_d$  and  $N_p$  are the shape functions of the displacement field and the pore pressure field. For each element type, detailed of shape functions are presented in Appendix C.

#### 2.3.1. 3D Cartesian coordinate

The storage equation 2.17 is written under the weak form as:

$$\sum_1^{noe} \iiint_V N_p^T \left\{ \alpha\Delta\varepsilon + S\Delta p - \Delta t \left[ \frac{\partial}{\partial x} \left( \frac{k_x}{\gamma_f} \frac{\partial p}{\partial x} \right) + \frac{\partial}{\partial y} \left( \frac{k_y}{\gamma_f} \frac{\partial p}{\partial y} \right) - \frac{\partial}{\partial z} \left( \frac{k_z}{\gamma_f} \frac{\partial p}{\partial z} \right) \right] \right\} dV = 0 \quad (2.20)$$

The incremental strain:

$$\Delta\varepsilon = \Delta\varepsilon_{xx} + \Delta\varepsilon_{yy} + \Delta\varepsilon_{zz} = \frac{\partial N_d}{\partial x} \Delta u_e + \frac{\partial N_d}{\partial x} \Delta v_e + \frac{\partial N_d}{\partial x} \Delta w_e \quad (2.21)$$

Substituting equation 2.21 into equation 2.20 gives:

$$\begin{aligned} & \sum_1^{noe} \iiint_V \left\{ N_p^T \frac{\partial N_d}{\partial x} \Delta u_e + N_p^T \frac{\partial N_d}{\partial y} \Delta v_e + N_p^T \frac{\partial N_d}{\partial z} \Delta w_e dV + S N_p^T N_p \Delta p_e \right\} dV \\ & - \sum_1^{noe} \iiint_V N_p^T \Delta t \left\{ \frac{\partial}{\partial x} \left( \frac{k_x}{\gamma_f} \frac{N_p}{\partial x} p_e \right) + \frac{\partial}{\partial y} \left( \frac{k_y}{\gamma_f} \frac{N_p}{\partial x} p_e \right) + \frac{\partial}{\partial z} \left( \frac{k_z}{\gamma_f} \frac{N_p}{\partial x} p_e \right) \right\} dV = 0 \end{aligned} \quad (2.22)$$

The incremental approximation form of the stress equilibrium equations is:

$$\begin{aligned}
\sum_1^{noe} \iiint_V N_d^T \left( \frac{\partial \Delta \sigma_{xx}}{\partial x} + \frac{\partial \Delta \sigma_{yx}}{\partial y} + \frac{\partial \Delta \sigma_{xz}}{\partial z} - \Delta f_x \right) dV &= 0 \\
\sum_1^{noe} \iiint_V N_d^T \left( \frac{\partial \Delta \sigma_{xy}}{\partial x} + \frac{\partial \Delta \sigma_{yy}}{\partial y} + \frac{\partial \Delta \sigma_{yz}}{\partial z} - \Delta f_y \right) dV &= 0 \\
\sum_1^{noe} \iiint_V N_d^T \left( \frac{\partial \Delta \sigma_{xz}}{\partial x} + \frac{\partial \Delta \sigma_{yz}}{\partial y} + \frac{\partial \Delta \sigma_{zz}}{\partial z} - \Delta f_z \right) dV &= 0
\end{aligned} \tag{2.23}$$

From equation 2.22 and equation 2.23, the coupled equation set is written under the matrix form is:

$$\begin{bmatrix} [K] & [L] \\ -[L]^T & [M] + \Delta t \times [P] \end{bmatrix} \begin{Bmatrix} \Delta d \\ \Delta p \end{Bmatrix} = \begin{Bmatrix} \Delta F \\ -\Delta t \times [P] \times p_0 + \Delta t \times Q \end{Bmatrix} \tag{2.24}$$

where  $[K]$  is the matrix for the displacement field,  $[M]$  and  $[P]$  are the matrices for the transient field,  $[L]$  is the coupled matrix,  $p_0$  is the water head of the previous calculation step,  $\Delta F$  is the incremental load vector, and  $Q$  is the extract rate vector. The detailed explanations are given in Appendix A.

### 2.3.2. Axisymmetric coordinate

Similarly, the total incremental strain component for axisymmetric models is:

$$\Delta \varepsilon = \frac{\partial N_d}{\partial r} \Delta u_e + \frac{N_d}{r} \Delta u_e + \frac{\partial N_d}{z} \Delta v_e \tag{2.25}$$

Equation 2.18 is written under the weak form as:

$$\begin{aligned}
\sum_1^{noe} \iint_R N_p^T \alpha \left\{ \frac{\partial N_d}{\partial r} \Delta u_e + \frac{N_d}{r} \Delta u_e + \frac{\partial N_d}{z} \Delta v_e \right\} r dR + \sum_1^{noe} \iint_R N_p^T S(N_p \Delta p_e) r dR \\
- \sum_1^{noe} \iint_R N_p^T \Delta t \left\{ \frac{\partial}{\partial r} \frac{k_r}{\gamma_f} \left( \frac{\partial}{\partial r} (N_p \Delta p_e) \right) + \frac{1}{r} \frac{k_r}{\gamma_f} \left( \frac{\partial}{\partial r} (N_p \Delta p_e) \right) + \frac{\partial}{\partial z} \frac{k_z}{\gamma_f} \left( \frac{\partial}{\partial z} (N_p \Delta p_e) \right) \right\} r dR = 0
\end{aligned} \tag{2.26}$$

The incremental approximation form of the stress equilibrium equations is:

$$\begin{aligned}
\sum_1^{noe} \iint_R N_d^T \left[ \frac{1}{r} \frac{\partial}{\partial r} (r \Delta \sigma_{rr}) + \frac{\partial}{\partial z} \Delta \sigma_{rz} - \frac{\Delta \sigma_{tt}}{r} - \Delta f_r \right] r dR = 0 \\
\sum_1^{noe} \iint_R N_d^T \left[ \frac{1}{r} \frac{\partial}{\partial r} (r \Delta \sigma_{zr}) + \frac{\partial}{\partial z} H \sigma_{zz} - \Delta f_z \right] r dR = 0
\end{aligned} \tag{2.27}$$

From equation 2.26 and equation 2.27, a similar equation as equation 2.24 can be obtained. Detailed explanations are presented in Appendix B.

## 2.4. Finite element code development

The finite element codes in chapter 3, 4 and 5 are open-source and are distributed via GitHub ([www.github.com/pham-hung](http://www.github.com/pham-hung)). Codes are developed using C++ programming language with Qt framework (<https://doc.qt.io/>). To recompile or to extend the codes, the following components need to be installed:

- Qt-5 (static version for FEFLOW Plug-in): <https://www.qt.io/download>
- Eigen library: [http://eigen.tuxfamily.org/index.php?title=Main\\_Page](http://eigen.tuxfamily.org/index.php?title=Main_Page)
- Intel MKL: <https://software.intel.com/en-us/mkl>
- Visual Studio C++ or g++ as the compiler

## 2.5. Finite element code verifications

### 2.5.1. 1D Terzaghi's problem (Axisymmetric and 3D models)

A 1.0 mm radius and 10.0 m height soft soil column (Fig. 2-3) is laterally constrained. The bottom boundary is fixed with no vertical displacement and is impervious. The top boundary is free drained and is applied a pressure  $q = 98.1 \text{ kN/m}^2$ . The soil properties are:

- Isotropic
- Hydraulic conductivity  $k = 10^{-7} \text{ m/s}$
- The compressibility of water  $C_f = 10^{-10} \text{ m}^2/\text{kN}$
- The bulk modulus  $K = 500 \text{ kN/m}^2$
- Poisson's ratio  $\nu = 0.3$
- The shear modulus  $G = 230.77 \text{ kN/m}^2$
- Biot's coefficient  $\alpha = 1$
- The total consolidation time  $T = 100$  days and the number of calculation step is  $ns = 100$
- The porosity  $n = 0.6$
- The storativity  $S = nC_f + (\alpha - n)C_s = 6 \times 10^{-8} \text{ m}^2/\text{kN}$

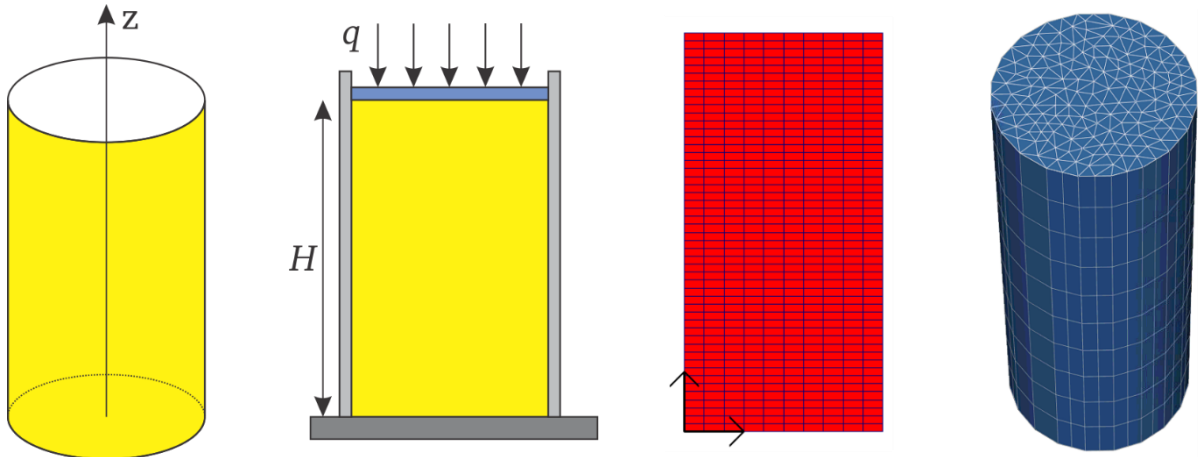


Fig. 2-3: Terzaghi's problem, 2D axisymmetric model and 3D model.

The initial excess pore pressure  $p_0 = q = 98.1 \text{ kN/m}^2$ . According to Terzaghi's solution (Verruijt, 2016), the EPWP at the time  $t$  and position  $z$  is:

$$p_{et} = p_0 \frac{4}{\pi} \sum_{j=1}^{\infty} \frac{-1^{j-1}}{2j-1} \cos \left[ (2j-1) \frac{\pi z}{2H} \right] \exp \left[ -(2j-1)^2 \frac{\pi^2 c_v t}{4H^2} \right] \quad (2.28)$$

where  $c_v$  is the consolidation coefficient.

$$c_v = \frac{k}{\gamma_f} \frac{K + \frac{4}{3}G}{\alpha^2 + \left(K + \frac{4}{3}G\right)S} = 8.236 \times 10^{-7} \text{ m}^2/\text{s} \quad (2.29)$$

Fig. 2-3 shows FE meshes of 2D axisymmetric and 3D models. Results of numerical models at the bottom boundary are compared to analytical solutions in Fig. 2-4. They are almost identical.

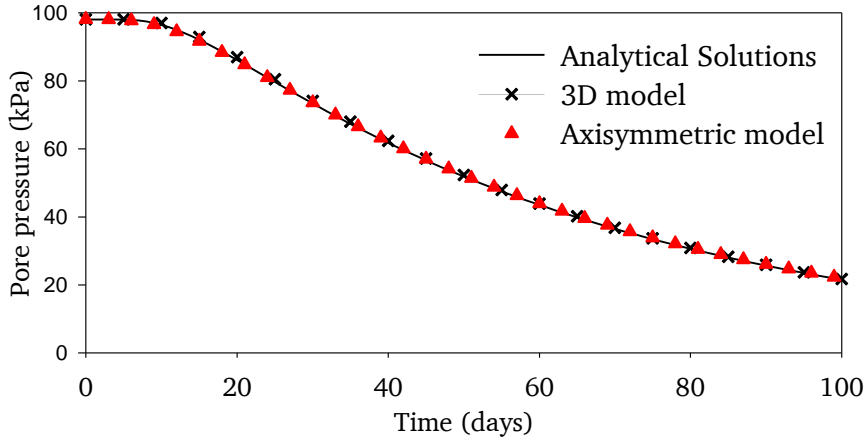


Fig. 2-4: Comparison results of the pore pressure at the bottom boundary among numerical models and the analytical solution.

### 2.5.2. De Leeuw's problem (Axisymmetric and 3D models)

A cylindrical soil sample that has the diameter  $2a = 2.0$  m and the height 1.0 m is constrained by two plates on the top and the bottom (Fig. 2-5). The sample is loaded by a uniform pressure  $q = 98.1$  kN/m<sup>2</sup> at the outer boundary, which is also the drained boundary. Immediately after applying the pressure  $q$ , the initial excess pore pressure is  $p_0 \sim q = 98.1$  kN/m<sup>2</sup>. The pore pressure at a position that has radius  $r$  and at the time  $t$  is calculated as (Verruijt, 2016):

$$p = \frac{p_0}{\gamma_w} \sum_{j=1}^{\infty} \frac{J_0(\xi_j) - J_0(\xi_j r/a)}{(1 - m_c \xi_j^2 - 1/4m_c) J_0(\xi_j)} \exp(-\xi_j^2 c_v t / a^2) \quad (2.30)$$

where  $J_0, J_1$  is the Bessel function of the first kind zero order and first order,  $\mu$  is the Poisson's ratio,  $S$  is storage specific;  $\alpha$  is the Biot's coefficient,  $K$  and  $G$  are the bulk modulus and the shear modulus respectively,  $c_v$  is the consolidation coefficient, and  $\xi_j$  for  $j=1,2,3\dots$  are the roots of function:

$$J_1(\xi_j) = 2m_c \xi_j J_0(\xi_j) \quad (2.31)$$

The parameter  $\eta$  is defined as:

$$\eta = (1 - \mu) / (1 - 2\mu) \quad (2.32)$$

The parameter  $m_c$  is:

$$m_c = \frac{1}{2} \eta \left[ \alpha^2 + S \left( K + \frac{1}{3} G \right) \right] / \alpha^2 \quad (2.33)$$

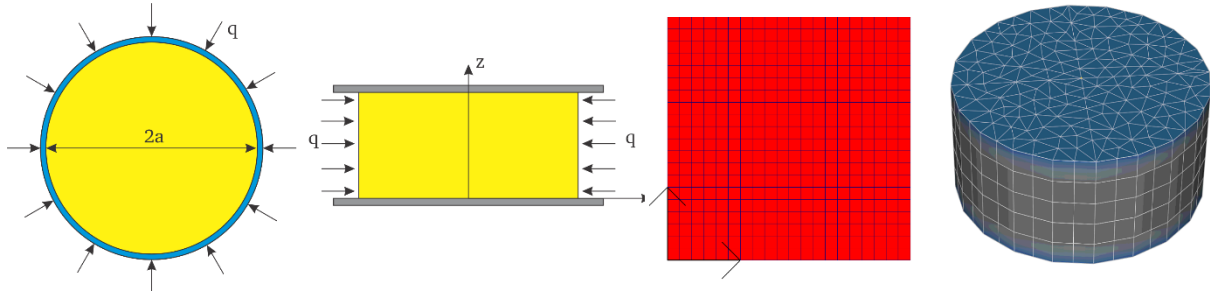


Fig. 2-5: De Leeuw's problem, 2D axisymmetric model and 3D models.

Soil properties are  $C_f = 10^{-7} \text{ m}^2/\text{kN}$ ,  $C_s = 0 \text{ m}^2/\text{kN}$ ,  $K = 500 \text{ kN/m}^2$ ,  $\nu = 0.1$ ,  $G = 545.45 \text{ kN/m}^2$ ,  $k_x = k_y = k_z = 10^{-9} \text{ m/s}$ ,  $n = 0.64$ ,  $\alpha = 1$ ,  $S = 6.4 \times 10^{-8} \text{ m}^2/\text{kN}$ ,  $m_v = 8.148 \times 10^{-4} \text{ m}^2/\text{kN}$ ,  $c_v = 0.0108 \text{ m}^2/\text{d}$ , simulation time  $t = 20 \text{ days}$  and the number of calculation steps  $ns = 200$ . Fig. 2-6 shows results of numerical models and the analytical solution. The differences are trivial.

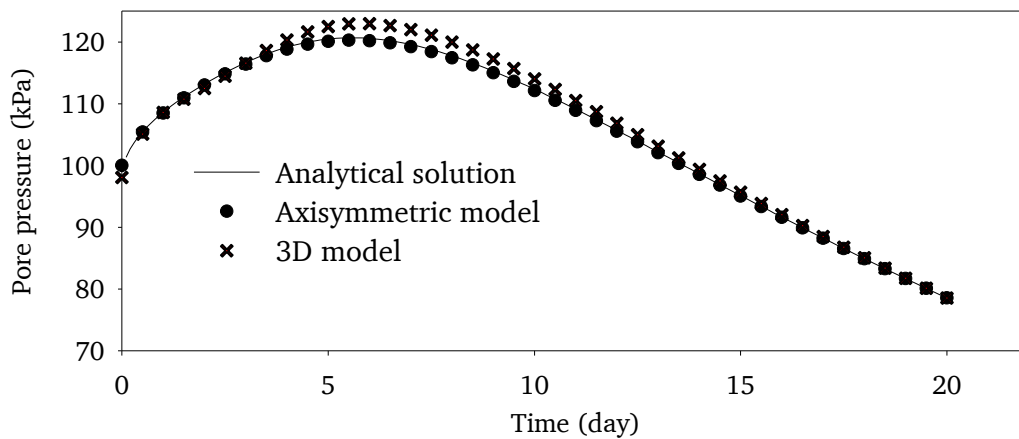


Fig. 2-6: Comparison results of the pore pressure at the centre among numerical models and the analytical solution.

### 2.5.3. Mandel's problem (3D model)

A square prism soil sample, which has a  $2a \times b$  dimension (Fig. 2-7), is constrained by two rigid plates on the top and on the bottom. Two sides of the x-direction are free and drained. The z-direction is also constrained.

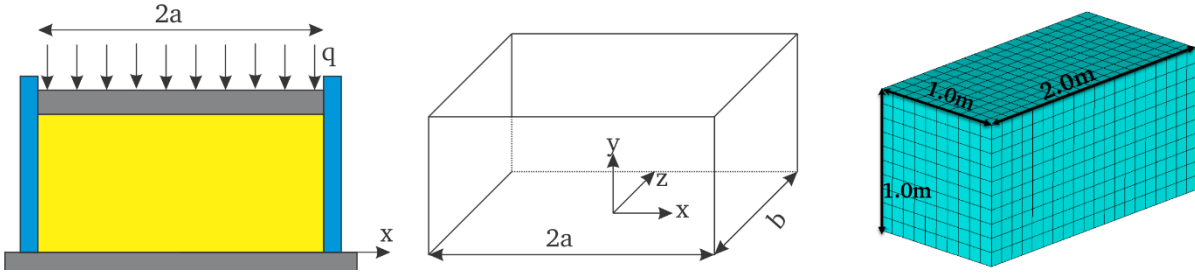


Fig. 2-7: Mandel's problem and 3D model

A constant force  $2F$  causes a uniform pressure  $q$  ( $\text{kN/m}^2$ ) on the top boundary. The excess pore pressure  $p$  at the position  $x$  (m) and at the time  $t$  (s) is calculated as (Abousleiman, Cheng, Cui, Detournay, & Roegiers, 1996):

$$p = \frac{2F}{aA_1} \sum_{i=1}^{\infty} \frac{\sin \beta_i}{\beta_i - \sin \beta_i \cos \beta_i} \times \left( \cos \frac{\beta_i x}{a} - \cos \beta_i \right) \times \exp \left( -\frac{\beta_i^2 c_v t}{a^2} \right) \quad (2.34)$$

where  $B$  is Skempton's coefficient,  $\nu_u = 0.5$  is the undrained Poisson's ratio,  $A_1$  and  $A_2$  are defined as equation 2.35 and 2.36, and  $\beta_i$  with  $i=1, 2, 3, \dots$  are the roots of function 2.37.

$$A_1 = 3 / B(1 + \nu_u) \quad (2.35)$$

$$A_2 = \alpha(1 - 2\nu) / (1 - \nu) \quad (2.36)$$

$$\tan \beta_i - \beta_i(A_1 / A_2) = 0 \quad (2.37)$$

Fig. 2-7 shows the 3D model of Mandel's problem. The soil properties are  $K=500 \text{ kN/m}^2$ ,  $\nu=0.1$ ,  $k=10^{-9} \text{ m/s}$ ,  $q=100 \text{ kN/m}^2$ ,  $c_s=0 \text{ m}^2/\text{kN}$ ,  $C_f=10^{-7} \text{ m}^2/\text{kN}$ ,  $n=0.64$ ,  $\Delta t=1000 \text{ s}$  and the total calculation step  $ns=200$ . Comparisons between numerical results and analytical results are presented in Fig. 2-8.

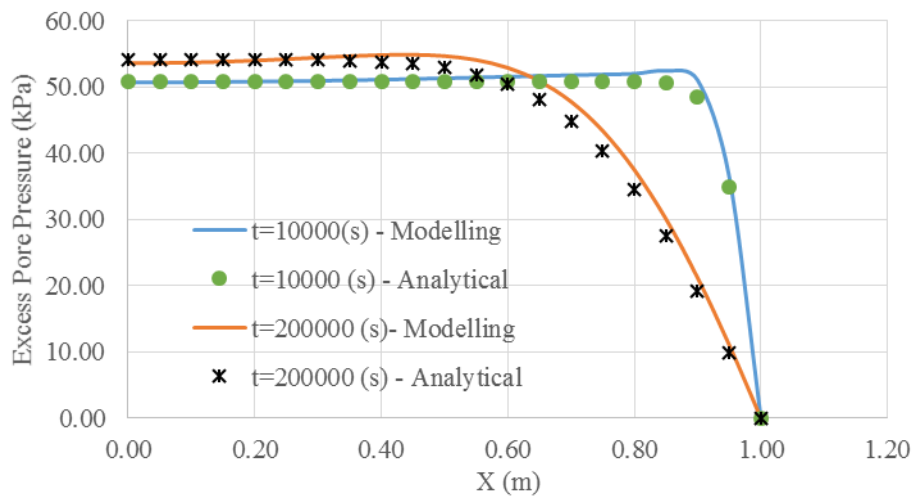


Fig. 2-8: Comparison of pore pressure results at  $t = 10000 \text{ s}$  and  $t = 200000 \text{ s}$  between the analytical solution and 3D model

### 2.5.4. Cryer's problem (3D model)

A sphere soil sample, which has the radius  $a = 1.0$  m, is compressed by a uniform load  $q$  (kN/m<sup>2</sup>) via the outer boundary (Fig. 2-9). The outer boundary is drained. The initial pore pressure is  $p_0$ .

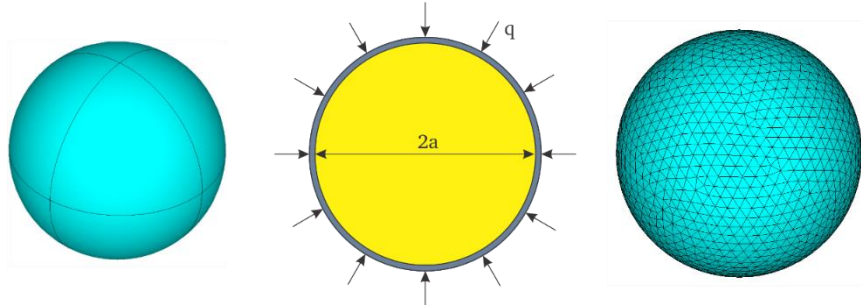


Fig. 2-9: Cryer's problem and 3D model

The pore pressure at the centre of the soil sample at the time  $t$  (s) is calculated as (Verruijt, 2016):

$$\frac{p_c}{p_0} = \eta \sum_{j=1}^{\infty} \frac{\sin \xi_j - \xi_j}{(\eta - 1) \sin \xi_j + \eta \xi_j \cos \xi_j / 2} \exp(-\xi_j^2 c_v t / a^2), \text{ where:} \quad (2.38)$$

- $\xi_j$  are the positive roots of the equation  $(1 - \eta \xi_j^2) \tan \xi_j - \xi_j = 0$
- The parameter  $\eta = \frac{K + 4G / 3}{2G} (1 + KS / \alpha^2)$
- The other variables are similar to equation 2.31.

Soil properties are  $K = 500$  kN/m<sup>2</sup>,  $\nu = 0.1$ ,  $k = 10^{-9}$  m/s,  $q = 100$  kN/m<sup>2</sup>,  $C_s = 0$  m<sup>2</sup>/kN,  $C_f = 10^{-7}$  m<sup>2</sup>/kN,  $n = 0.64$ ,  $\Delta t = 86400$  s and  $ns = 100$ . Fig. 2-10 shows a perfect fit between the 3D model and the analytical solution.

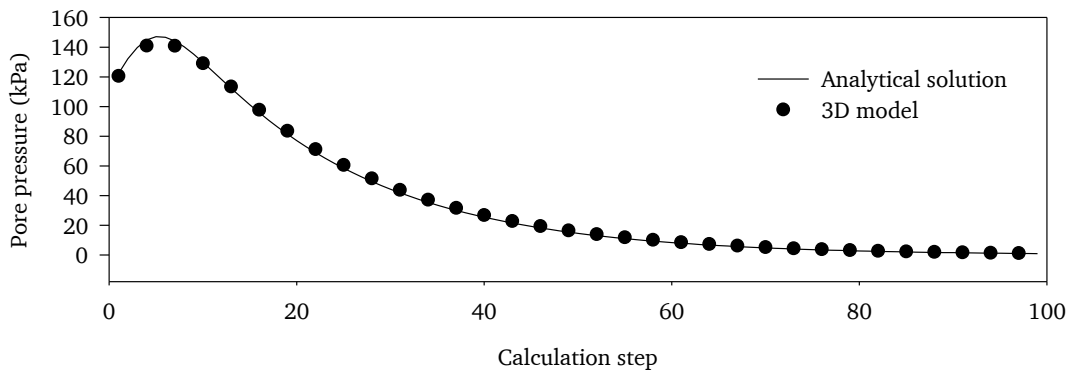


Fig. 2-10: Pore pressure at the centre of the sphere, comparison between the 3D model and the analytical solution.



---

---

### **3. Fully hydro-mechanical coupled Plug-in (SUB+) in FEFLOW for analysis of land subsidence due to groundwater extraction**

---

This chapter is reproduced from: Pham HT, Rhaak W, Schuster V, Sass I. *Fully hydro-mechanical coupled Plug-in (SUB+) in FEFLOW for analysis of land subsidence due to groundwater extraction*. SoftwareX. 2019 (Pham, Rhaak, Schuster, & Sass, 2019).



## Original software publication

## Fully hydro-mechanical coupled Plug-in (SUB+) in FEFLOW for analysis of land subsidence due to groundwater extraction



Hung Tien Pham\*, Wolfram Rühaak, Valerian Schuster, Ingo Sass

*Geothermal Science and Technology, Institute of Applied Geosciences, Technische Universität Darmstadt, Germany*

## ARTICLE INFO

## Article history:

Received 9 July 2018

Received in revised form 7 November 2018

Accepted 8 November 2018

## Keywords:

Groundwater modelling

Land subsidence

FEFLOW Biot's theory

Fully coupled hydro-mechanics

## ABSTRACT

Extensive groundwater extraction leads to the drawdown of the groundwater table, which can increase the stress of soils and lead to land subsidence. Analyses of land subsidence generally require numerical models based on the poroelasticity theory. FEFLOW is a well-known commercial finite element software that is one of the most widely used for groundwater, heat transfer, and transport modelling. However, it is not capable of modelling land subsidence. Here, we introduce a plug-in called SUB+ and a pre-processing software PSUB that can be used for fully coupled land subsidence analyses using the poroelasticity theory. The plug-in and the software are developed using C++ with Qt-Framework. The Eigen and Intel MKL libraries are used for matrix operations and the sparse matrix solver. Although FEFLOW is closed-source, SUB+ and PSUB are open-source and available on GitHub.

© 2018 The Authors. Published by Elsevier B.V. This is an open access article under the CC BY license (<http://creativecommons.org/licenses/by/4.0/>).

## Code metadata

Current code version	VI
Permanent link to code/repository used of this code version	<a href="https://github.com/ElsevierSoftwareX/SOFTX_2018_104">https://github.com/ElsevierSoftwareX/SOFTX_2018_104</a>
Legal Code License	MIT, LGPL
Code versioning system used	None
Software code languages, tools, and services used	C++, OpenGL
Compilation requirements, operating environments & dependencies	Qt-5 static, Eigen Library, Intel MKL
If available Link to developer documentation/manual	<a href="https://github.com/pham-hung/Subsidence_FEFLOW/blob/master/Documents/User_manual.pdf">https://github.com/pham-hung/Subsidence_FEFLOW/blob/master/Documents/User_manual.pdf</a>
Support email for questions	<a href="mailto:pham@geo.tu-darmstadt.de">pham@geo.tu-darmstadt.de</a>

## Software metadata

Current software version	VI
Permanent link to executables of this version	<a href="https://github.com/pham-hung/Subsidence_FEFLOW">https://github.com/pham-hung/Subsidence_FEFLOW</a>
Legal Software License	MIT, LGPL
Computing platforms/Operating Systems	Windows x64
Installation requirements & dependencies	
If available, link to user manual – if formally published include a reference to the publication in the reference list	<a href="https://github.com/pham-hung/Subsidence_FEFLOW/blob/master/Documents/User_manual.pdf">https://github.com/pham-hung/Subsidence_FEFLOW/blob/master/Documents/User_manual.pdf</a>
Support email for questions	<a href="mailto:pham@geo.tu-darmstadt.de">pham@geo.tu-darmstadt.de</a>

## 1. Motivation and significance

The topic of land subsidence due to groundwater extraction is an important issue in many regions all over the world, for

example, Shanghai China [1], Jakarta Indonesia [2], Bangkok Thailand [3], Mexico City Mexico [4], Mekong Delta Vietnam [5], California USA [6], and Northeastern Saxony Germany [7]. Usually, land subsidence models are developed by hydrogeologists under an assumption that there is no horizontal deformation [6]. Hence, land subsidence problems can be solved using two uncoupled models, or two-step models. First, a groundwater model is used to

\* Corresponding author.

E-mail address: [pham@geo.tu-darmstadt.de](mailto:pham@geo.tu-darmstadt.de) (H.T. Pham).

obtain changes in the groundwater level that lead to differences in the effective stress. Then, the settlement magnitude is calculated using an analytical method or a numerical model. This approach is typically used in the field of hydrogeology because is easy to implement, especially with the finite difference method – for instance, MODFLOW with interbed storage packages [8].

However, land subsidence is a three-dimensional (3D) problem. Ignoring horizontal deformation can lead to overestimating the magnitude of the settlement, particularly in the vicinity of pumping wells [6]. In a review of regional land subsidence accompanying groundwater extraction, Galloway and Burbey [6] stated that models based on the poroelasticity theory are necessary to analyse the realistic behaviour of aquifer settings. The poroelasticity theory was first initially developed by Biot [9] based on the one-dimensional consolidation theory of Terzaghi. Then, it was later further extended by Biot and Verruijt [10,11].

FEFLOW is a commonly used finite element software for groundwater, heat transfer, and transport modelling purpose, however, FEFLOW is not capable of modelling land subsidence. FEFLOW provides an API (application programming interface) to develop plug-ins. Based on the poroelasticity theory, we developed a plug-in, named SUB+, that can not only be used for land subsidence problems but also general consolidation analyses. Furthermore, a software package called PSUB was developed to visualise results from SUB+. With SUB+, FEFLOW acts as a pre-processing tool. The geometry, the mesh, input material parameters, time step setting, and boundary conditions are processed in FEFLOW. Subsequently, SUB+ uses these data to assemble the global matrix and solve the system of equations. Finally, results from SUB+ are saved as ASCII files and are visualised by using PSUB.

SUB+ and PSUB were developed using C++ with the cross-platform framework Qt. The source code can be compiled both on Windows and Linux. Matrix operations and the sparse matrix solver are based on Eigen and Intel MKL libraries [12,13], which ensure that SUB+ is fast and reliable. SUB+ is verified with analytical solutions of Terzaghi and Deleeuw's problems. For Windows end-users, SUB+ and PSUB are provided as a single .dll and .exe file, respectively. All third-party libraries are linked statically. Thus, Windows users can use SUB+ and PSUB immediately without any configuration.

This paper outlines the poroelasticity theory and main features of SUB+ and PSUB. Details about the installation, the theory, verifications, and the user manual are provided separately as supplementary materials.<sup>1</sup>

## 2. Theory

We introduce the poroelasticity theory (or Biot's theory), which is used to develop SUB+. Detailed information is found in the works of Biot [9,10,14,15], Verruijt [11], and in the supplementary materials.<sup>1</sup>

### 2.1. Fully coupled poroelasticity theory

We consider a representative element in three dimensions (Fig. 1), where the displacements in  $x$ ,  $y$ ,  $z$ -direction are denoted as  $u$ ,  $v$ , and  $w$  respectively. The pore water pressure is denoted as  $p$ , and the total head is  $H$ .

The total head is related to the pore pressure by:

$$H = p\gamma_w + Ele \quad (1)$$

where  $\gamma_w$  is the unit weight of water and  $Ele$  is the elevation.

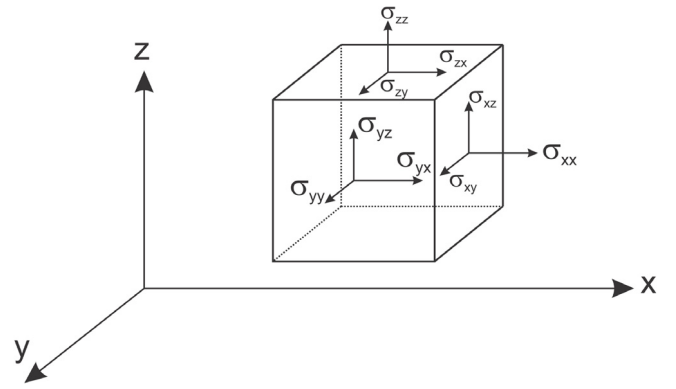


Fig. 1. A representative element in the Cartesian coordinate system with total stress components.

The system equation of the poroelasticity theory includes the storage equation (or the groundwater equation) and the stress equilibrium equations. The storage equation is defined as:

$$\alpha \frac{\partial \varepsilon}{\partial t} + S \frac{\partial H}{\partial t} - \frac{\partial}{\partial x} \left( k_x \frac{\partial H}{\partial x} \right) - \frac{\partial}{\partial y} \left( k_y \frac{\partial H}{\partial y} \right) - \frac{\partial}{\partial z} \left( k_z \frac{\partial H}{\partial z} \right) = 0 \quad (2)$$

where  $\varepsilon = \varepsilon_{xx} + \varepsilon_{yy} + \varepsilon_{zz}$  is the total volume strain;  $\alpha$  is the Biot's coefficient;  $t$  is the time;  $S$  is the storativity;  $k_i$  is the hydraulic conductivity in  $x$ ,  $y$ ,  $z$ -direction; and  $\varepsilon_{ii}$  ( $i = x, y, z$ ) is the axial strain components. The storativity is defined as:

$$S = nC_f + (\alpha - n)C_s \quad (3)$$

where  $n$  is the porosity;  $C_f$  is the compressibility of water;  $C_s$  is the compressibility of solid grains (or the soil skeletons).

The stress equilibrium equations are:

$$\begin{aligned} \frac{\partial \sigma'_{xx}}{\partial x} + \frac{\partial \sigma'_{yx}}{\partial y} + \frac{\partial \sigma'_{zx}}{\partial z} + \alpha \frac{\partial p}{\partial x} - f_x &= 0 \\ \frac{\partial \sigma'_{xy}}{\partial x} + \frac{\partial \sigma'_{yy}}{\partial y} + \frac{\partial \sigma'_{zy}}{\partial z} + \alpha \frac{\partial p}{\partial y} - f_y &= 0 \\ \frac{\partial \sigma'_{xz}}{\partial x} + \frac{\partial \sigma'_{yz}}{\partial y} + \frac{\partial \sigma'_{zz}}{\partial z} + \alpha \frac{\partial p}{\partial z} - f_z &= 0 \end{aligned} \quad (4)$$

where  $\sigma_{ij}$  and  $\sigma'_{ij}$  are the total stress and the effective stress components respectively and  $f_i$  is the body forces. The total stress is the sum of the effective stress and the pore pressure:

$$\sigma_{ij} = \sigma'_{ij} + \alpha \delta p = \sigma'_{ij} + \alpha \delta (H - Ele) \gamma_w \quad (5)$$

where  $\delta$  is the Kronecker delta.

The relation between the effective stress and the strain follows Hook's law:

$$\begin{aligned} \sigma'_{xx} &= - \left( K + \frac{4}{3}G \right) \frac{\partial u}{\partial x} - \left( K - \frac{2}{3}G \right) \frac{\partial v}{\partial y} - \left( K - \frac{2}{3}G \right) \frac{\partial w}{\partial z} \\ \sigma'_{yy} &= - \left( K + \frac{4}{3}G \right) \frac{\partial v}{\partial y} - \left( K - \frac{2}{3}G \right) \frac{\partial u}{\partial x} - \left( K - \frac{2}{3}G \right) \frac{\partial w}{\partial z} \\ \sigma'_{zz} &= - \left( K + \frac{4}{3}G \right) \frac{\partial w}{\partial z} - \left( K - \frac{2}{3}G \right) \frac{\partial u}{\partial x} - \left( K - \frac{2}{3}G \right) \frac{\partial v}{\partial y} \\ \sigma'_{xy} &= \sigma'_{yx} = -G \left( \frac{\partial u}{\partial y} + \frac{\partial v}{\partial x} \right); \\ \sigma'_{xz} &= \sigma'_{zx} = -G \left( \frac{\partial u}{\partial z} + \frac{\partial w}{\partial x} \right); \\ \sigma'_{yz} &= \sigma'_{zy} = -G \left( \frac{\partial v}{\partial z} + \frac{\partial w}{\partial y} \right) \end{aligned} \quad (6)$$

where  $K = 1/C_m$  is the bulk modulus;  $C_m$  is the compressibility of porous media;  $G$  is the shear modulus.

<sup>1</sup> The supplementary material available in the github link [https://github.com/pham-hung/Subsidence\\_FEFLOW/blob/master/Documents/User\\_manual.pdf](https://github.com/pham-hung/Subsidence_FEFLOW/blob/master/Documents/User_manual.pdf).

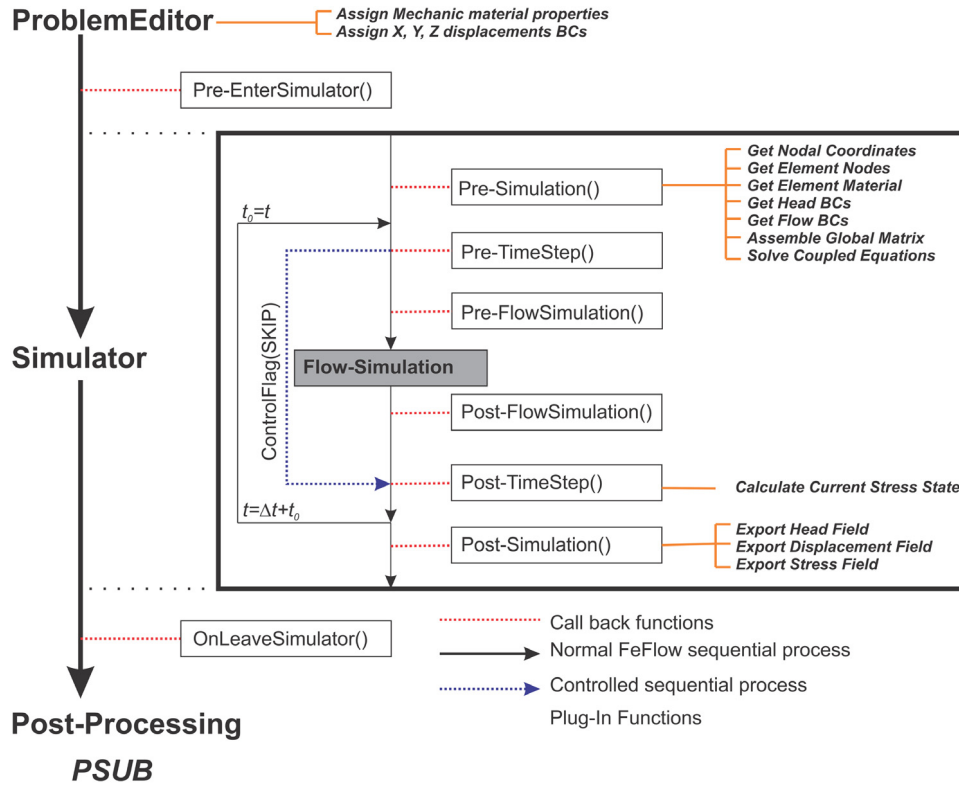


Fig. 2. FEFLOW program flow and main functions of SUB+ Plug-In.

Eqs. (2) and (4) are the full-coupled equations that contain four variables: three displacements in  $x, y, z$ -direction and the pore pressure  $p$  (or the total head  $H$ ). Eq. (2) implies that the change of the total volume, which has two components  $\alpha(\partial\varepsilon/\partial t)$  and  $S(\partial H/\partial t)$ , is equal to the amount of water that exits the element  $\nabla(k\nabla H)$ . The former component is caused by changes in the effective stress, and the latter component is derived from changes in the pore pressure.

### 2.2. Uncoupled approach – a simple form of the poroelasticity theory

In conventional groundwater theory, it is assumed that there is no horizontal deformation. If the gravity direction is the negative  $z$ -direction, we have:

$$\varepsilon_{xx} = \varepsilon_{yy} = 0 \quad (7)$$

If porous media behaves as an elastic material, then:

$$\begin{aligned} \varepsilon = \varepsilon_{zz} &= -m_v \sigma'_{zz} = -m_v (\sigma_{zz} - \alpha p) \\ &= -m_v [\sigma_{zz} - \alpha \gamma_w (H - Ele)] \end{aligned} \quad (8)$$

where  $m_v = 1/(K + 4G/3)$  is the confined compressibility of porous media. From Eq. (8), we have:

$$\alpha \frac{\partial \varepsilon}{\partial t} = -\alpha m_v \frac{\partial \sigma_{zz}}{\partial t} + \alpha^2 m_v \frac{\partial H}{\partial t} \quad (9)$$

Substituting Eq. (9) into Eq. (2) gives:

$$(\alpha^2 m_v + S) \frac{\partial H}{\partial t} = \nabla(k\nabla H) + m_v \frac{\partial \sigma_{zz}}{\partial t} \quad (10)$$

If the total stress is assumed to be constant over time, the second term of the right-hand side is zero, and Eq. (10) becomes:

$$S_s \frac{\partial H}{\partial t} = \nabla(k\nabla H) \quad (11)$$

Eq. (11) is the conventional groundwater equation that is also used in FEFLOW. The new parameter  $S_s$  includes the compressibility of water, solid grains, and porous media. Eq. (11) has only the total head as the variable or it is an uncoupled form of the coupled equation system of Biot's theory. The land subsidence problems now are solved in two steps:

- Step 1: Solve Eq. (11) to obtain results of the total head field for each time step.
- Step 2: Calculate vertical deformation for each time step according to changes in the water head.

Uncoupled models are suitable when there is no horizontal deformation and the total vertical stress is constant. In some cases, when horizontal movements are large (e.g. near pumping wells), this approach overestimates 1D settlement [6].

### 2.3. Finite element approximation

Applying the Galerkin approximation method with the backward integration scheme for Eqs. (2) and (4), the coupled equations are written under the matrix form:

$$\begin{bmatrix} K & L \\ -L^T & M + \Delta t P \end{bmatrix} \begin{Bmatrix} \Delta d \\ \Delta H \end{Bmatrix} = \begin{Bmatrix} \Delta F \\ -\Delta t P \times H_0 + \Delta t Q \end{Bmatrix} \quad (12)$$

where  $\Delta t$  is the calculation time step;  $K$  is the matrix for the displacement field,  $M$  and  $P$  are the matrices for the transient field;  $L$  is the coupled matrix;  $\Delta d = \{\Delta u \ \Delta v \ \Delta w\}^T$  is the incremental displacement vector;  $\Delta H$  is the incremental water head vector;  $H_0$  is the water head of the previous calculation step;  $\Delta F$  is the incremental load vector; and  $Q$  is the extract rate vector.

### 3. SUB+ Plug-in and PSUB description

Fig. 2 shows the program flow of a finite element model in FEFLOW. FEFLOW has three main modules:

- Problem editor: To edit geometry, input parameters, and boundary conditions of the model.
- Simulator: To solve systems of equations.
- Post-Processing: To visualise results.

SUB+ is called in the problem editor phase and in the simulator phase. Whereas, PSUB is an alternative to the post-processing phase.

The main functions of SUB+ are:

- In the problem editor phase: SUB+ creates a saved folder, a setting folder, user nodal and elemental data to assign boundary conditions and input parameters for the mechanical field. Other input data for the hydro field is processed in FEFLOW in a regular way.
- During the simulation phase: SUB+ gathers all information related to nodes, elements, material properties, calculation time, and boundary conditions. Then, SUB+ uses these data to assemble the global coupled matrix and solve the system of equations. Finally, SUB+ calculates element stress and saves results as ASCII files in the saved folder.

PSUB imports output data generated by SUB+ and visualises them. PSUB can scale the coordinate, scale the deformation, show results of a specific calculation step or make an animation. Step-by-step instructions for using SUB+ and PSUB are provided in the *User\_manual.pdf* file.

### 3.1. Assembling the global matrix using multi-threads

Two specific techniques are used to increase the speed of SUB+. The first is for assembling the global matrix in Eq. (12) using multi-threads. The second is for applying Dirichlet boundary conditions directly to element stiffness matrices before they are assembled into the global matrix.

Fig. 3 shows how SUB+ assembles parallel the global matrix. The number of available threads is  $m$ , and the number of elements is  $noe$ . Each thread will loop over  $n$  elements to calculate  $n$  element stiffness matrices. Each coefficient of an element stiffness matrix is stored as an element of a vector. With  $m$  available threads,  $m$  vectors are created. Elements of vectors are tuple type. A vector element contains a row index  $i$ , a column index  $j$ , and a coefficient from an element matrix. When all threads finish, all vectors are concatenated as a single vector, and the global matrix is generated by using this vector.

### 3.2. Applying dirichlet boundary conditions for each element stiffness matrix

The global matrix is sparse. Only non-zero values are stored with the row and column indices. If Dirichlet boundary conditions

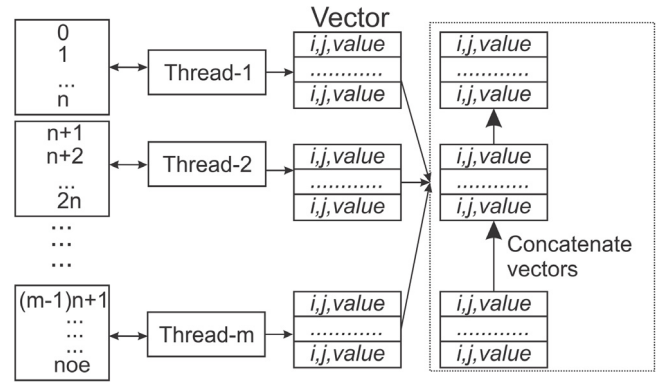


Fig. 3. Multi-threading assembly the global matrix algorithm.

are applied after assembling the global matrix, the number of non-zero coefficients changes. It is time-consuming and not memory efficient. To overcome this difficulty, Dirichlet boundary conditions are applied to each element stiffness matrix before it is assembled into the global matrix. Since element matrices are small dense matrices, this operation is trivial.

## 4. Example

In this section, we consider an aquifer system that has 14 layers (similar to the situation in the Vietnamese Mekong Delta [5]). The model data is given in Table 1, where  $k_{xx}$ ,  $k_{yy}$ ,  $k_{zz}$  are the hydraulic conductivity ( $k_{xx} = 3k_{zz}$ ), and  $K$  is the bulk modulus. All layers are considered to have the same porosity  $n = 0.6$  and the compressibility of solid grain  $C_s = 1 \times 10^{-10}$  kN/m<sup>2</sup>.

The initial total head of the system is 0.0 m. The simulation time is ten years and the number of time steps is 365. The boundary conditions, the model size, and the extract well locations are shown in Fig. 4. Each well has 200 m<sup>3</sup>/d extraction rate.

The number of nodes is 23636, the total degrees of freedom is 94544, and the number of elements is 43484. In this specific example, for each calculation step, SUB+ takes approximately two seconds to assemble the global matrix and another four seconds for the sparse matrix solver on the author's computer (Xeon 1230v5, 4 cores, 3.4 Ghz).

Fig. 5 shows the total head and the land subsidence magnitude at the final analysis step using PSUB. The maximum decrease of the groundwater water head is  $-2.68$  m, and the maximum surface settlement is 0.216 m. Although all extract wells have the same pumping rate, areas that are far away from the constant total head boundaries (the total head is zero) have the largest subsidence.

Table 1  
Input data for the aquifer system.

Layer	Type	$k_{xx} = k_{yy}$ (m/d)	$k_{zz}$ (m/d)	Poisson's Ratio	$K$ (kN/m <sup>2</sup> )	Thickness (m)	Top Elevation (m)
1	Aquitard	3.3e-4	1.1e-4	0.4	2991	18	-9
2	Aquifer	8.2	2.73	0.3	56277	24	-27
3	Aquitard	1.1e-3	3.6e-4	0.4	20468	22	-51
4	Aquifer	46.8	15.6	0.3	51587	14	-73
5	Aquitard	1.8e-2	6e-3	0.4	48611	39	-87
6	Aquifer	59.5	19.8	0.3	106732	13	-129
7	Aquitard	5.7e-7	1.9e-4	0.4	77778	39	-139
8	Aquifer	11.3	3.77	0.3	116801	21	-178
9	Aquitard	3.7e-3	1.23e-3	0.4	109546	44	-199
10	Aquifer	67.5	22.5	0.3	114638	18	-243
11	Aquitard	2.6e-3	8.67e-4	0.4	131827	38	-261
12	Aquifer	39.5	13.17	0.3	108605	21	-299
13	Aquitard	1.1e-3	3.67e-4	0.4	146751	41	-320
14	Aquifer	6.8	2.27	0.3	71982	59	-361

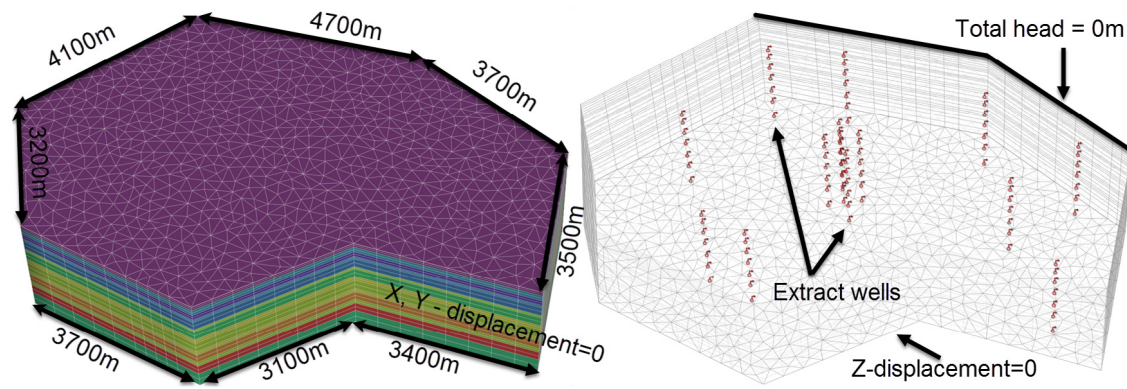


Fig. 4. Geometry and boundary conditions of the aquifer system with 14 layers and extraction wells.

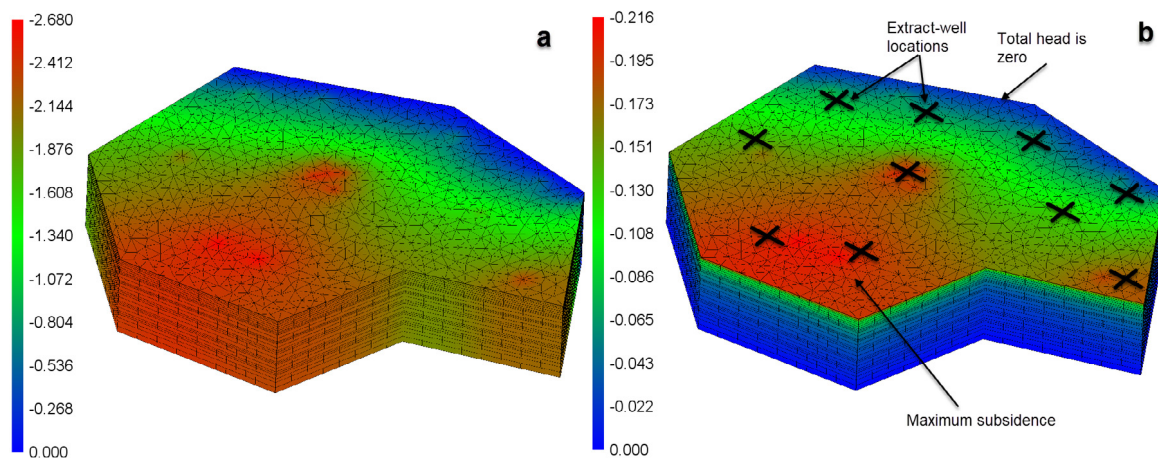


Fig. 5. Simulation results after ten years ( $z$ -coordinate is exaggerated five times); In (a) the total head (m) is displayed while (b) shows the magnitude of land subsidence (m).

## 5. Impact and conclusions

The plug-in SUB+ and the program PSUB provide a simple, powerful, and effective tool to analyse land subsidence problems in FEFLOW based on Biot's theory. Many available groundwater models in FEFLOW now can benefit from SUB+ and PSUB. When land subsidence analyses are needed with those models, only parameters and boundary conditions for the mechanical field are added. The other information is untouched.

Moreover, applications of SUB+ and PSUB are not limited to land subsidence analyses; they can be used to solve other problems that share the same theory. For instance, consolidation analyses of soft soil foundations, or they can be extended to support thermal-hydro-mechanical (THM) modelling. Future developments will include the extension of SUB+ to consider nonlinear materials and to be used from other well-known groundwater codes, such as, for instance, MODFLOW, OpenGeoSys, and Hydrus. A standalone version is planned.

## Acknowledgment

Hung Pham was funded by NaWaM, a program of DAAD Germany.

## References

- [1] Xu Y-S, Shen S-L, Ren D-J, Wu H-N. Analysis of factors in land subsidence in Shanghai: a view based on a strategic environmental assessment. *Sustainability* 2016;8(6):573.
- [2] Abidin HZ, Andreas H, Gumilar I, Fukuda Y, Pohan YE, Deguchi T. Land subsidence of Jakarta (Indonesia) and its relation with urban development. *Nat Hazards* 2011;59(3):1753.
- [3] Phien-wej N, Giao PH, Nutalaya P. Land subsidence in Bangkok, Thailand. *Eng Geol* 2006;82(4):187–201.
- [4] Dalia O-Z, Adrian O-G. Evolution of long-term land subsidence near Mexico City: Review, field investigations, and predictive simulations. *Water Resour Res* 2010;46(1).
- [5] Minderhoud PSJ, Erkens G, Pham VH, Bui VT, Erban L, Kooi H, et al. Impacts of 25 years of groundwater extraction on subsidence in the Mekong delta, Vietnam. *Environ Res Lett* 2017;12(6):064006.
- [6] Galloway DL, Burbey TJ. Review: Regional land subsidence accompanying groundwater extraction. *Hydrogeol J* 2011;19(8):1459–86.
- [7] Wolkersdorfer C, Thiem G. Ground water withdrawal and land subsidence in northeastern Saxony (Germany). *Mine Water Environ* 1999;18(1):81–92.
- [8] Leake S, D. Galloway. MODFLOW ground-water model: User guide to the subsidence and aquifer-system compaction package (SUB-WT) for water-table aquifers. 2007.
- [9] Biot MA. General theory of three-dimensional consolidation. *J Appl Phys* 1941;12(2):155–64.
- [10] Biot M. General solutions of the equations of elasticity and consolidation for a porous material. *J Appl Mech* 1956;23(1):91–6.
- [11] Verruijt A. *PorosityElasticity*: <http://geo.verrijt.net/>. 2016.
- [12] Intel(R). *Intel parallel studio xe*. 2011.
- [13] Guennebaud G, Jacob B. *Eigen V3*. 2010.
- [14] Biot MA. Theory of elasticity and consolidation for a porous anisotropic solid. *J Appl Phys* 1955;26(2):182–5.
- [15] Biot MA. Mechanics of deformation and acoustic propagation in porous media. *J Appl Phys* 1962;33(4):1482–98.

---

#### **4. Fully coupled analysis of consolidation by prefabricated vertical drains with applications of constant strain rate tests**

---

This chapter is reproduced from: Pham, H.T., Rühaak, W., Nguyen, O.C., Ngo, D.H., Sass, I., 2019. *Fully coupled analysis of consolidation by prefabricated vertical drains with applications of constant strain rate tests: case studies and open-source program*. Geotextiles and Geomembranes. doi:<https://doi.org/10.1016/j.geotexmem.2019.12.009> (Pham, Rühaak, Ngo, Nguyen, & Sass, 2019).



ELSEVIER

Contents lists available at ScienceDirect

## Geotextiles and Geomembranes

journal homepage: [www.elsevier.com/locate/geotextmem](http://www.elsevier.com/locate/geotextmem)

# Fully coupled analysis of consolidation by prefabricated vertical drains with applications of constant strain rate tests: Case studies and an open-source program

Hung Tien Pham<sup>a,\*</sup>, Wolfram Rühaak<sup>b</sup>, Dong Huy Ngo<sup>c</sup>, Oanh Cong Nguyen<sup>d</sup>, Ingo Sass<sup>a</sup>

<sup>a</sup> Geothermal Science and Technology, Institute of Applied Geosciences, Technische Universität Darmstadt, Germany

<sup>b</sup> Bundesgesellschaft für Endlagerung mbH (BGE), Germany

<sup>c</sup> School of Civil Engineering, Institute of Engineering, Suranaree University of Technology, Thailand

<sup>d</sup> Division of Soil Mechanics and Foundation Engineering, Southern Institute of Water Resource Research, Ho Chi Minh City, Viet Nam

## ARTICLE INFO

## Keywords:

Finite element method  
Constant rate of strain test  
Prefabricated vertical drains  
CONAXIS  
Nonlinear poroelasticity theory

## ABSTRACT

The paper proposes a new approach to use measured data of the constant strain rate test (CRST) for analysis of consolidation by prefabricated vertical drains (PVDs). Each PVD has an influence zone that idealised as a unit cell. Consolidation behaviour of a unit cell is studied with an axisymmetric finite element (FE) model based on Biot's theory. From a CRST data, ASTM-D4186 or the back-analysis method is used to obtain stress-dependent parameters for the model. An open-source FE software named CONAXIS was developed for these purposes. Data from two projects in Mekong Delta Vietnam were used in this study. In the first project, nine CRSTs with various depths from a borehole were conducted. Two tests were chosen to be simulated using the proposed approach implemented in CONAXIS and the soft soil model in PLAXIS for validation and comparison purposes. Comparing to the laboratory data, CONAXIS gave more accurate results than PLAXIS. Then CONAXIS was used to calculate the settlement of the ground surface during the construction process with different scenarios. For the second project, six CRSTs from three boreholes were used to set up the model in CONAXIS. Modelled results of both projects showed good agreements with field monitoring data.

## 1. Introduction

The one-dimensional (1D) theory of consolidation was proposed by Terzaghi (1943). Biot generalised Terzaghi's theory for three-dimensional (3D) problems so-called the poroelasticity theory, which was later further extended by Biot and Verruijt (Biot, 1941, 1955; Verruijt, 2016). It has been integrated into various commercial software such as PLAXIS, ABAQUS, Sigma/W. Numerical solutions of the poroelasticity theory have been studied by many researchers in different aspects, for instances, the numerical stability (Reed, 1984), the pore pressure oscillation (Murad and Loula, 1994), the convergence of finite element approximation (Haga et al., 2012), the time step scheme (Sheng and Sloan, 2003). However, previous works usually relied on constant values of the poroelastic model parameters (i.e., the bulk modulus, the hydraulic conductivity).

Parameters for consolidation analyses are usually obtained from the odometer test (incremental loading test – ILT), which spends approximately a week for a test. In 1969, Smith and Wahls proposed a new

consolidation test by applying a constant rate of strain (CRS) that shortens the testing time to one to two days. Moreover, test data is continuous and is recorded automatically. Because of these advantages, the CRST was standardised in the early '80s as ASTM-D4186 based on the theory developed by Wissa et al. (ASTM/D4186M-12e1, 2014; Wissa, 1971). In the CRST, the compressibility and the vertical consolidation coefficient of soil samples change continuously during the test in accordance with the applied stress. Based on those values, parameters for the poroelasticity theory can be determined if Poisson's ratio is known. Hence, these parameters depend on the vertical effective stress or the void ratio.

Previous studies on the CRST can be categorised into two main groups that are the CRST itself and usage of the CRST for consolidation analyses. The first group focuses on proper strain rates (Ozer et al., 2011), comparisons between the CRST and the ILT (Fantaziu and Musat, 2014; Jia, 2010), evaluating the theory to interpret results from the CRST or modelling the CRST using constitute models for the geotechnical field such as the soft soil (SS) model and the modified Cam-

\* Corresponding author.

E-mail address: [pham@geo.tu-darmstadt.de](mailto:pham@geo.tu-darmstadt.de) (H.T. Pham).

<https://doi.org/10.1016/j.geotextmem.2019.12.009>

Received 24 May 2019; Received in revised form 12 December 2019; Accepted 13 December 2019

0266-1144/ © 2019 Elsevier Ltd. All rights reserved.

Clay (MCC) model (Jia, 2010). Table 1 shows some examples of the second group. Most of those studies were to predict settlement during the consolidation process in projects that used prefabricated vertical drains (PVDs) as the soft soil improvement method. Finite difference models or analytical solutions for unit cells were utilised; input parameters were horizontal and vertical consolidation coefficients ( $c_h$  and  $c_v$ ) obtained from  $e$ -log( $\sigma'$ ) curves, where  $e$  is the void ratio and  $\sigma'$  is the effective stress. With this approach, data of the CRST is processed similarly to the ILT. Hence, the advantages of the CRST are not fully considered. Dependence of the bulk modulus and the hydraulic conductivity on the effective stress obtained from continuous data of the CRST has not been taken into account. Additionally, source codes for those models are closed-source; they were used only by the authors.

Various studies on using the finite element method to analyse behaviours of PVD systems have been published (Hiep and Chung, 2018; Kumarage and Gnanendran, 2019; Liu and Rowe, 2015; Nguyen and Kim, 2019; Ni et al., 2019; Rujikiatkamjorn and Indraratna, 2006; Rujikiatkamjorn et al., 2008). However, none of those models uses directly stress-dependent parameters obtained from the CRST. Instead, the MCC model and the SS model have been commonly chosen (Indraratna and Redana, 2000; Rujikiatkamjorn and Indraratna, 2006; Rujikiatkamjorn et al., 2008), in which key input parameters are the compression index, the recompression index and the hydraulic conductivity. The compression and the recompression indices for a specific material zone do not usually change during calculation processes, while the hydraulic conductivity can be a constant or approximately depend on the void ratio. Nevertheless, when a curve  $e$ -log( $\sigma'$ ) has an S-shape (Liu et al., 2013) or the compression index is not constant (Bo et al., 2017), using a single value of the compression index for the MCC and SS model is not sufficient to represent real behaviours of soft soils.

All the above discussions lead to an idea to develop FE models based on the poroelasticity theory with stress-dependent parameters obtained from the CRST for consolidation analyses of unit cells. Using FE models, the smear zone and the discharge capacity of PVDs can be considered. Furthermore, various boundary condition types can be applied. Because such an approach has not been implemented before, validations must be carried out. The most suitable validated scheme is to simulate the CRST itself, i.e. to compare modelled results to experimental data. If the method is capable of modelling the CRST (i.e. modelled results fit experimental data), it can also be employed for upscale models.

Here, an open-source FE software named CONAXIS (github.com/pham-hung/Conaxis) is introduced for the purposes explained above. CONAXIS was developed using C++ with the cross-platform framework Qt; hence, the source code can be compiled on both Windows and Linux. The program and the source code are freely provided on GitHub. More information related to the theory, verifications, examples and tutorials can also be found there. As the code is open-source, it is free to use, distribute and modify in accordance with the license.

Two soft soil improvement projects in Mekong Delta (Vietnam) were chosen as case studies of combining Biot's theory and stress-dependent parameters gained from the CRST using CONAXIS. Both projects used PVDs, surcharge loading and vacuum pumping as the ground improvement method. The methodology and the procedure for consolidation analysis are explained in detail for the first project; then, they are applied for the second project. All data is provided on GitHub.

In the first project, nine CRSTs with various depths from a borehole

were carried out. Two arbitrary tests among them were modelled with CONAXIS for validation purposes. Moreover, they were also simulated with PLAXIS using the SS model. Modelled results from CONAXIS and PLAXIS then were compared to laboratory data. While CONAXIS produced almost exactly total stress values, differences between PLAXIS results and measurements were considerable. In terms of the excess pore water pressure (EPWP), relative errors between results from both software and recorded data were also significant. Therefore, a back-analysis scheme was developed and implemented in CONAXIS to minimise those errors. For the unit cell model, back-analyses for all nine CRSTs were performed initially. The results were  $K$ - $\sigma'_{zz}$  and  $k_z$ - $\sigma'_{zz}$  curves, where  $K$  is the bulk modulus,  $k_z$  is the vertical hydraulic conductivity and  $\sigma'_{zz}$  is the vertical effective stress. Afterwards, these curves were directly used for the unit cell model.

For the second project, six CRSTs from three boreholes were utilised to set up the unit cell model in CONAXIS. As in the first project, the back-analysis procedure was also used for all tests to obtain stress-dependent parameters.

## 2. Theory and methodology

Brief information about the CRST, equations from ASTM-D4186 to interpret test data, the unit cell theory for consolidation analyses of PVD systems and the poroelasticity theory are mentioned here. In-depth descriptions are found in ASTM-D4186 (ASTM/D4186M-12e1, 2014), the summary of Chai (Chai and Carter, 2011), and works of Verruijt (2016).

### 2.1. Constant rate of strain tests

In the CRST (Fig. 1), the soil specimen is axially sandwiched between the porous stone on the top and the rigid plate on the bottom, and it is laterally constrained by O-rings. The load cell is connected to the motor so that the strain rate is constantly kept during the test. The deformation and the pore pressure taken place during the test are measured and recorded through the linear variable differential transformer (LVDT) and the pore pressure transducer, respectively.

The measured data includes values recorded by LVDT  $\Delta H$  (m), the vertical applied pressure  $\sigma$  (kPa) and the pore pressure  $p$  (kPa) from the pore pressure transducer. The initial data of a soil sample is the initial height  $H_0$  (m) and the initial void ratio  $e$ . According to ASTM-D4186, either the linear theory or the nonlinear theory can be used to interpret data from the CRST. Both theories assume the compressibility  $m_v$  ( $m^2/kN$ ) and the consolidation coefficient  $c_v$  ( $m^2/s$ ) are constant over the depth of the sample at any time.

At any given time  $t$ , in case of the linear theory, equations 23–27 in

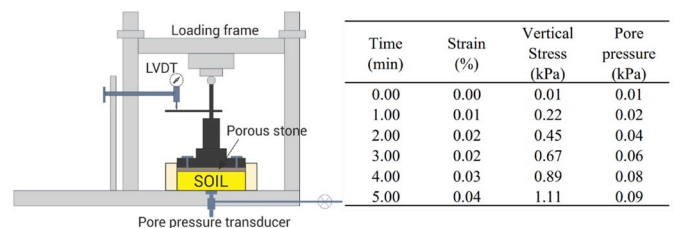


Fig. 1. The CRS test scheme and reading values.

**Table 1**  
Applications of the CRS test for consolidation analyses.

Authors	Analysis method	Soil improvement method	Location
Suzuki and Yasuhara (Suzuki and Yasuhara, 2004)	Finite difference	PVDs	Japan and Indonesia
Suzuki and Takeuchi (Suzuki and Takeuchi, 2008)	Finite difference	PVDs	Haiphong, Vietnam
Nguyen and Pham (Nguyen and Giao, 2014)	Analytical solution	PVDs and vacuum	Vungtau, Vietnam
Nguyen and Tran (Nguyen and Tran, 2015)	Finite difference	PVDs and vacuum	Camau, Vietnam

ASTM-D4186 (ASTM/D4186M-12e1, 2014) are used to calculate the average vertical effective stress  $\sigma'$  (kPa), the vertical hydraulic conductivity  $k_v$  (m/s), the compressibility  $m_v$  and the consolidation coefficient  $c_v$ . For the nonlinear theory, equations ( $\times 1.1$ -X1.4) are applied instead.

On the other hand, the compressibility  $m_v$  can be expressed as:

$$m_v = \frac{1}{K + 4G/3} = \frac{1 + \mu}{3K(1 - \mu)} \quad (1)$$

where  $K$  (kN/m<sup>2</sup>) is the bulk modulus,  $G$  (kN/m<sup>2</sup>) is the shear modulus and  $\mu$  is the Poisson's ratio. From equation (1), if Poisson's ratio is known, the bulk modulus and the shear modulus are obtained for each time; these parameters are considered to depend on the average vertical effective stress or the void ratio.

## 2.2. Unit cell models for consolidation analysis of PVD systems

PVDs are band-shaped and have channelled plastic cores wrapped with geotextile filters. Water from soft soils passes the geotextile filter and then flows along the channelled core to the free surface. Instead of vertical flow, water flow is radial, and the length of the drainage paths is shortened significantly. The consolidation rate is thus speeded up. PVDs are often installed in a triangular pattern or a square pattern with an appropriate distance using a special machine that has the mandrel to push PVDs into the soils. The mandrel can disturb the soils around PVDs and create the smear zone.

Each PVD has a specific influence zone that is idealised as a cylinder, which is called a unit cell. The radius of the unit cell  $r_e$  (m) is determined based on the field installation pattern, and the distance between PVDs. At the centre of the unit cell, dimensions of the PVD and the smear zone are converted into equivalent zones that have radii  $r_w$  (m) and  $r_s$  (m), respectively.

Consolidation analysis for a unit cell is performed with an axisymmetric model (Fig. 2). The horizontal and vertical displacements and the EPWP are denoted as  $u$ ,  $v$ , and  $p$ , respectively. The left and the right boundaries of the unit cell have  $u = 0$ ; the bottom boundary has  $v = 0$ . If the well resistance is ignored (i.e. the discharge capacity of PVDs is infinite), the PVD boundary has zero EPWP ( $p = 0$ ). In contrast, the flow along PVD is considered as the one-dimensional (1D) flow.

## 2.3. Axisymmetric finite element models based on the poroelasticity theory

The coordinate system of axisymmetric models is shown in Fig. 3. The equation system includes the storage and stress equilibrium equations. The storage equation is defined as:

$$\alpha \frac{\partial \varepsilon}{\partial t} + S_s \frac{\partial p}{\partial t} = \frac{\partial k_r}{\partial r} \frac{\partial p}{\partial r} + \frac{1}{r} \frac{k_r}{\gamma_f} \frac{\partial p}{\partial r} + \frac{\partial k_z}{\partial z} \frac{\partial p}{\partial z} \quad (2)$$

where  $\alpha$  is the Biot's coefficient (for soft soils  $\alpha = 1$ ),  $S_s = nC_f + (\alpha - n)C_s$  ( $\text{m}^2/\text{kN}$ ) is the storativity,  $n$  is the porosity,  $C_f$  ( $\text{m}^2/\text{kN}$ ) and  $C_s$  ( $\text{m}^2/\text{kN}$ )

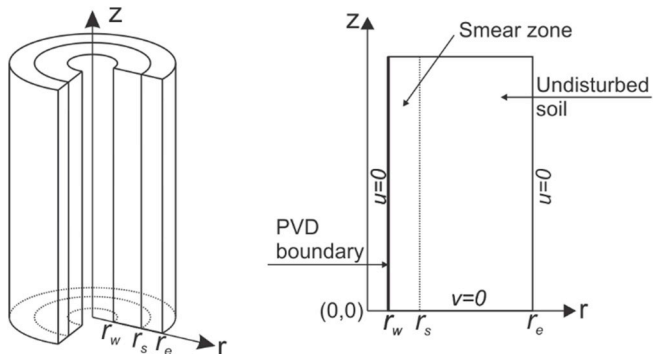


Fig. 2. Unit cell models.

are compressibilities of water and soil skeletons,  $k_r$  (m/s) and  $k_z$  (m/s) are the horizontal and vertical hydraulic conductivity, respectively, and  $\varepsilon$  is the total strain.

The stress equilibrium equations for  $r$ -direction and  $z$ -direction are:

$$\frac{\partial \sigma_{rr}}{\partial r} + \frac{\sigma_{rr} - \sigma_{\theta\theta}}{r} + \frac{\partial \sigma_{rz}}{\partial z} - f_r = 0 \quad (3)$$

$$\frac{\partial \sigma_{rz}}{\partial r} + \frac{\partial \sigma_{rz}}{r} + \frac{\partial \sigma_{zz}}{\partial z} - f_z = 0 \quad (4)$$

where  $\sigma_{rr}$ ,  $\sigma_{\theta\theta}$ ,  $\sigma_{rz}$  and  $\sigma_{zz}$  are the total stress components,  $f_r$  and  $f_z$  are the body force components. The total stress is calculated according to Hook's law and Terzaghi's principle of effective stress with Biot's correction.

$$\begin{aligned} \sigma_{rr} &= \sigma'_{rr} + \alpha p = -(K - 2G/3)\varepsilon - 2G(\partial u/\partial r) + \alpha p \\ \sigma_{zz} &= \sigma'_{zz} + \alpha p = -(K - 2G/3)\varepsilon - 2G(\partial v/\partial z) + \alpha p \\ \sigma_{\theta\theta} &= \sigma'_{\theta\theta} + \alpha p = -(K - 2G/3)\varepsilon - 2G(u/r) \\ \sigma_{rz} &= \sigma'_{rz} = -2G(\partial u/\partial z + \partial v/\partial r) \\ \varepsilon &= \varepsilon_{rr} + \varepsilon_{\theta\theta} + \varepsilon_{zz} = (\partial u/\partial r) + (u/r) + (\partial v/\partial z) \end{aligned} \quad (5)$$

where  $\varepsilon_{rr}$ ,  $\varepsilon_{zz}$  and  $\varepsilon_{\theta\theta}$  are the strain components;  $\sigma'_{rr}$ ,  $\sigma'_{zz}$  and  $\sigma'_{\theta\theta}$  are the effective stress.

Applying the Galerkin approximation method for equations (2)–(5) with the backward interpolation scheme, the coupled system is written under the matrix form:

$$\begin{Bmatrix} [K] & [L] \\ -[L]^T & [S] + \Delta t[M] \end{Bmatrix} \begin{Bmatrix} \Delta d \\ \Delta p \end{Bmatrix} = \begin{Bmatrix} \Delta F \\ -\Delta t[M] \times p_0 + \Delta t[Q] \end{Bmatrix} \quad (6)$$

where  $\{\Delta d\} = \{\Delta u \ \Delta v\}^T$  is the incremental displacement vector,  $\Delta p$  is the incremental pore pressure vector,  $p_0$  is the initial pore pressure vector,  $\Delta t$  is the time step,  $[K]$  is the matrix for the displacement field,  $[S]$  and  $[M]$  are matrices for transient field,  $[L]$  is the coupled matrix,  $\Delta F$  is the incremental load vector, and  $Q$  is the extract rate vector.

## 3. The CONAXIS software

CONAXIS (i.e. consolidation analysis of axisymmetric systems) is an open-source software developed using C++ with the cross-platform framework Qt (Pham et al., 2019a, 2019b). The source code can be compiled both on Windows and Linux. CONAXIS focuses on consolidation analyses for unit cell models using directly stress-dependent parameters obtained from the CRST. CONAXIS is freely provided on GitHub. For Windows users, CONAXIS can be used immediately without any configuration. For Linux users, the source code needs to be compiled again. Detailed information related to verifications, tutorials, program description and examples is also available on GitHub.

### 3.1. Modelling the CRST in CONAXIS

The purpose of re-simulating the CRST is to validate the proposed approach (i.e. using stress-dependent parameters obtained from the CRST for consolidation analyses) by comparing modelled results with laboratory data. If the simulated outputs fit laboratory values, the proposed approach can be applied to upscale models to solve practical problems.

Fig. 4a illustrates the FE mesh and the boundary conditions of a CRST model in CONAXIS. The model has the height  $H_0$  and the radius  $R$ . As the sample is laterally constrained by O-rings, the left and the right boundaries of the model have  $u = 0$  (no horizontal movement). The bottom is assigned the boundary condition  $v = 0$  (no vertical movement), and the top boundary is the drained boundary condition  $p = 0$  (no EPWP).

For each time step, a measured dataset of a CRST includes the applied pressure on the top of the sample (from the loading frame), the top vertical displacement (from LVDT) and the EPWP on the bottom

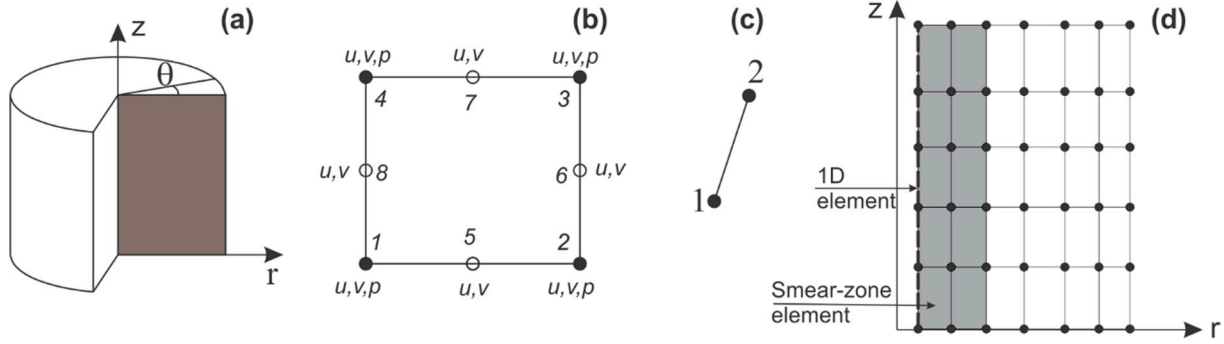


Fig. 3. (a) The axisymmetric coordinate system; (b) The rectangular element; (c) The 1D element; (d) The finite element mesh.

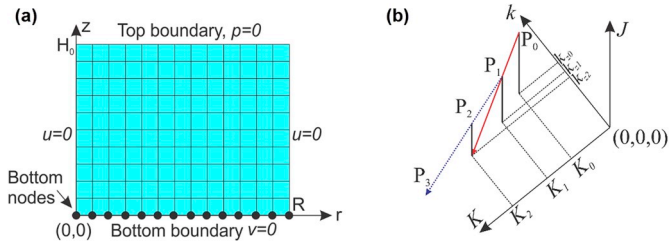


Fig. 4. (a)-A model of a CRS test; (b)-Secant method for the back-analysis process.

(from the pore pressure transducer). However, in the FE model, the top boundary can only be assigned a pressure (Neumann's boundary condition) or a displacement (Dirichlet's boundary condition). Therefore, there are two possibilities to evaluate differences between modelled results and measured data.

The first possibility is to assign pressure values from the loading frame converted to nodal forces to the top boundary. Modelled results are the average EPWP of bottom nodes and the average vertical displacement of top nodes; then, these values are compared to experimental data. It is called the load control procedure. The second is the strain control procedure, in which values from LVDT are used as the boundary condition for the top boundary instead of the applied pressure. The average total stress of all elements is determined and compared with values from the loading frame.

From a dataset of a CRST, CONAXIS first calculates the bulk modulus  $K$ , the shear modulus  $G$  and the vertical hydraulic conductivity  $k_z$  for each time step based on ASTM-D4186 using either the linear theory or the nonlinear theory. Because there is only the vertical seepage flow, the horizontal hydraulic conductivity  $k_r$  does not affect modelled results. Therefore,  $k_r$  is assumed to be equal to  $k_z$ . Furthermore, modelled time steps are taken from the test data (the first column in Fig. 1). Both the load control procedure and the strain control procedure are available in CONAXIS.

It is noted that at any given time step, the bulk modulus, the shear modulus and the hydraulic conductivity are identical for all elements of the model. In other words, the soil sample is considered as a representative elementary volume. This satisfies Wissa's assumptions (Wissa, 1971).

### 3.2. Back-analysis: a new approach to interpret data from the CRST

Assume that Poisson's ratio is known, at any given time step, the values of the bulk modulus and the vertical hydraulic conductivity are  $K_m$  and  $k_{z,m}$ , respectively. From the laboratory data, the applied stress and the EPWP are  $\sigma_n$  and  $p_n$ . With the strain control procedure, the average total vertical stress of all elements and the average EPWP of bottom nodes of an FE model are denoted as  $\sigma_{zz,m}$  and  $p_m$ .

Relative errors between recorded values and modelled results are

defined:

$$J_{pore} = \frac{(p_m - p_n)}{p_n} \quad (7)$$

$$J_{stress} = \frac{(\sigma_{zz,m} - \sigma_n)}{\sigma_n} \quad (8)$$

As previously mentioned in section 2.1, the bulk modulus  $K_m$  and the vertical hydraulic conductivity  $k_{z,m}$  can be obtained by using ASTM-D4186. When modelled results fit recorded values, the errors  $J_{stress}$  and  $J_{pore}$  are expected to be small.

If  $J_{stress}$  and  $J_{pore}$  of each time step are minimised by modifying the input parameters  $K_m$  and  $k_{z,m}$ , an optimisation problem with a constraint condition occurs:

$$\begin{cases} |J_{pore}| \leq \epsilon; & |J_{stress}| \leq \epsilon \\ k_{z,m} > 0; & K_m > 0 \end{cases} \quad (9)$$

where  $\epsilon$  is a defined tolerance.

Solving equation (9) is a back-analysis process with objective functions  $J_{pore}$  and  $J_{stress}$ . The back-analysis is an iterative process, which was described by Shoji (Shoji et al., 1990). The process starts with initial values of model parameters; they are then modified after each iteration until convergence criteria are reached.

Several methods can be used to solve the back-analysis problem such as the conjugate gradient method (Arai et al., 1987) and the Broyden-Fletcher-Goldfarb-Shanno (BFGS) formula (Shoji et al., 1990). However, both methods require calculating derivatives of the objective functions of  $K_m$  and  $k_{z,m}$  to determine the search direction. This leads to computing two derivatives of the global matrix stiffness of  $K_m$  and  $k_{z,m}$  that is complicated. Therefore, CONAXIS uses the secant method instead (Fig. 4-b). Starting with the first row of a recorded dataset, the detailed steps are:

- **Step 1:** Calculate values of the objective functions  $J_{pore}$  and  $J_{stress}$  with initial values  $k_{z0}$  and  $K_0$ . Choose  $J_{pore}$  or  $J_{stress}$  to minimise first. It is the point  $P_0 (k_{z0}, K_0, J_0)$  in Fig. 4-b.
- **Step 2:** Modify  $k_{z0}$ ,  $K_0$  to find the point  $P_1$ .
- **Step 3:** Find an intersection between the line  $P_0P_1$  and the plane  $k_zOK$ . The intersection point is  $P_2 (k_{z2}, K_2, J_2)$ . Recalculate the objective function with  $k_{z2}$ ,  $K_2$  get to  $J_2$ .
- **Step 4:** Repeat Step 1 to Step 3 until  $|J_i| \leq \epsilon$  and move to the next objective function.
- **Step 5:** When both  $J_{pore}$  and  $J_{stress}$  are smaller than  $\epsilon$ , move to the next row.

An intersection point between a line and a plane is easy to find, and no derivative is needed. After the back-analysis process, for each time step, the average vertical effective stress of all elements  $\sigma'_{zz}$  is calculated. The bulk modulus  $K$  and the hydraulic conductivity  $k_z$  depend on  $\sigma'_{zz}$ .

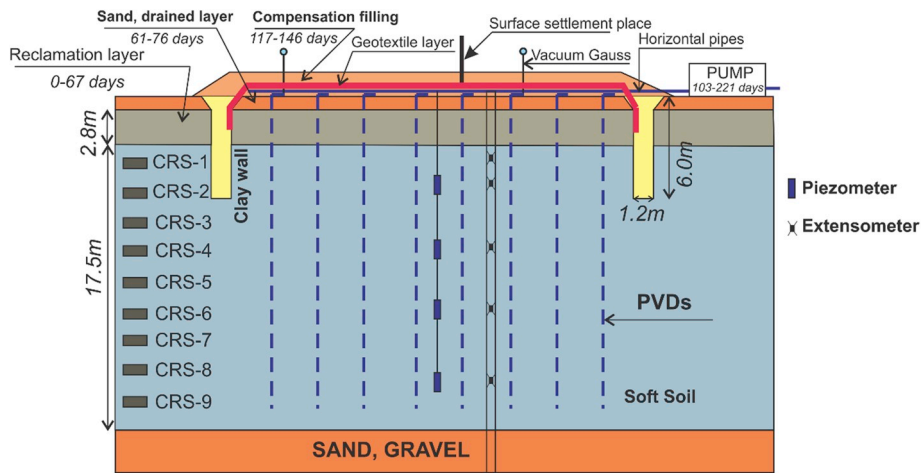


Fig. 5. CMGPP project scheme.

4. First case study: camau gas processing plant (CMGPP)

4.1. Project description

The CMGPP located in Camau Vietnam was built on a large area (~330 m × 113 m) that had 17.5 m thickness of soft soils. To reduce the post-construction settlement and to reduce the construction time, PVDs combined with surcharge loading and vacuum pumping were used to accelerate the consolidation process. The PVDs grid was 1.0 m by 1.0 m square. The 100 mm × 4 mm PVDs RID 4.0 were installed with a rectangular 120 mm × 60 mm mandrel.

The construction process is shown in Fig. 5. Initially, a 2.8 m reclamation layer was filled using the hydraulic method. A 0.5 m sand layer was added subsequently, followed by the installation of the PVDs. A clay diaphragm wall system that had 6.0 m height and 1.2 m thickness was constructed to decouple the treated zone hydraulically. Next, the PVDs were connected to a vacuum discharge system. A geo-membrane layer and PE-HD liners covered all the treated area. Then, vacuum pumps generated vacuum pressure within 118 days. During this period, a compensation-filling layer was also added.

The instrument system (Fig. 6) was placed after installing PVDs. It included ten surface settlement plates (SSP21–30), three multipoint extensometers (SS7, SS8, SS9), eight vacuum gauges (VG18–26), and three piezometer groups (PZ7, PZ8, PZ9). Each extensometer had nine sensors, and each piezometer group had four piezometers at various depths.

4.2. Testing data

The piston sampler with the thin-wall tube was used to retrieve high-quality samples for the CRSTs. Nine CRSTs from various depths of

Table 2

CMGPP project - Summary of soil laboratory testing results.

No.	Depth (m)	Liquid limit %	Plastic limit %	Plasticity index	Wet density (kN/m <sup>3</sup> )	Void ratio
CRS-1	3.5–4.5	47.8	28.3	19.5	16.4	1.42
CRS-2	5.5–6.5	57.0	29.2	27.8	16.3	1.65
CRS-3	7.5–8.5	57.6	34.0	23.5	16.4	1.60
CRS-4	9.5–10.5	84.3	37.6	46.8	15.2	1.84
CRS-5	11.5–12.5	73.0	34.5	38.5	15.7	1.81
CRS-6	13.5–14.5	73.7	35.5	38.2	15.9	1.82
CRS-7	15.5–16.5	86.2	40.2	46.0	15.4	2.07
CRS-8	17.5–18.5	79.2	37.0	42.2	15.7	1.89
CRS-9	19.5–20.5	81.3	36.5	44.7	15.7	1.88

the same borehole (Fig. 6) were performed under 0.0051 mm/min displacement rate. The depth was calculated from the surface elevation of + 3.3 m. The soil properties of nine samples are given in Table 2. All samples had the initial height  $H_0 = 2.54$  cm and the radius  $R = 3.175$  cm (the cross-section area was 31.67 cm<sup>2</sup>).

Fig. 7 presents laboratory data of nine CRSTs. The EPWP values of the CRS-1 and CRS-2 were approximately zero because of high permeability. Those two samples might come from a sandy clay layer.

4.3. Modelling the CRST: comparisons between CONAXIS and PLAXIS

CONAXIS can be used to model the CRST with parameters obtained using either the linear theory or the nonlinear theory (ASTM/D4186M-12e1, 2014). CRS-3 and CRS-7 were chosen randomly to be simulated by CONAXIS and PLAXIS version 8.2 (Fig. 8) for the validation and comparison purposes. While CONAXIS utilised the poroelasticity theory

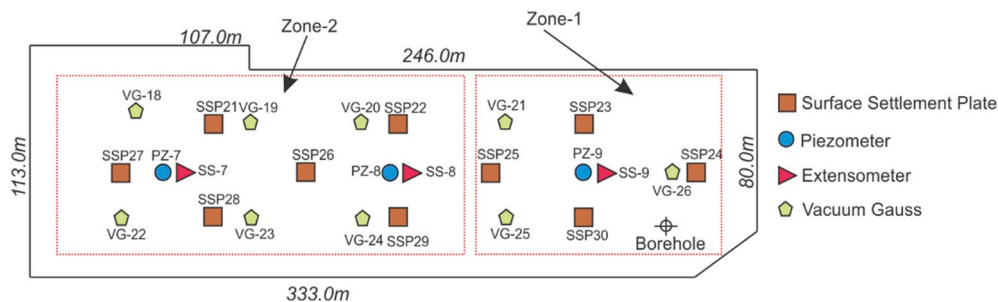


Fig. 6. CMGPP project - Monitoring system.

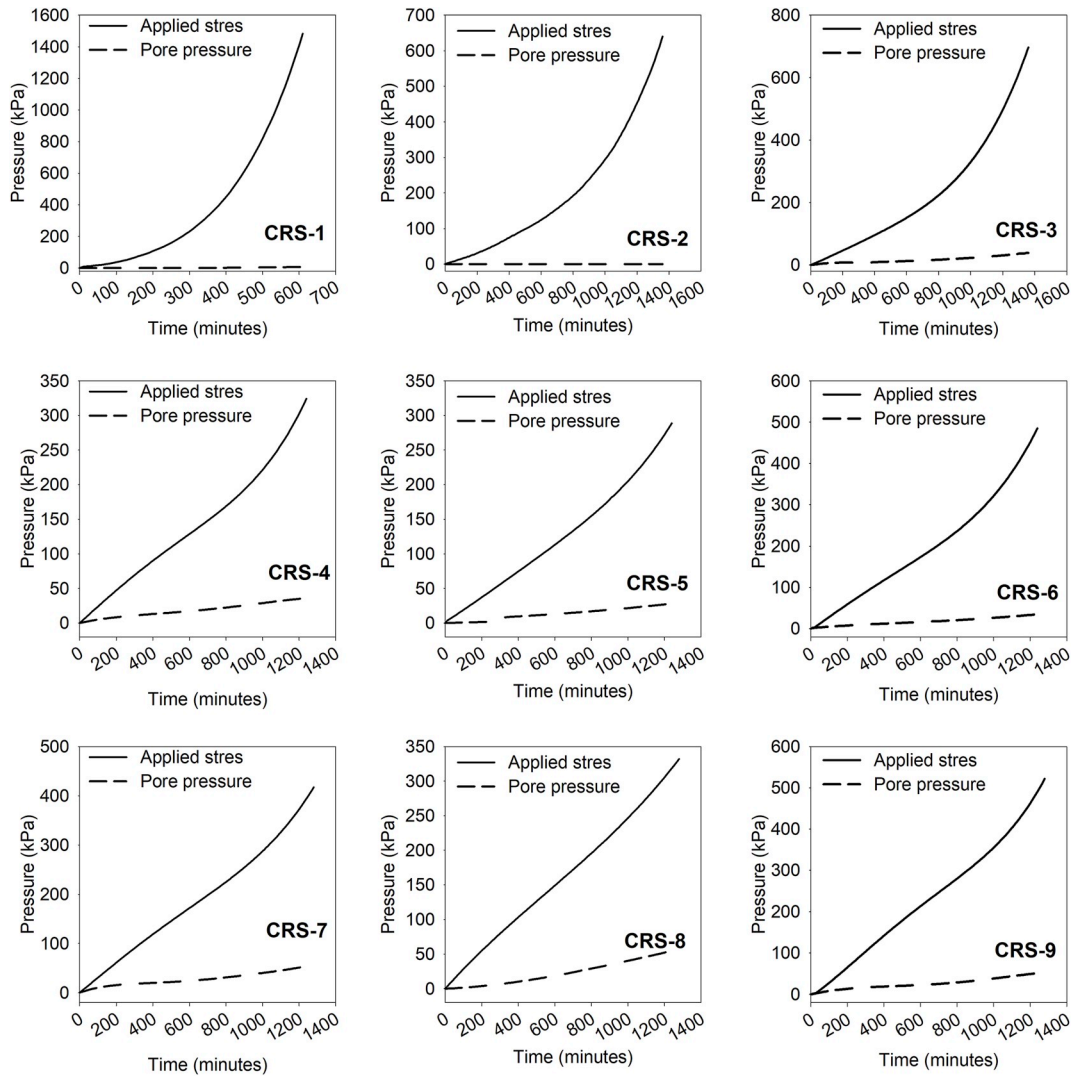


Fig. 7. CMGPP project - Testing data of the nine samples with 0.0051 mm/min constant strain rate.

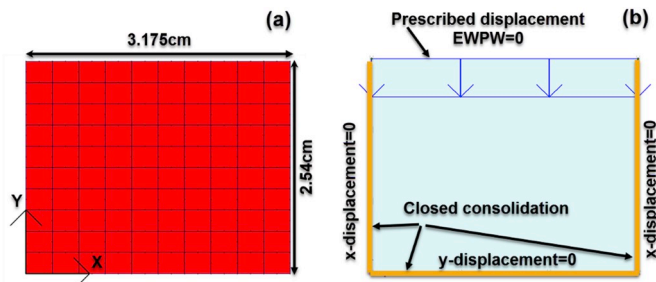


Fig. 8. (a) CONAXIS model; (b) PLAXIS model.

with stress-dependent parameters, the SS model of PLAXIS was used. Input parameters for the SS model in PLAXIS were obtained (Table 3) by plotting the experimental data as Fig. 9.

**Table 3**  
Input parameters for the soft soil model in PLAXIS.

Sample No.	$C_c$	$C_r$	$K_0$	$\mu$	$M$	$p'_c$ (kPa)	POP (kPa)	$e_0$	$k_0$ (m/s)	$C_k$
CRS-3	0.597	0.045	0.5	0.2	1.61	65.0	65.0	1.60	2.10e-9	0.699
CRS-7	0.869	0.082	0.5	0.2	1.61	80.1	80.1	2.07	9.15e-10	0.921

In Table 3,  $C_c$  and  $C_r$  are the compression and recompression indices.  $K_0 = 1 - \sin(\phi')$  is the at-rest earth pressure coefficient, where  $\phi'$  is the effective friction angle. The Poisson's ratio  $\mu$  is determined empirically. For the soft soil model, the slope of critical state line  $M$  is automatically calculated from  $K_0$ . POP is the pre-overburden pressure used to generate the initial stress state. POP is defined as the difference between the preconsolidation stress  $p'_c$  and the initial vertical stress. Because samples were totally unloaded, POP is equal to  $p'_c$ . The parameter  $e_0$  is the initial void ratio,  $k_0$  is the vertical hydraulic conductivity corresponding to the void ratio  $e_0$ .  $C_k$  quantifies the relation between the void ratio and the hydraulic conductivity (Equation (10)). In Fig. 9, the recompression paths of  $e \sim \log(k_v)$  curves were ignored to determine  $C_k$ ,  $k_0$  was thus taken by extending the compression paths.

$$C_k = \frac{e - e_0}{\log(k/k_0)} \quad (10)$$

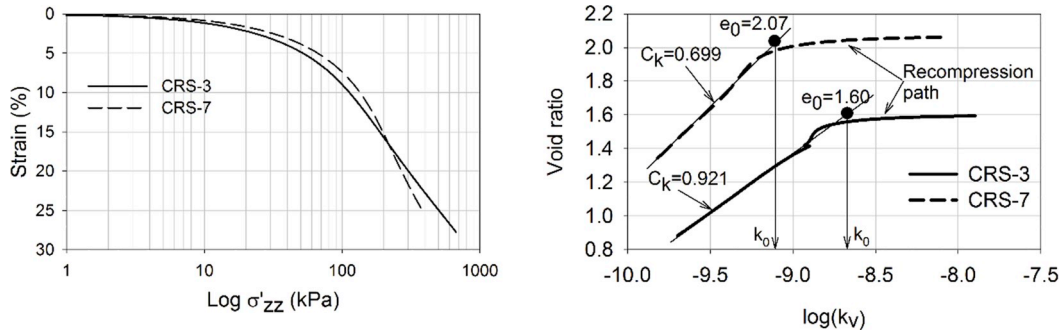


Fig. 9. Testing data of CRS-3 and CRS-7.

The strain control procedure was used for both CONAXIS and PLAXIS. Fig. 10a–d compare direct results of the total stress and the EPWP from two software to laboratory data, and Fig. 10e and f shows relative errors  $\epsilon$  which are calculated as:

$$\epsilon = 100 \left| \frac{i_m - i_r}{i_r} \right| \% \quad (11)$$

where  $i_m$  is the modelled result and  $i_r$  is the recorded value.

In terms of the total stress, the differences between CONAXIS and recorded data of both tests were small with less than 3% relative errors. Meanwhile, errors of PLAXIS were more significant at the beginning of the tests and then decreased over time. At the end of the loading phase, those errors were about 20%. Concerning the EPWP, CONAXIS generated up to 35% higher values compared to test data. Because of ignoring the recompression paths to determine  $C_k$  and  $k_0$  values, PLAXIS failed to give consistent results of the EPWP during the recompression phase (i.e.  $\sigma' < p'_c$ ) that also resulted in large errors of the total stress. Within the normally consolidated range, results of PLAXIS were closer to recorded data; however, similarly to CONAXIS, relative errors of the EPWP were still quite significant (up to 40%).

were calculated according to ASTM-D4186. Even if only the normally consolidated range was considered, relative errors of the EPWP between both software and measured data were still considerable. Hence, it is suggested that the back-analysis scheme should be used to minimise those errors. Moreover, differences between PLAXIS results and measurements can derive from the fact that a single set of  $C_c$  and  $C_r$  is not sufficient to describe a stress-strain curve gained from a CRST. To reduce errors,  $\epsilon$ - $\log(\sigma')$  and  $e \sim \log(k_v)$  curves can be divided into smaller segments. For example, in the studies of Suzuki (Suzuki and Takeuchi, 2008; Suzuki and Yasuhara, 2004) and Nguyen (Nguyen and Tran, 2015), two or three  $C_c$  values (namely  $C_{c1}$ ,  $C_{c2}$ , and  $C_{c3}$ ) were used. This approach can be applied in PLAXIS to model the CRST with the SS model by using more calculation phases. Each phase has different input parameters corresponding to a range of the average effective stress. However, to model a real field problem, this method is not practical since each element of a model has a different effective stress value at a specific calculation time.

4.4. Back-analysis results

To gain a perfect fit between CONAXIS and measured data, the

The hydraulic conductivity values for both CONAXIS and PLAXIS

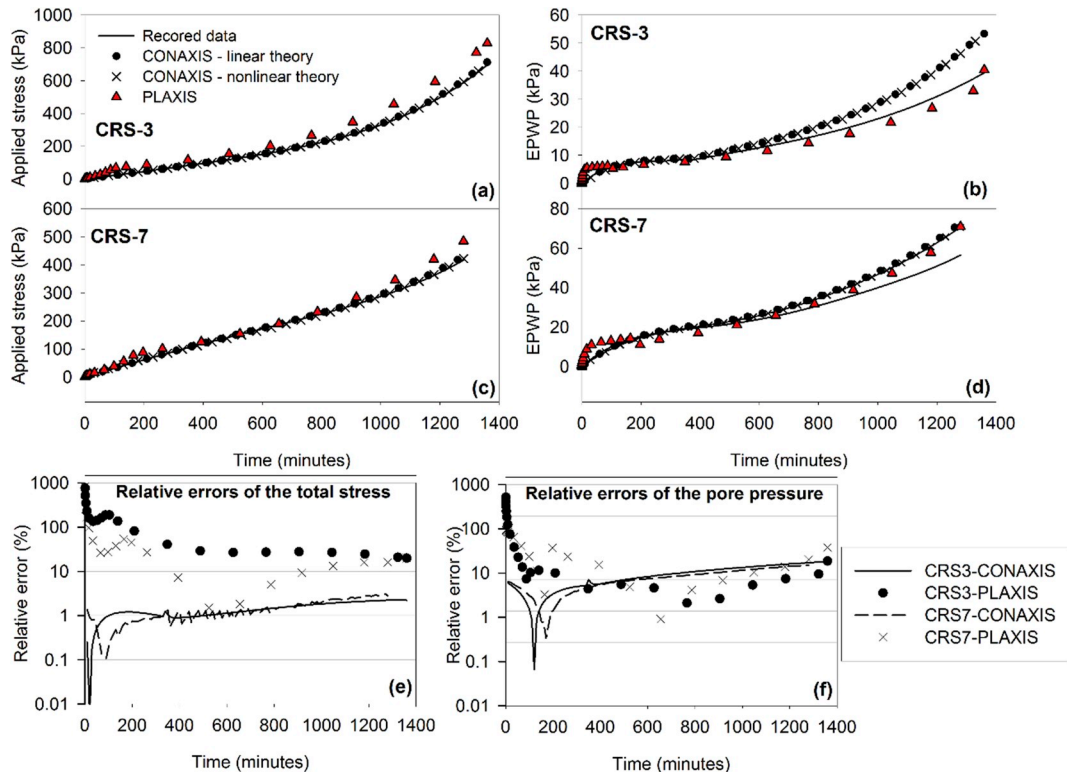


Fig. 10. Comparisons among CONAXIS, PLAXIS and measured data.

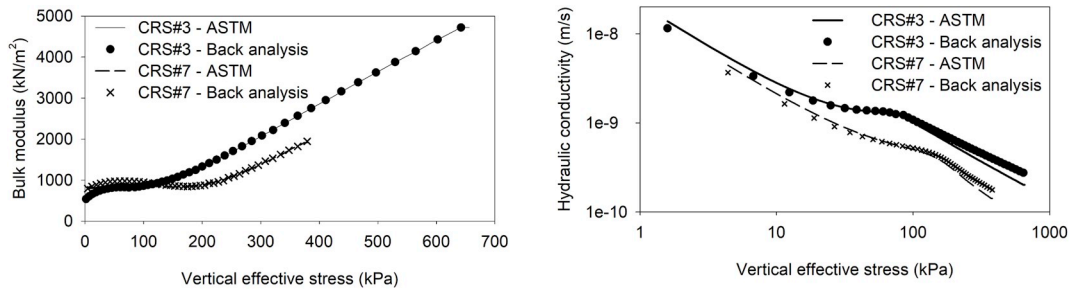


Fig. 11. Comparing parameters obtained using the back-analysis method and ASTM-D4186.

back-analysis scheme described in section 3.2 was utilised. The tolerance  $\epsilon$  (in equation (9)) for the back-analysis process was set to 0.001, or there was nearly no difference between modelled results and measurements. Fig. 11 compares the bulk modulus and the vertical hydraulic conductivity obtained with the back-analysis method with values obtained using ASTM-D4186. The bulk modulus curves from the two methods are similar. It is reasonable as the differences in the total stress between CONAXIS and laboratory data are minor (Fig. 10). Conversely, CONAXIS alters slightly values of the hydraulic conductivity to match numerical results with test data.

4.5. Axisymmetric FE model of the unit cell

Because nine CRSTs were performed, the axisymmetric model of the unit cell was also divided into nine layers (Fig. 12a). The first layer has 1.5 m thickness, and the other layers have 2.0 m thickness. The back-analysis procedures were carried out for all nine tests. Poisson's ratio was assumed to be 0.4. As the unit cell model is laterally constrained, Poisson's ratio does not affect results. However, when the horizontal strain is considered in some cases, e.g. circular foundations, Poisson's ratio should be carefully considered.

For the square installation pattern of the PVDs with 1.0 m spacing, the radius of the unit cell is  $r_e = 0.565$  m. The equivalent radius of the PVDs, which have the width  $b$  and the thickness  $t$ , is (Long and Covo, 1994):

$$r_w = \frac{0.5b + 0.7t}{2} = \frac{0.5 \times 0.1 + 0.7 \times 0.004}{2} = 0.0264 \text{ m} \quad (12)$$

The smear zone is twice the size of the mandrel (Bergado et al., 1991). Hence, the equivalent radius  $r_s$  of the smear zone is (Bergado et al., 1991):

$$r_s = 2 \times \frac{0.5b + 0.7t}{2} = 2 \times \frac{0.5 \times 0.12 + 0.7 \times 0.06}{2} = 0.102 \text{ m} \quad (13)$$

There were four analysis stages corresponding to the construction process (Table 4). For all stages, the left and the right boundaries had no horizontal movement; the bottom had no vertical movement. In the in-situ stage, CONAXIS turned off the EPWP degree of freedom; only the

gravity force was applied to obtain the initial effective stress for all elements. After this stage, the displacements of all nodes were reset to zero.

The undrained analysis stage generated the initial EPWP. For stage 2, 3 and 4, loads of filled layers (sand layer, reclamation layer and compensation filling layer) were considered as the surcharge loading on the top boundary that changed during the construction time. The bottom boundary was assigned the drained boundary condition (i.e. EPWP is zero). The top and the PVD boundary was assigned the vacuum boundary condition with negative EPWP values that depended on the calculation time. Values of surcharge loading and vacuum pressures over time are plotted in Fig. 12b.

In this project, there was no opportunity for a laboratory test to evaluate the ratio between the horizontal hydraulic conductivity to the vertical hydraulic conductivity ( $r = k_r/k_z$ ). Hence, four analyses were performed with  $r = 1.0$ ,  $r = 2.0$ ,  $r = 3.0$  and  $r = 4.0$ , respectively. When the smear zone was considered, the horizontal conductivity of the smear zone was equal to the vertical hydraulic conductivity of the undisturbed zone (Bergado et al., 1991).

4.6. Comparisons between modelled results and field data

For easier visualisation, the treatment area is divided into Zone-1 and Zone-2 (Fig. 6). Each zone has similar monitoring data of surface settlement plates and multipoint extensometers; hence, results that are presented here are the average results of each zone. We denote SSP-Zone-1, SSP-Zone-2, SS-Zone-1 and SS-Zone-2 as average surface settlement values and average extensometer values of Zone-1 and Zone-2, respectively.

Fig. 13 compares surface settlement results of CONAXIS to field monitoring data of Zone-1 and Zone-2 with different ratios  $r$  with or without the smear zone. If there is no smear zone, the higher the ratio  $r$ , the higher the consolidation rate. For the cases  $r = 2.0$  and  $r = 3.0$ , modelled results are much different to field measurements. Since the smear zone cannot be avoided when installing PVDs, ignoring it leads to overestimating the settlement rate of the treatment area.

In contrast, when the smear zone is considered in models, and the

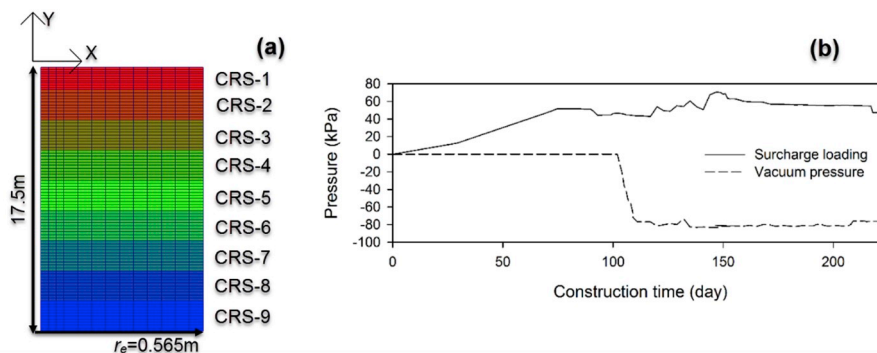


Fig. 12. CMGPP project - (a) Unit cell model in CONAXIS, each colour represents a material zone; (b) The surcharge loading and vacuum pressure over time.

**Table 4**  
CMGPP project - Analysis stages.

Stage #	Description	Start (day)	End (day)	Duration (day)	Number of steps
1	In-situ	0	0	0	1
2	Undrained (Initial step)	0	0	0	1
3	Before installing PVDs	0	85	85	170
4	After installing PVDs	85	221	136	272

ratio  $r$  is greater than 2.0, CONAXIS produced a good match with the monitoring data in terms of both the consolidation rate and the settlement values, especially for Zone-1. Within the smear zone, the horizontal hydraulic conductivity reduced to the vertical hydraulic conductivity. Consequently, for all cases, the hydraulic conductivity of the smear zone is identical. The smear zone acts as a barrier that constraints seepage flow. Although the horizontal hydraulic conductivity of the undisturbed zone is two to four times higher than the vertical hydraulic conductivity, the consolidation rates of these cases are not much different. For the clay from Mekong Delta, the ratio  $r$  from 2.0 to 3.0 is reasonable; they were also used for some previous studies (Nguyen and Tran, 2015).

Test samples were taken from the borehole that belonged to Zone-1 (Fig. 6). Hence, modelled results are much closer to field measurements of this zone. For Zone-2, simulated values are smaller than monitoring data. This discrepancy can derive from the layer-1 and layer-2 of the model. The samples for these layers (CRS-1 and CRS-2) might be from a sandy clay layer that does not appear in Zone-2. To verify this assumption, a new model (named model-2) with properties of layer-1 and layer-2 that were replaced by properties of layer-3 was performed (i.e. using CRS-3 for layer-1 and layer-2 instead of CRS-1 and CRS-2). The ratio  $r$  was set to 3.0. With this modification, the results of model-2 are closer to SSP-Zone-2 values (Fig. 14). Indeed, for a large treated area (approximately 38000 m<sup>2</sup>) with only one borehole data, it is impossible to have a perfect fit between numerical results and field measurements.

Fig. 15 compares simulated results and field data of extensometers for Zone-1 and Zone-2. Although there were still differences between the model and the reality, overall, CONAXIS produces acceptable results.

Unfortunately, results of piezometers are not shown here due to lack of data. However, the results of surface settlement plates and extensometers prove that the proposed approach implemented in CONAXIS is capable of solving practical problems.

**5. Second case study: saigon-hiep phuoc terminal port (SHTP)**

**5.1. Project description**

The SHTP locates in Ho Chi Minh City Vietnam, and the soil improvement area was approximately 11 ha. The similar treatment

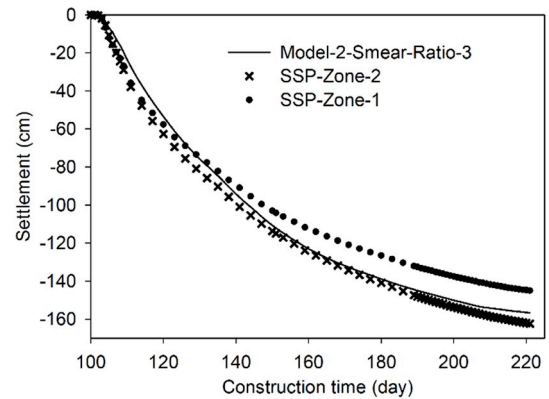


**Fig. 14.** CMGPP project - Surface settlement plates: Comparisons among Model-2 results, SSP-Zone-1 data and SSP-Zone-2 data.

method applied for the CMGPP project, which was the combination of PVDs, vacuum and surcharge loading, also was used in this project. Compared to the CMGPP project, the average thickness of soft soil in this project was double (35.0 m); hence, the construction time was also significantly longer (510 days) with the 304-day vacuum pumping period. Also, the total thickness of the reclamation layer and the sand layer below PE-HD liners was only 1.4 m. The other components such as the clay wall system, PVDs (the size, the type, and the distance among PVDs), the mandrel to install PVDs, the CRT apparatus, and the construction sequence were almost similar to those of the CMGPP project (Fig. 5).

The treatment area was divided into 12 sub-areas (so-called B1–B6 and A1–A6) and six phases (A1\_B1 to A6\_B6) as in Fig. 16a. In this study, data from the A5 area was selected. The monitoring system of the A5 region (Fig. 16a) included five surface settlement plates (SSP21–SSP25), and one extensometer E05. In addition, in Fig. 16b, the tip resistance ( $q_t$ ) profile from the piezocone penetration test (CPTu) shows that there are two sandy clay layers that must be considered in the analysis.

**5.2. Testing data**

Ten CRSTs were performed for samples that were taken from three

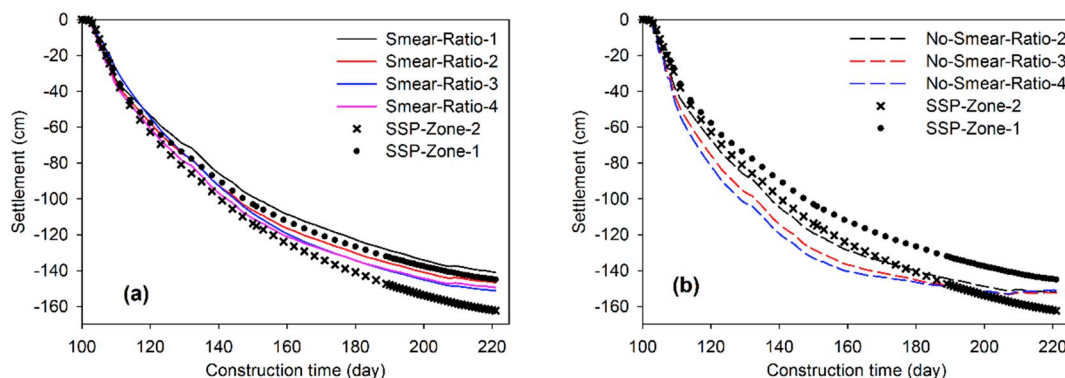


**Fig. 13.** CMGPP project - Surface settlement plates: Comparisons between CONAXIS results and field data.

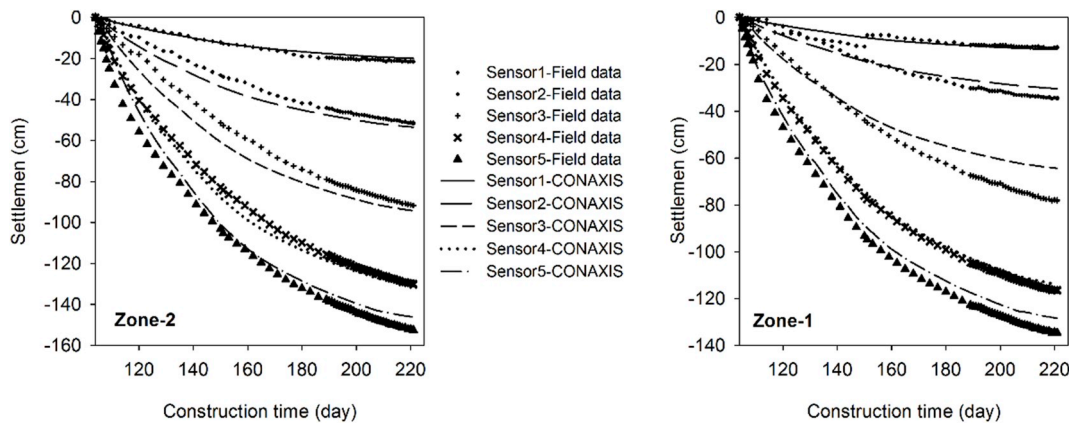


Fig. 15. CMGPP project - Multi-point extensometers: Comparisons between CONAXIS results and field data.

different boreholes in A4, A5, and A6 areas (Fig. 16a). However, some samples had a similar depth; therefore, only six CRSTs were selected for the consolidation analysis with one sample (CRS-A5-12) from the sandy clay layer. Table 5 summaries soil properties of six tests and Fig. 17 presents their testing data.

5.3. The unit cell model

The unit cell model was divided into seven layers corresponding to six CRSTs (Fig. 18a). The CRS-A5-12 test (sandy clay soil) was used for 4th and 6th layers. Back-analysis was performed for all tests in CONAXIS to obtain stress-dependent parameters.

As both CMGPP and SHTP projects are located in Mekong Delta Vietnam and have the similar characteristics of the PVD type, the distance among PVDs, and the mandrel size, the unit cell model for the SHTP project also has the radius  $r_e = 0.565$  m, the equivalent radius of the PVDs  $r_w = 0.0264$  m, the equivalent radius of the smear zone  $r_s = 0.102$  m, and the ratio  $r = 3.0$  (taken from section 4.5).

Five analysis stages corresponding to different construction phases are listed in Table 6. The surcharge loading profile calculated from heights of the sand layer, the reclamation layer, and the compensation filling layer is presented in Fig. 18b. The design vacuum pressure was  $-70$  kPa. Because of the considerable PVD length and the long vacuum pumping period, the well resistance effect is considered during the consolidation process by modelling the PVD with 1D elements (Fig. 18a) that have the section area  $A_{1D}$  ( $m^2$ ) and the hydraulic conductivity  $k_{1D}$  (m/s). With the discharge capacity  $q_w = 2000$   $m^3/year$ , properties of 1D elements are:

$$A_{1D} = \pi r_w^2 = 0.00219 \text{ m}^2 \tag{14}$$

$$k_{1D} = \frac{q_w}{A_{1D}} = 0.029 \text{ m/s} \tag{15}$$

Table 5

SHTP project - Summary of soil laboratory testing results.

No.	Depth (m)	Liquid limit %	Plastic limit %	Plasticity index	Wet density ( $kN/m^3$ )	Void ratio
CRS-A4-02	7.1	92.8	37.2	55.6	15.0	2.50
CRS-A5-04	11.0	74.6	41.2	33.4	15.3	2.45
CRS-A4-06	15.2	90.2	37.9	52.3	15.5	2.00
CRS-A4-10	23.2	64.4	29.7	34.7	16.1	1.90
CRS-A5-12	27.0	31.7	21.2	10.5	18.0	1.54
CRS-A6-12	31.0	80.1	37.8	42.2	16.5	1.72

Boundary conditions for each calculation stage are similar to those of the CMGPP project except the PVD boundary. As 1D elements are used to represent the PVD, no boundary condition is necessary for nodes along the PVD.

5.4. Comparisons between simulations and field data

Fig. 19 shows good agreements between CONAXIS results and monitoring data of the surface settlement plates (average values of five SSPs) and the extensometer. Due to a technical problem, field data of EX05 is only available from 207th day (start vacuum pumping) to 304th day.

6. Discussion and conclusion

This study proposes a new approach, which has not been applied before, to use laboratory data of the CRST for consolidation analysis with finite element models of unit cells based on Biot's theory. Instead of using compression and recompression indices to represent a stress-strain curve of a CRST,  $K-\sigma_v'$  and  $k_v-\sigma_v'$  curves are obtained from the

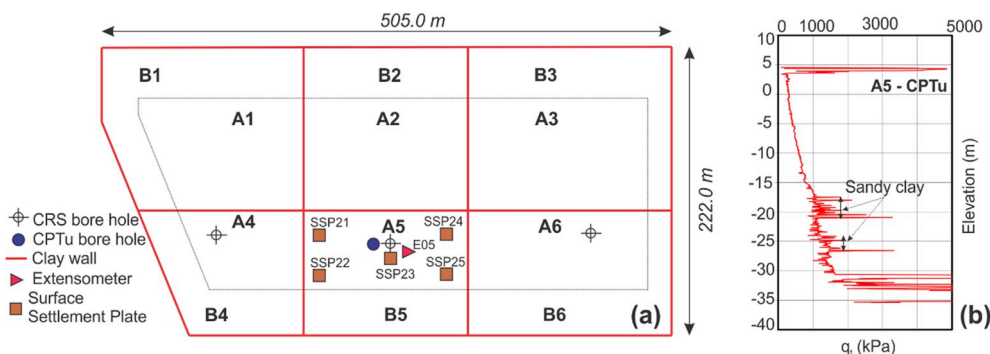


Fig. 16. SHTP project - (a) Project layout and the monitoring system of A5 area; (b) The tip resistance ( $q_t$ ) profile from the CPTu.

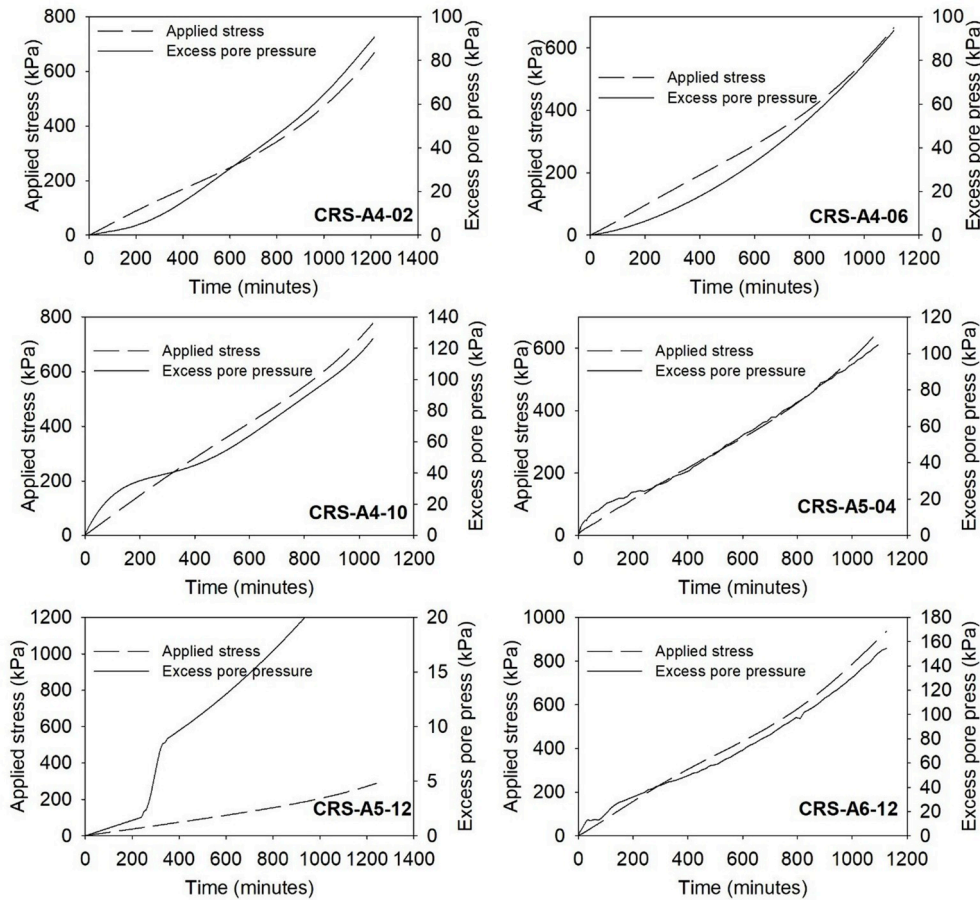


Fig. 17. Six CRSTs from three different boreholes of A4, A5, and A6 area.

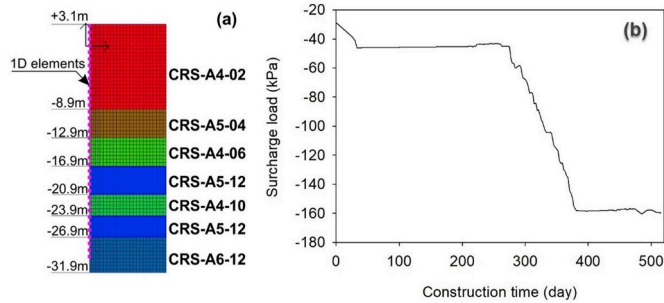


Fig. 18. SHTP project – (a) The unit cell model based on six CRSTs, the PVD is modelled with 1D elements, and the PVD length is 34.0 m; (b) The surcharge load during the construction time.

Table 6  
SHTP project - Analysis stages.

Stage #	Description	Start (day)	End (day)	Duration (day)	Number of steps
1	In-situ	0	0	0	1
2	Undrained (Initial step)	0	0	0	1
3	Reclamation	0	191	191	191
4	Installing PVDs	192	206	15	206
5	Vacuum pumping	207	511	304	304

continuous test data by following ASTM-D4186 or using the back-analysis scheme; then these curves are used directly for upscale models. The proposed method was validated by re-simulating the CRST.

Comparisons shown in section 4.3 suggest that although curves obtained by using ASTM-D4186 can be applied with acceptance accuracy, the back-analysis scheme should be used to achieve the best possible results. By following this approach, the CRST can be simulated exactly with almost no difference between modelled results and test data. Also, results from two case studies demonstrate that the proposed method is capable of solving practical problems.

Comparing to the SS model in PLAXIS, the proposed method generates more accurate results. Additionally, following this approach, no graphical method is needed to determine input parameters. Instead,  $K-\sigma_v'$  and  $k_v-\sigma_v'$  curves are obtained directly and automatically from test data.

The proposed method and the back-analysis scheme are implemented in CONAXIS, which is open-source and is distributed freely on GitHub. The software is simple, powerful, and ready for Windows end-users. For Linux users, the software needs to be compiled again. Because it is open-source, the software is completely free to use, to modify, and to redistribute. CONAXIS focuses on modelling unit cells with stress-dependent parameters obtained from the CRST. Most tasks of this study were done by using CONAXIS. However, CONAXIS does not aim to include the SS model or MCC model that are available in other software. Furthermore, it does not support plane-strain models.

The methodology presented in this study and CONAXIS software can also be extended to manage data from Rowe Cell. Moreover, back-analysis results from CONAXIS can be used for other software that has Biot's theory. For example,  $C_k$  and  $k_0$  values for PLAXIS (Table 3) can be altered after back-analysis processes to have better results. ANSYS or Sigma/W can utilise directly  $K-\sigma_v'$  and  $k_v-\sigma_v'$  curves for consolidation analyses.

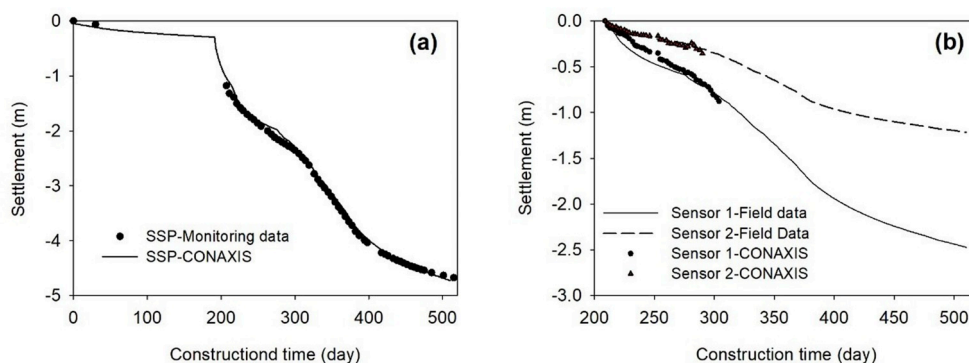


Fig. 19. SHPT project - Comparisons between CONAXIS results and field monitoring data - (a) Surface settlement plate; (b) Extensometer.

## Appendix

All the information related to CONAXIS and data can be found on GitHub: <https://github.com/pham-hung/Conaxis>.

## References

- Arai, K., Ohta, H., Kojima, K., 1987. Estimation of Non Linear Constitutive Parameters Based on Monitored Movement of Subsoil under Consolidation. Japanese Geotechnical Society, Tokyo, JAPON.
- ASTM/D4186M-12e1, 2014. Standard Test Method for One-Dimensional Consolidation Properties of Saturated Cohesive Soils Using Controlled-Strain Loading. ASTM International, West Conshohocken, PA 2012.
- Bergado, D.T., Asakami, H., Alfaro, M.C., Balasubramaniam, A., 1991. Smear effects of vertical drains on soft Bangkok clay. *Journal of Geotechnical Engineering* 117, 1509–1530.
- Biot, M.A., 1941. General theory of three-dimensional consolidation. *J. Appl. Phys.* 12, 155–164.
- Biot, M.A., 1955. Theory of elasticity and consolidation for a porous anisotropic solid. *J. Appl. Phys.* 26, 182–185.
- Bo, M.W., Choa, V., Chu, J., Arulrajah, A., Horpibulsuk, S., 2017. Laboratory investigation on the compressibility of Singapore marine clays. *Mar. Georesour. Geotechnol.* 35, 847–856.
- Chai, J., Carter, J.P., 2011. *Deformation Analysis in Soft Ground Improvement*. Springer, Dordrecht.
- Fantaziu, C.-M., Musat, V., 2014. Research on soil consolidation using consolidation cell under constant rate of strain. *Buletinul Institutului Politehnic din Iasi. Sectia Constructii, Arhitectura* 60 75.
- Haga, J.B., Osnes, H., Langtangen, H.P., 2012. On the causes of pressure oscillations in low-permeable and low-compressible porous media. *Int. J. Numer. Anal. Methods Geomech.* 36, 1507–1522.
- Hiep, H., Chung, S.G., 2018. Back-analysis of geotechnical parameters on PVD-improved ground in the Mekong Delta. *Geotext. Geomembranes* 46, 402–413.
- Indraratna, B., Redana, I.W., 2000. Numerical modeling of vertical drains with smear and well resistance installed in soft clay. *Can. Geotech. J.* 37, 132–145.
- Jia, R., 2010. Consolidation behavior of Ariake clay under constant rate of strain. Dept. of Engng. Syst. a. Technol. Graduate School of Sci. a. Engng. Saga Univ., Saga, Japan.
- Kumarage, P.I., Gnanendran, C.T., 2019. Long-term performance predictions in ground improvements with vacuum assisted Prefabricated Vertical Drains. *Geotext. Geomembranes* 47, 95–103.
- Liu, K.W., Rowe, R.K., 2015. Numerical modelling of prefabricated vertical drains and surcharge on reinforced floating column-supported embankment behaviour. *Geotext. Geomembranes* 43, 493–505.
- Liu, M.D., Xu, K.J., Horpibulsuk, S., 2013. A mathematical function to represent S-shaped relationships for geotechnical applications. *Proceedings of the Institution of Civil Engineers - Geotechnical Engineering* 166, 321–327.
- Long, R.P., Covo, A., 1994. Equivalent diameter of vertical drains with an oblong cross section. *Journal of Geotechnical Engineering* 120, 1625–1630.
- Murad, M.A., Loula, A.F.D., 1994. On stability and convergence of finite element approximations of Biot's consolidation problem. *Int. J. Numer. Methods Eng.* 37, 645–667.
- Nguyen, B.-P., Kim, Y.-T., 2019. Radial consolidation of PVD-Installed normally consolidated soil with discharge capacity reduction using large-strain theory. *Geotext. Geomembranes* 47, 243–254.
- Nguyen, C.-O., Tran, T.T., 2015. Consolidation Analysis of Vietnam Soft Marine Clay by Finite Difference Method with Application of Constant Rate of Strain Consolidation Test, *Geotechnique, Construction Materials and Environment*. pp. 271–276 Osaka, Japan.
- Nguyen, Q.P., Giao, Huy, 2014. Improvement of Soft Clay at a Site in the Mekong Delta by Vacuum Preloading *Geomechanics and Engineering*, vol 6. pp. 419–436.
- Ni, P., Xu, K., Mei, G., Zhao, Y., 2019. Effect of vacuum removal on consolidation settlement under a combined vacuum and surcharge preloading. *Geotext. Geomembranes* 47, 12–22.
- Ozer, A.T., Lawton, E.C., Bartlett, S.F., 2011. New method to determine proper strain rate for constant rate-of-strain consolidation tests. *Can. Geotech. J.* 49, 18–26.
- Pham, H.T., Rühaak, W., Schulte, D., Sass, I., 2019a. Application of the Vimeke-Taylor concept for fully coupled models of consolidation by prefabricated vertical drains. *Comput. Geotech.* 116 103201.
- Pham, H.T., Rühaak, W., Schuster, V., Sass, I., 2019b. Fully hydro-mechanical coupled Plug-in (SUB+) in FEFLOW for analysis of land subsidence due to groundwater extraction. *Software* 9, 15–19.
- Reed, M.B., 1984. An investigation of numerical errors in the analysis of consolidation by finite elements. *Int. J. Numer. Anal. Methods Geomech.* 8, 243–257.
- Rujikiatkamjorn, C., Indraratna, B., 2006. Three-Dimensional Numerical Modeling of Soft Soil Consolidation Improved by Prefabricated Vertical Drains, *Ground Modification and Seismic Mitigation*.
- Rujikiatkamjorn, C., Indraratna, B., Chu, J., 2008. 2D and 3D numerical modeling of combined surcharge and vacuum preloading with vertical drains. *Int. J. Geomech.* 8, 144–156.
- Sheng, D., Sloan, W.S., 2003. Time stepping schemes for coupled displacement and pore pressure analysis. *Comput. Mech.* 31, 122–134.
- Shoji, M., Ohta, H., Arai, K., Matsumoto, T., Takahashi, T., 1990. Two-Dimensional consolidation back-analysis. *Soils Found.* 30, 60–78.
- Suzuki, K., Takeuchi, H., 2008. Performance OF band shaped vertical drain for soft hai PHONG clay. *Soils Found.* 48, 577–585.
- Suzuki, K., Yasuhara, K., 2004. Two case studies OF consolidation settlement analysis using constant rate OF strain consolidation test. *Soils Found.* 44, 69–81.
- Terzaghi, K., 1943. *Theoretical Soil Mechanics*. Wiley Online Library.
- Verruijt, A., 2016. *PoroElasticity*. <http://geo.verruijt.net/>.
- Wissa, A., 1971. Consolidation at constant rate of strain. *J. Soil Mech. Found. Div.* <https://trid.trb.org/view/127864>.



---

---

## **5. Application of the Vimoke-Taylor concept for fully coupled models of consolidation by prefabricated vertical drains**

---

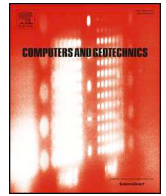
This chapter is reproduced from: Pham HT, Rühaak W, Schulte D, Sass I. *Application of the Vimoke–Taylor concept for fully coupled models of consolidation by prefabricated vertical drains*. Computers and Geotechnics (Pham, Rühaak, Schulte, et al., 2019).



ELSEVIER

Contents lists available at ScienceDirect

## Computers and Geotechnics

journal homepage: [www.elsevier.com/locate/compgeo](http://www.elsevier.com/locate/compgeo)

Research Paper

## Application of the Vimoke–Taylor concept for fully coupled models of consolidation by prefabricated vertical drains

Hung Tien Pham\*, Wolfram R uhaak, Daniel Schulte, Ingo Sass

Institute of Applied Geosciences, Technische Universit at Darmstadt, Germany

## ARTICLE INFO

## Keywords:

3D PVDs  
 Vimoke–Taylor concept  
 Consolidation  
 Biot's theory  
 Vertical drains  
 Vacuum pumping

## ABSTRACT

Prefabricated vertical drains (PVDs) are widely used to accelerate consolidation processes of soft soils. Each PVD has a specific influence zone that is idealised as a cylinder, which is called a unit cell. The behaviour of a PVD system is usually analysed by analytical or numerical models of a unit cell model. Fully three-dimensional (3D) models of PVD systems are still a challenge due to the small size of PVDs and radial flows around PVDs, which result in a dense mesh around the PVDs and excessive computational efforts. In this study, the Vimoke–Taylor concept, which is typically used in the hydrology field, is applied to decrease the difficulties of computing 3D finite element (FE) models for PVD systems. The correction factor of the Vimoke–Taylor concept is determined by minimising the defined error between the analytical solution and the numerical result of a simple unit cell model. The correction factor depends on drained-zone size, PVD size, smear-zone size, and 3D FE mesh properties.

## 1. Introduction

Prefabricated vertical drains (PVDs) combined with surcharge loading and vacuum pumping methods are widely used all over the world to accelerate the consolidation process of soft soils. PVDs are band-shaped (typically 100 mm × 4 mm) and have channelled plastic cores wrapped with geotextile filters. Water from soft soils passes through the geotextile filter and then flows along the channelled core to the free surface. Instead of vertical flow, water flow is radial, and the length of the drainage path is shortened significantly. The consolidation rate is thus speeded up. PVDs are often installed in a triangular or square pattern with an appropriate distance using a special machine that has the mandrel to push PVDs into the soils. The mandrel can disturb the soils around PVDs and create the smear-zone.

Behaviours of PVD systems are usually analysed by an analytical or numerical model. With the analytical model, each PVD has a specific influential zone that is idealised as a cylinder called a unit cell. Using the axisymmetric model of the unit cell, Barron [1] first developed solutions for different cases: free strain with or without the smear-zone and equal strain with or without the smear-zone. However, those solutions are complicated due to the involvement of Bessel functions, which are difficult to compute. Therefore, Hansbo [2] developed a simpler solution for equal strain cases that has been applied regularly because it is easy to calculate. Following either Barron or Hansbo's

solution, the excess pore pressure of any point inside a unit cell at any time during the consolidation time can be computed.

Finite element (FE) models of PVD systems are typically used to study more complicated problems, for instance, different scenarios of surcharge loads, varied length of PVDs or multi-layers of soils. A PVD system can be analysed with a 2D axisymmetric model of a unit cell, a 2D plane strain model or a full 3D model. While 2D models are used extensively for practical purposes, 3D models have not been published often. Particular exceptions include Rujikiatkamjorn [3,4], where a large cylindrical unit cell (450 mm diameter and 850 mm height) and a PVD system (a 14 × 25 × 20 m treated zone with 350 PVDs) were modelled in ABAQUS using solid elements. The drained boundary condition (i.e. the excess pore pressure is zero) was assigned for elements along PVDs to simulate the perfect drain condition. In those studies, although both PVDs and smear-zones were rectangular to simplify the FE meshes, meshes around PVDs were still dense due to small sizes of PVDs. In case of the unit cell, approximately 1000 3D elements were used to represent a quarter of the unit cell. If a similar mesh is used for an upscale model with hundreds of PVD, the number of elements is up to millions that results in excessive computational efforts.

Additionally, water flow into vicinity areas of PVDs is characterised as radial flow. Hence, the excess pore pressure varies logarithmically with radial distance. Therefore, in numerical models, meshes around

\* Corresponding author at: Schnittspahnstra e 9, 64287 Darmstadt, Germany.

E-mail address: [pham@geo.tu-darmstadt.de](mailto:pham@geo.tu-darmstadt.de) (H.T. Pham).

<https://doi.org/10.1016/j.compgeo.2019.103201>

Received 5 September 2018; Received in revised form 11 June 2019; Accepted 2 August 2019

0266-352X/  2019 Elsevier Ltd. All rights reserved.

Nomenclature	
$s$	distance between each PVD [m]
$r_e$	radius of a unit cell [m]
$r_w$	equivalent radius of a PVD [m]
$r_s$	equivalent radius of a smear-zone [m]
$H$	height of a unit cell [m]
$b, t$	thickness and width of a PVD [m]
$w, l$	length and width of a smear-zone [m]
$C_d$	correction factor [-]
$k (k_h \text{ or } k_v)$	hydraulic conductivity (horizontal or vertical direction) [m/s]
$k_s$	horizontal hydraulic conductivity of a smear-zone [m/s]
$k_s/k_h$	ratio between horizontal hydraulic conductivity of the smear-zone and the undisturbed zone [-]
$k_w$	hydraulic conductivity of PVD [m/s]
$q_w$	discharge capacity of PVD [m <sup>3</sup> /s]
$A_w$	section area of PVD [m <sup>2</sup> ]
$p_{analytical}$	excess pore pressure of a node obtained using analytical solutions [kPa]
$p_{numerical}$	excess pore pressure of a node obtained using finite element models [kPa]
$ns$	total of calculation step [-]
$n$	total of nodes for a finite element model [-]
$error$	error between numerical results and analytical solutions [%]
$c_r$	horizontal consolidation coefficient [m <sup>2</sup> /s]
$dt$	interval time between two calculation steps [s]
$p_0$	initial excess pore pressure [kPa]
$K$	bulk modulus [kN/m <sup>2</sup> ]
$G$	shear modulus [kN/m <sup>2</sup> ]
$\nu$	Poisson's ratio [-]
$v_{max}$	maximum settlement at the final calculation step [m]

PVDs must be refined with small elements to manage the radial flow. Otherwise, results from analyses are not reliable. For instance, Wong [5] compared results of an axisymmetric model in Plaxis2D, a 3D model in Plaxis3D for a simple unit cell with Barron's solutions. Although meshes around PVDs were dense, differences between the numerical results and the analytical solutions were still visible.

As discussed above, small sizes of PVDs and the radial flow lead to dense meshes around PVD boundaries in FE models of PVD systems, which causes significant increases in the number of nodes, the number of elements, and the total degrees of freedom, especially for fully coupled 3D models. In the hydrogeology field, modelling wells or pipes in groundwater models also encounter similar issues. Radii of wells and pipes are small compared to sizes of calculation domains. If wells or pipes are treated as drained boundaries, water flow around them is almost radial [6]. To overcome this problem, the Vimoke-Taylor (VT) concept has been considered as the most effective method [6]. The general idea of the VT concept is to represent drained boundaries, which are open spaces, by using centre nodes; and values of hydraulic conductivity around drained boundaries are modified with a correction factor  $C_d$  to account for open spaces and to deal with radial flow patterns [7]. Hence, when applying the VT approach for numerical models, meshes around drained boundaries do not need to be refined. Fipps [6] compared the VT approach with three other methods: "holes" in models, nodes with a specific value of water head and nodes with a specific value of discharge rate. He concluded that the VT method correctly predicts both hydraulic heads and drain flow rates even with a simple mesh. Then, because of its simplicity and accuracy, the VT concept has been used widely to simulate drained boundaries in groundwater models [8]. As PVDs are also treated as drained boundaries, the VT concept has a great potential for modelling PVD systems. Following the VT approach, the problem related to small elements

around PVDs can be solved.

In this paper, details about the VT concept and its implementation in 3D FE models of PVD systems are explained. FE models were developed based on Biot's theory (poroelasticity theory) with C++ programming language. Hence, the results of this study are also valid for geotechnical models that use Biot's theory for coupled consolidation analyses, e.g. linear model, elastic-plastic model or Cam-Clay model. The most important task of the VT concept is to determine the correction factor  $C_d$ . Thus far, there is still no final agreement about a general equation to estimate  $C_d$  in the hydrogeology field. However, it is common that the  $C_d$  factor is found by matching simulated water heads of a simple model to the analytical solution of Kirkham [8]. Based on that idea, a procedure to estimate the  $C_d$  factor for models of PVD systems was proposed, where  $C_d$  for a specific case is determined by matching numerical results of a unit cell to analytical solutions. Series of patch tests were performed to study factors that affect the  $C_d$  value. To demonstrate the advantages of the VT method, two 3D models were presented. The first model is a real project in Vietnam, and the second model is a large fictitious model.

## 2. Theory

### 2.1. Analytical solutions for unit cell models

From the installation pattern of a PVD system and the distance  $s$  between the PVDs, the radius of the unit cell  $r_e$  is calculated. The two most common installation patterns are square and triangular patterns (Fig. 1a and b). For the square pattern  $r_e = 0.565 \times s$ , and for the triangular pattern  $r_e = 0.53 \times s$ .

At the centre of the unit cell, the PVD has a thickness  $t$  and width  $b$ , and the length and width of the smear-zone are denoted as  $l$  and  $w$ ,

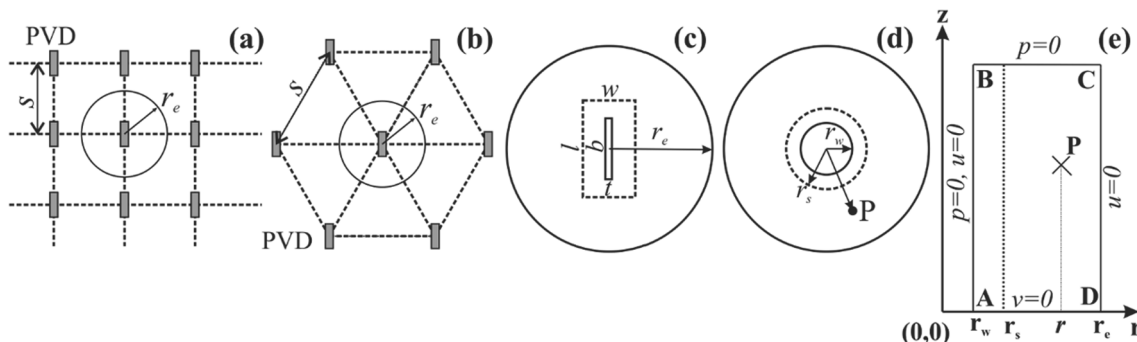


Fig. 1. (a, b) Square and triangular pattern; (c, d) Convert size of a PVD and a smear-zones into equivalent circular zones; (e) axisymmetric model of a unit cell.

respectively (Fig. 1c). These dimensions are converted into equivalent circular zones with radii  $r_w$  and  $r_s$ , respectively (Fig. 1d). According to Long and Covo [9]:

$$\begin{cases} r_w = 0.5 \times (0.5b + 0.7t) \\ r_s = 0.5 \times (0.5l + 0.7w) \end{cases} \quad (1)$$

At any time during the consolidation process, the excess pore pressure of a point P inside the unit cell (Fig. 1e), which has a radius  $r$ , can be obtained using solutions of Barron [1] or Hansbo [2].

### 2.2. Finite element models based on the poroelasticity theory

The poroelasticity theory or Biot's theory is used to develop FE models [10–13]. The displacement field is approximated by Galerkin's method with second-order elements, whereas the pore pressure field is approximated with first-order elements. Many researchers have pointed out that this approach is advisable for Biot's poroelasticity theory to avoid instability of numerical solutions [14,15]. Moreover, the backward interpolation and constant time steps are used for the time integration. These approaches give the most stable and accurate solutions [12]. Details on the development of the matrix system are found in the work of Verruijt [12] and Pham [16]. The FE code and verifications are provided on GitHub (<https://github.com/pham-hung/VimokeTaylor-PVDs>).

### 2.3. Vimoke–Taylor concept

When numerical models were not widely used to study seepage and groundwater flow in the past, analogue resistance networks were commonly used instead. For instance, in Fig. 2b, a horizontal homogenous aquifer with a well (drained boundary) in the middle, which is an open space, can be represented by an analogue resistance network (Fig. 2a). Vimoke and Taylor concluded that the open space could be replaced by a centre point in the resistance network, which is point-5 in Fig. 2a. However, the resistance from the adjacent points (point-1, 2, 3, 4) to the centre point (point-5) needs to be adjusted to account for the cross-section of the open space.

$$R_{drain} = C_d R \quad (2)$$

where  $R_{drain}$  is the adjusted resistance,  $R$  is the original resistance, and  $C_d$  is a dimensionless correction factor.

The VT concept then has been applied by many authors in numerical models, especially in combination with the finite volume method [8]. For example, the aquifer is discretised by the grid, and the aquifer has the hydraulic conductivity  $k$  (Fig. 2b and c). The hydraulic conductivity is the inverse of the resistance or  $k = 1/R$ . According to VT, the hydraulic conductivity of the drained cell  $k_{drain}$  is modified with the same correction factor  $C_d$ :

$$k_{drain} = C_d k \quad (3)$$

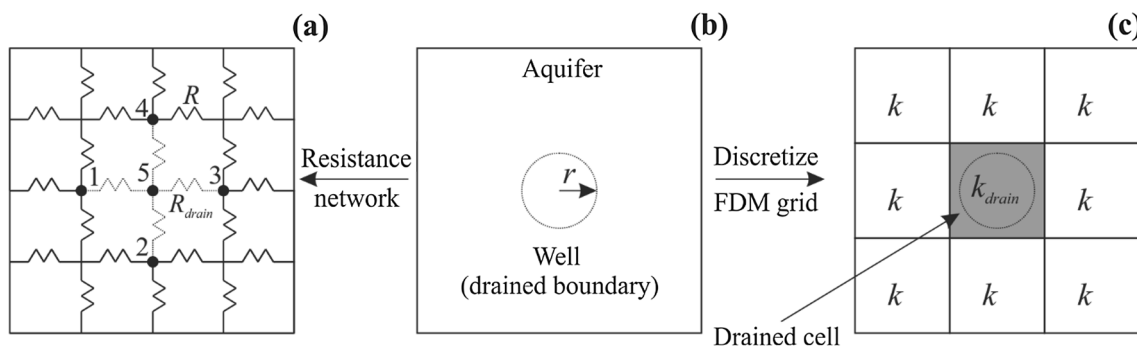


Fig. 2. Discretise a domain with a drained boundary with a resistance network and a finite difference grid.

## 3. Implementation of the Vimoke–Taylor concept in 3D FE models of PVD systems

### 3.1. Meshing strategy

Assume that a 3D model is needed for a  $5 \times 5 \times 10$  m block. The block includes the typical  $100 \times 4$  mm PVDs with  $240 \times 120$  mm smear-zones, which are twice the size of a regular mandrel  $120 \times 60$  mm. Sizes of the PVDs and the smear-zones are much smaller than the dimensions of the block. If the actual shapes of the PVDs and the smear-zones are considered (Fig. 3a), many small elements are necessary to mesh the smear-zones. When the PVDs and the smear-zones are converted into equivalent circular zones (Fig. 3b), the situation is not much improved because the radii of the equivalent zones are still small compared to the model dimensions. Furthermore, many segments are required to represent curved surfaces of cylinders. In both cases (Fig. 3a and b), the number of nodes and elements of the meshes increase quickly because of the necessary refinement around the PVDs and the smear-zones.

Applying the VT concept is a huge improvement in this case. At the centre position of each PVD, a zone called drained-zone represents both the smear-zone and the PVD-zone. In Fig. 3c, the drained-zone has a square cross-section, and it is divided into four smaller zones. The centre points of the drained-zones are assigned the drained boundary condition (i.e. the excess pore pressure  $p$  is zero) or 1D elements can be assigned along these points. The horizontal hydraulic conductivity of the drained-zones is modified as:

$$k_{hd} = C_d k_h \quad (4)$$

where  $k_{hd}$  is the horizontal hydraulic conductivity of the drained-zones,  $C_d$  is the correction factor, and  $k_h$  is the horizontal hydraulic conductivity of undisturbed soils. The vertical hydraulic conductivity is kept unchanged.

When the shape and the dimension of the drained-zones are chosen appropriately, small elements for the PVD-zones and the smear-zones are no longer necessary. Consequently, fewer nodes and elements are used to model the system, which results in a significant reduction of the computational effort.

Four primitive geometries of 3D FEs can be used: tetrahedron, hexahedron, prism, and pyramid; Fig. 4 shows the second-order of all four element types, namely Tet10p, Hex20p, Prism15p and Pyra13p, respectively. If the geometry of a model is simple, the hexahedral and prismatic elements are ideal because the number of nodes and elements can be significantly decreased in comparison to a mesh using tetrahedrons only. However, for complex geometries, meshing with hexahedra and prisms is a challenging task, or it might be impossible. Hence, mixing element types is a suitable strategy. When zones cannot be discretised with hexahedra and prisms, tetrahedrons are used. Then, these elements connect with adjacent elements using pyramidal elements.

Because of the radial flow, drained-zones should be symmetrical.

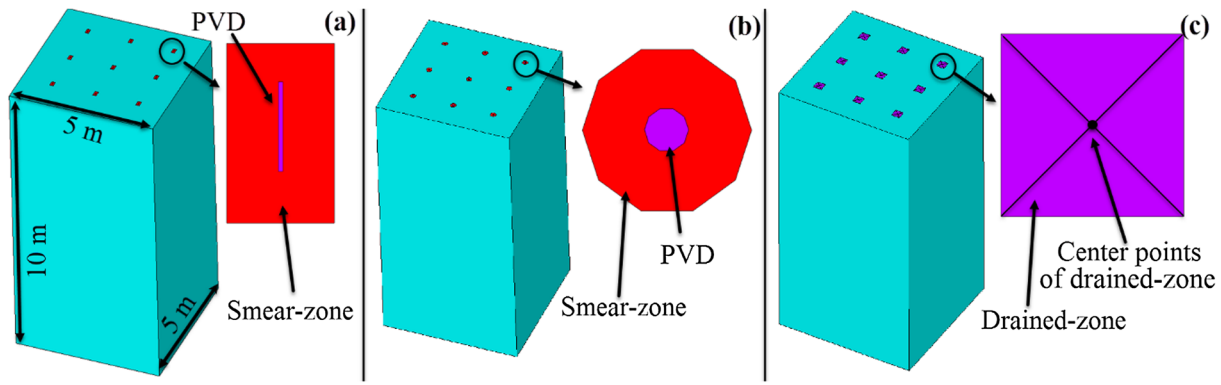


Fig. 3. Different strategies to mesh a 3D model of a PVD system; (a) Actual shape of PVD and smear-zone; (b) Equivalent circular zones; (c) Apply Vimoke–Taylor concept.

Preferably, the drained-zones are cylindrical (Fig. 5a). However, in FE models, curved lines or curved surfaces must be divided into smaller segments. Therefore, if the drained-zones are approximated as cylinders, many nodes and elements are required to represent curved lines and surfaces, respectively. Conversely, if the drained-zones have a block-shape with a square cross-section, fewer nodes and elements are needed. For instance, in Fig. 5, 160 prismatic elements are used for a cylindrical drained-zone (Fig. 5a), whereas only 36 elements are used if the drained-zones have a square cross-section (Fig. 5b and c). However, the square cross-section has a minor disadvantage. It is not perfectly symmetrical.

If drained-zones have a square cross-section, they can be discretised with either the hexahedral or prismatic element type (Fig. 5b and c). The number of elements for the drained-zones in both cases is the same. However, because the edge size of the hexahedra is half of the prisms, more elements around the drained-zone are required for the former case in comparison with the latter. For example, in Fig. 5d, two pyramidal elements are used to connect an edge of the drained-zone, which is meshed with the hexahedral element. However, only one element is enough if the prismatic element is used instead (Fig. 5e). For large 3D models with many PVDs, this difference is noticeable.

In conclusion, for practical purposes, drained-zones should have a square cross-section, and the prismatic element should be used for the drained-zones.

### 3.2. A procedure to determine the correction factor

The most important task of the VT approach is to estimate the correction factor  $C_d$  in Eqs. (3) and (4). In the hydrology field, there has not yet been an agreement about a general formula to determine the  $C_d$  value [8]. However, it is common that  $C_d$  is estimated by matching simulated water heads of a simple model to the analytical solution of Kirkham [8]. From that idea, if a unit cell model and the analytical solutions of Barron or Hansbo are used instead, a similar scheme can

also be used to determine the  $C_d$  factor for a 3D model of a PVD system.

The analytical solutions depend on the PVD size, the smear-zone size, the soil properties, the PVD discharge capacity and the ratio between the horizontal hydraulic conductivity of the smear-zone and the undisturbed zone  $k_s/k_h$ . Hence, the correction factor  $C_d$  can also be affected by those parameters. Concerning 3D FE models, the  $C_d$  factor can be decided by mesh properties of drain-zones and soil-zones (i.e. element size and element type). Hereby, the soil-zones are the rest of the 3D models, which are not the drained-zones. Therefore, it can be preliminarily concluded that the  $C_d$  factor of a unit cell model can be applied for a 3D model of a PVD system if both models have the same properties of the drained-zone, the PVD, the smear-zone, the soils, and the FE mesh.

Based on the above discussions, a procedure to determine the correction factor  $C_d$  is suggested in Fig. 6. All parameters that can influence the  $C_d$  factor are considered. Instead of giving a general formulation to estimate the  $C_d$  factor, it is determined for each specific case.

Details of the process for determining the  $C_d$  factor are as follows:

- **Step 1:** From the PVD size and the mandrel size, equivalent radii  $r_w$  and  $r_s$  are calculated.
- **Step 2:** From the installation pattern of the PVD system, the unit cell radius  $r_e$  is calculated.
- **Step 3:** Create a simple unit cell model with the radius  $r_e$ . The unit cell has a drained-zone in the middle. The size and the shape of the drained-zone are discussed in Section 3.1.
- **Step 4:** Mesh the unit cell with the chosen element type (hexahedron, tetrahedron, or prism).
- **Step 5:** Calculate analytical solutions of the excess pore pressure field. Calculations are performed for every node of the unit cell model, for every calculation step.
- **Step 6:** Minimise the error (equation (5)) between analytical solutions and numerical results by using an optimisation method. In this study, the golden section method [17] was used to determine the  $C_d$

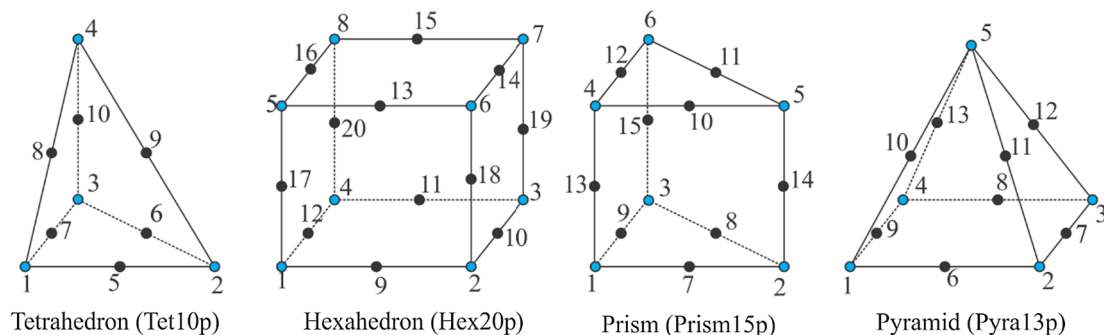


Fig. 4. Four different second-order element types for 3D models.

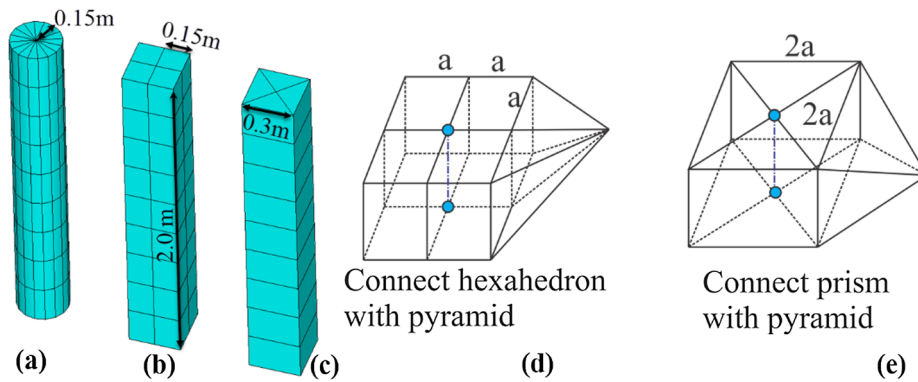


Fig. 5. Different shapes and element types for drained-zones; (a) The drained-zone is a cylinder with prismatic elements; (b) The drained-zone has a square cross-section with hexahedral elements; (c) The drained-zone has a square cross-section with prismatic elements; (d, e) Connected hexahedra and prisms with pyramids.

factor within a given range (usually authors use the range from 0.1 to 2.0) that gives the minimum error. The error is calculated as:

$$error = 100 \times \frac{\sum_{i=1}^{ns} \sum_{j=1}^n \left| \frac{p_{numerical} - p_{analytical}}{p_{analytical}} \right|}{ns \times n} (\%) \quad (5)$$

In Eq. (5),  $ns$  is the number of calculation steps,  $n$  is the number of nodes, and  $p_{numerical}$  and  $p_{analytical}$  are excess pore pressure values of the node  $j$  at the calculation step  $i$ .  $p_{numerical}$  is obtained from the 3D model of the unit cell, and it changes according to  $C_d$ . From coordinates of node  $j$ ,  $p_{analytical}$  is calculated by using solutions of Barron or Hansbo. Although  $p_{numerical}$  must be determined again for each  $C_d$  value,  $p_{analytical}$  for all nodes is calculated only once. In principle, both solutions of Barron [1] and Hansbo [2] for equal strain or free strain cases can be used to compute  $p_{analytical}$ . However, as the free strain analysis is closer to reality than the equal strain analysis, Barron's solutions for free strain cases are used in this study.

In Step 3, because only the radial drain is considered, the height of the unit cell model has no effect on the analytical solutions, except when the well resistance is considered. Hence, the unit cell model height is chosen based on the element size of the drained-zone, and it should not be too large to save computational time. For example, if the drained-zone is meshed with hexahedra that have a 0.2 m height, the unit cell model height can be from 1.0 m to 2.0 m (five to ten times of the hexahedral height).

Step 6 is an iterative process. The number of iterations depends on the tolerance of the golden section method (i.e. the difference of  $C_d$  value between two consecutive steps) and the range of  $C_d$ . If the tolerance is small or the search range is large, more iterations are needed. In this study, the  $C_d$  range is from 0.1 to 2.0, and the tolerance is 0.001.

With this setting, most cases can be satisfied, and the number of iterations varies from 14 to 16.

### 3.3. Patch tests to study dependence of the correction factor

As mentioned in Section 3.2, there are numerous factors that can affect the correction factor  $C_d$ . Serial tests with unit cell models are used to verify the proposed procedure and to investigate influences of each factor. Unit cell models have the height  $H$  (m) with the square cross-section of the drained-zones. Six patch tests (PTs) are implemented to study the dependence of the correction factor  $C_d$ .

- **PT1:** All models have the same parameters except the sizes of the drained-zones. The cross-sections of the drained-zones are square, and the prismatic element is used both for the drained-zones and the soil-zones.
- **PT2:** The drained-zone and the soil-zone are meshed with different element types. The other parameters are the same for all models. PT2 examines how element types affect the correction factor.
- **PT3:** PT3 studies the effects of PVD and smear-zone sizes on the factor  $C_d$ . Other parameters are kept constant.
- **PT4:** All parameters related to PVDs and soils are identical. The drained-zone is meshed with different element sizes but with the same element type. PT4 investigates the dependence of  $C_d$  factor on the number of nodes, the number of elements or the element size.
- **PT5:** Soil properties vary, but the correction factor  $C_d$  and other parameters do not change. PT5 is very important if soil parameters depend on the effective-stress or the void ratio.
- **PT6:** From PT1 to PT5, the well resistance is ignored. For PT6, PVDs are modelled using 1D elements (two nodes) with limited hydraulic

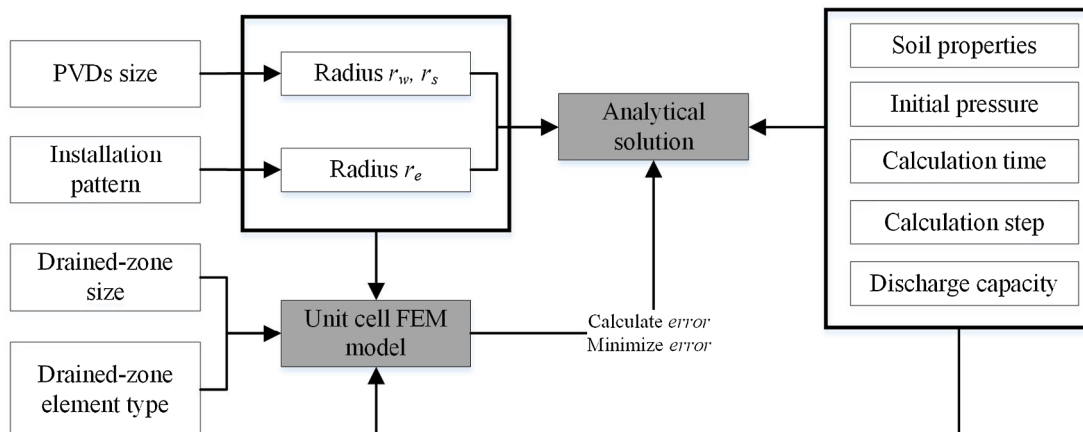


Fig. 6. Proposed procedure to determine the correction factor  $C_d$ .

conductivity. A  $C_d$  factor for a model without the well resistance is determined first. Then, this factor is used for models with different discharge capacity.

Fig. 7 shows a typical 3D FE model of a unit cell, which has a radius  $r_e$ , a height  $H$  and a square-cross section of the drained-zone. The horizontal hydraulic conductivity of the drained-zone is modified with the correction factor or  $k_{hd} = C_d \times k_h$ . The bottom boundary has no vertical movement, and the outer boundaries have no horizontal movement (roller boundary condition type). Pressure is applied to the top boundary to cause the initial excess pore pressure  $p_0$ . If the well discharge is not considered, nodes that belong to the centre line are assigned the drained boundary condition (excess pore pressure  $p$  is zero). Otherwise, 1D elements are created along the centre line. The top and the bottom nodes are drainage points.

4. Results of the patch test

4.1. PT1: Influence of drained-zone size on the correction factor

The common parameters for all models are:  $r_e = 0.6$  m,  $r_w = 0.0264$  m, no smear-zone,  $c_r = 2 \times 10^{-7}$  m<sup>2</sup>/s,  $k_v = 1 \times 10^{-9}$  m/s,  $k_h = 2k_v$ ,  $p_0 = 100$  kPa,  $dt = 43200$  s,  $ns = 100$  and  $H = 2.0$  m. The correction factor is determined with the procedure that is described in Fig. 6, and the minimum error is calculated by Eq. (5).

Apparently, the correction factor depends on the drained-zones size (Table 1). Moreover, the smaller the smear-zone, the smaller the minimum error. However, decreasing the drained-zones size leads to an increase in the total number of nodes. For example, Case-1 and Case-3 have 0.2 m and 0.4 m drained-zone (square cross-section), respectively. The total number of nodes in Case-1 is 1.7 times more than in Case-3. For 3D models of PVD systems, this difference is a huge problem, whereas, the error of Case-1 and Case-4 is 0.61% and 1.35%, respectively.

Generally, the drained-zone size should be chosen according to the purposes of an analysis and capacity of computers. If a high accuracy of the analysis is required, the smear-zone size can be small. However, if the computer has a limited calculation power, the smear-zone size can be larger to reduce the total of nodes.

4.2. PT2: Influence of element types on the correction factor

The common parameters for all models are:  $r_e = 0.5$  m,  $r_w = 0.03$  m,  $r_s = 0.1$  m,  $c_r = 1 \times 10^{-7}$  m<sup>2</sup>/s,  $k_v = 3e-10$  m/s,  $k_h = 2k_v$ ,  $k_s/k_h = 0.6$ ,  $p_0 = 100$  kPa,  $dt = 86400$  s,  $ns = 100$  and  $H = 2.0$  m. The square cross-section of the drained-zones is  $0.3 \times 0.3$  m.

For a unit cell model, the drained-zone is meshed first to ensure a uniform mesh (from top to bottom). Hence, when Tet10p is used for the

Table 1  
PT1 – Description and results.

Case	Drained-zone size (m)	Total number of nodes	$C_d$	Minimum error (%)
1	0.2	1681	0.924	0.61
2	0.3	1485	0.766	0.80
3	0.4	995	0.660	1.35

Table 2  
PT2 – Description and results.

Case	Drained-zone element type	Soil-zone element type	Number of nodes	$C_d$	Minimum error (%)
1	Hex20p	Hex20p	2147	0.911	1.18
2	Hex20p	Prism15p	1809	0.902	1.40
3	Hex20p	Tet10p	2206	0.896	1.41
4	Prism15p	Hex20p	2351	0.586	1.15
5	Prism15p	Prism15p	2105	0.577	1.02
6	Prism15p	Tet10p	2483	0.571	1.32
7	Tet10p	Tet10p	2075	0.616	3.13

drained-zone, only Tet10p can be used for the soil-zone too. To avoid the effect of element size on the correction factor, all cases have nearly the same number of nodes.

Table 2 shows the clear dependence of the correction factor on the element type used for the drained-zone. When the element type for the drained-zone is kept unchanged (Case-1, 2, 3 and Case-4, 5, 6), the  $C_d$  values are not much varied if the soil-zone is meshed with different element types. For instance, in Cases-1, 2 and 3, the  $C_d$  value is 0.911, 0.902, and 0.896, respectively. These values can be used interchangeably if models do not require high accuracy.

It is also noticeable that the error of Case-7 is the largest. Hex20p and Prism15p are created by extruding a rectangle or a triangle. Hence, the mesh of a drained-zone with Hex20p and Prism15p is uniform (from top to bottom). However, Tet10p is created by the Delaunay triangulation algorithm. Thus, a uniform mesh is difficult to achieve. This is the reason why Case-7 has a larger error than the others. Therefore, the tetrahedral element type is not recommended to mesh drained-zones.

4.3. PT3: Influence of PVD and smear-zone size on the correction factor

Drained-zones ( $0.3 \times 0.3$  m) are meshed with Prism15p, and Tet10p is used for the rest. The constant parameters for all models are:  $r_e = 1.0$  m,  $c_r = 2 \times 10^{-7}$  m<sup>2</sup>/s,  $k_v = 5 \times 10^{-10}$  m/s,  $kh = 3k_v$ ,  $k_s/k_h = 0.33$ ,  $p_0 = 150$  kPa,  $dt = 86,400$  s,  $ns = 100$  and  $H = 5.0$  m.

For each case in Table 3, the correction factor  $C_d$  is unique. Thus, the  $C_d$  factor must be determined again when sizes of the PVD and the smear-zone change.

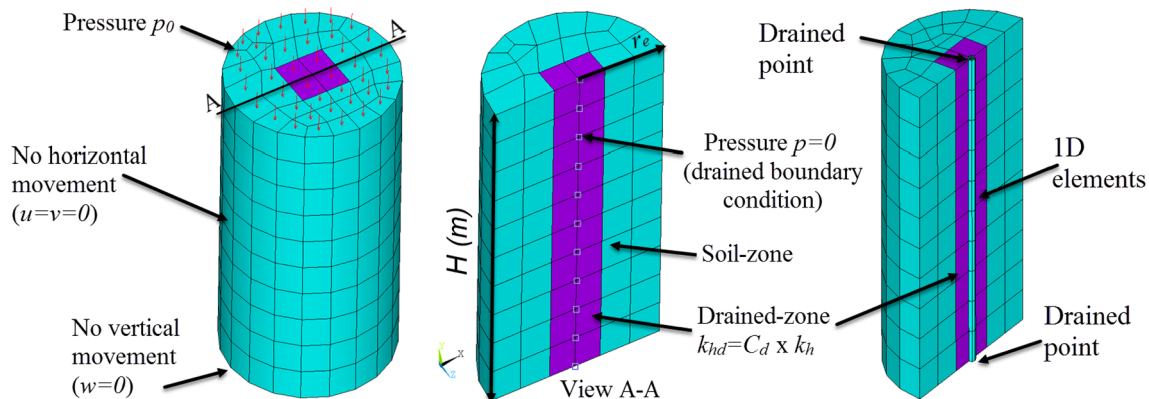


Fig. 7. A 3D FE model of a simple unit cell.

**Table 3**  
PT3 – Description and results.

Case	$r_w$ (m)	$r_s$ (m)	Note	$C_d$	Minimum error (%)
1	0.01	–	No smear-zone	0.501	0.44
2	0.02	–	No smear-zone	0.648	0.55
3	0.03	–	No smear-zone	0.783	0.65
4	0.01	0.05	With smear-zone	0.247	0.28
5	0.02	0.1	With smear-zone	0.280	0.33
6	0.03	0.15	With smear-zone	0.304	0.41

4.4. PT4: Influence of mesh sizes on the correction factor

All parameters used for PT4 are taken from Case-4 of PT3 except the element size. The soil-zone is meshed with varied element sizes that lead to differences in the number of nodes (Table 4). As a general rule of the FE method, the smaller the element size is, the more accurate the result is. The number of nodes does not affect only excess pore pressure results but also the displacement field. Therefore, the maximum settlement  $v_{max}$  (m) at the final calculation step and relative differences  $\epsilon$  (%) in  $v_{max}$  between Case-1, which has the average mesh size, and other cases are considered.

Overall, the results from Table 4 show that the effect of the element size on the correction factor is trivial. Case-1, 2 and 3 have nearly the same correction factor  $C_d$  and the maximum settlement  $v_{max}$ . In Case-4, the  $C_d$  is 0.243 and is slightly smaller compared to Case-1 (0.247). If the same correction factor from Case-1 is applied to Case-4 (Case-5), error increases from 1.11% to 1.16% and the relative difference  $\epsilon$  between Case-1 and Case-5 is 1.92%.

Choosing an appropriate element size, which produces an acceptable result, is a general topic of the FE method that is not discussed here. However, results from PT4 suggest that the unit cell and the up-scale model should have a similar mesh size to achieve the best results when applying the VT concept.

4.5. PT5: Influence of soil properties on the correction factor

Soil properties here refer to the vertical hydraulic conductivity and the consolidation coefficient that can change during the consolidation process. Usually, the ratios  $k_h/k_v$  and  $k_s/k_h$  are assumed to be constant over calculation time and are given in advance.

Prism15p is used for all models, and the common parameters are:  $r_e = 0.6$  m,  $r_w = 0.03$  m,  $r_s = 0.10$  m,  $ns = 100$ ,  $k_h/k_v = 2$ ,  $k_s/k_h = 0.5$ ,  $p_0 = 150$  kPa and  $H = 2.0$  m. The constant time step of each test is determined so that all tests have the same degree of consolidation at the final step.

The  $C_d$  is determined for Case-1, and it is then applied to other cases. Table 5 shows that all models have the same error. It means the  $C_d$  does not depend on the soil properties. This result agrees with the original study of Vimeke and Taylor [7], where the  $C_d$  factor was not affected by the electric analogue resistance. Because of this characteristic, the VT concept is easy to apply to a nonlinear problem where soil properties change during consolidation processes, for instance, the hydraulic conductivity and the bulk modulus are effective stress dependent. The  $C_d$  factor is determined only once with an arbitrary parameter set; then, it can be applied to the whole simulation time.

4.6. PT6: Influence of discharge capacity

The  $C_d$  factor and the model from PT5 are used with different PVD discharge capacities  $q_w$ . The other parameters are:  $ns = 100$ ,  $k_s/k_h = 0.5$ ,  $c_r = 5 \times 10^{-7}$  m<sup>2</sup>/s,  $k_v = 1 \times 10^{-9}$  m/s,  $k_h = 2k_v$ ,  $p_0 = 100$  kPa and  $dt = 8640$  s. To consider the discharge capacity, 1D elements [18] that have the hydraulic conductivity  $k_w$  and the cross-section area  $A_w$  are used to model PVDs.

Table 6 shows that the discharge capacity  $q_w$  does not affect the

correction factor  $C_d$ . It is reasonable because the well resistance does not alter the radial flow. Hence, to be simpler, the  $C_d$  factor is determined with models that have infinity discharge capacity (i.e. PVD is considered as drained boundaries). Then, the factor can be used with any value of PVDs discharge capacity.

5. Application

This section shows two examples to demonstrate the advantages of the VT concept for 3D models of PVD systems. The first example is a real project in Vietnam. A full 3D unit cell model is developed. Then, the modelled results of the 3D model are compared with results from 2D axisymmetric model and real monitoring data. In this example, soil parameters that are obtained from constant strain rate tests and ASTM D4186 [19] depend on the vertical effective stress, but the correction factor is determined only once. This example aims to prove the exactness of the VT concept and the proposed procedure.

In the second example, a 3D fictitious model is developed to show how the VT concept can be applied to larger problems. The well resistance is ignored for both examples.

5.1. First example: A project from Vietnam

A factory in the South of Vietnam was constructed on a large area that has 17.5 m thickness of soft soil. The soil was improved by using PVDs combined with surcharge loads and vacuum pumps method to reduce the post-construction settlement and to shorten the construction time. The installation pattern of the PVDs is square with 1.0 m distance. Sizes of the PVDs and the mandrel are 100 mm  $\times$  4 mm and 120 mm  $\times$  60 mm, respectively.

The soil treatment process (Fig. 8) started with a 2.8 m reclamation layer, which was filled using the hydraulic method. A 0.5 m sand layer was subsequently added, followed by the installation of the PVDs. To hydraulically decouple the treated zone, a clay diaphragm wall system (6.0 m height and 1.2 m thickness) was built. On the top, a geotextile layer and impervious HDPE membranes covered all the treated area. Then, the vacuum pumps worked for nearly four months. During this period, a compensation filling layer was also added. The settlement of the original surface was monitored by surface settlement plates (SSPs) that were placed after installing PVDs.

The vacuum pressure is considered as a negative pore pressure on the top boundary and along the PVD boundary in the unit cell model. The load on the top is a combination of the reclamation layer, the sand layer, and the compensation layer. The development of the total load and the vacuum pressure during the construction period is shown in Fig. 9.

Nine constant rate of strain tests (CRSTs) from 0.0 m to 17.5 m depth were conducted. Next, the hydraulic conductivity and the bulk modulus of the CRS tests were calculated using ASTM D4186. Outputs are curves of the hydraulic conductivity and the bulk modulus that depend on the vertical effective stress. These curves are provided as supplementary materials.

For the square installation pattern of the PVDs with 1.0 m spacing, the radius of the unit cell is  $r_e = 0.565$  m. The equivalent radius of the PVDs is [9]:

**Table 4**  
PT4 – Description and results.

Case	Mesh size	Number of nodes	$C_d$	error (%)	$v_{max}$ (m)	$\epsilon$ (%)
1	Average	5665	0.247	0.28	-0.1560	0
2	Dense	18,865	0.248	0.16	-0.1556	-0.25
3	Coarse	4286	0.247	0.35	-0.1564	0.26
4	Very coarse	1641	0.243	1.11	-0.1575	0.71
5	Very coarse	1641	0.247	1.16	-0.1594	1.92

**Table 5**  
PT5 – Input parameters and results.

Case	$c_r$ (m <sup>2</sup> /s)	$k_h$ (m/s)	$dt$ (s)	$C_d$	Minimum error (%)
1	$1 \times 10^{-8}$	$1 \times 10^{-11}$	864,000	0.505	0.82
2	$5 \times 10^{-8}$	$5 \times 10^{-10}$	172,800	0.505	0.82
3	$1 \times 10^{-7}$	$1 \times 10^{-9}$	86,400	0.505	0.82
4	$5 \times 10^{-7}$	$3 \times 10^{-9}$	17,280	0.505	0.82
5	$1 \times 10^{-6}$	$8 \times 10^{-9}$	8640	0.505	0.82

**Table 6**  
PT6- Input parameters and results.

Case	$q_w$ (m <sup>3</sup> /year)	$A_w$ (m <sup>2</sup> )	$k_w$ (m/s)	$C_d$	Minimum error (%)
1	1	$2.28 \times 10^{-3}$	1.12E-05	0.505	0.88
2	10	$2.28 \times 10^{-3}$	1.12E-04	0.505	0.87
3	100	$2.28 \times 10^{-3}$	1.12E-03	0.505	0.88
4	200	$2.28 \times 10^{-3}$	2.24E-03	0.505	0.88
5	500	$2.28 \times 10^{-3}$	5.61E-03	0.505	0.88

$$r_w = \frac{0.5 \times 0.1 + 0.7 \times 0.004}{2} = 0.0264 \text{ m} \tag{6}$$

The smear-zone is twice the size of the mandrel [20]. Hence, the equivalent radius  $r_s$  of the smear-zone equals to:

$$r_s = 2 \times \frac{0.5 \times 0.12 + 0.7 \times 0.06}{2} = 0.102 \text{ m} \tag{7}$$

Additionally, the horizontal hydraulic conductivity of the smear-zone is equal to the vertical hydraulic conductivity of the undisturbed zone [20]. In this study area, the horizontal hydraulic conductivity is three times higher than the vertical hydraulic conductivity [21].

To prove the advantages of the VT concept, two models are performed, which are: a full 3D unit cell model with the VT correction (Fig. 10b) and a 2D axisymmetric model with a fine mesh (Fig. 10c). Both models are divided into nine layers, corresponding to the nine CRS tests. The first layer has 1.5 m thickness, and others have 2.0 m thickness. The 3D model contains 1872 prismatic elements. The simple unit cell model (Fig. 10a) that is used to determine the correction factor has a  $0.3 \times 0.3$  m drained-zone, 0.565 m radius and 2.0 m height. The correction factor found with the proposed procedure is 0.326.

Although the mesh of the 3D model is coarse (only 1872 elements) and the 2D mesh is much denser, results from both models are almost identical, which agree well with monitoring data during the vacuum

pumping period (Fig. 10d).

5.2. Second example: A fully coupled 3D model of a PVD system

A foundation (Fig. 11) is improved with PVDs and surcharge loads that can derive from filling layers or structural loads on the top boundary. The installation pattern of the PVDs is 1.5 m  $\times$  1.5 m square (Fig. 11b). In this example, an axisymmetric model cannot give the horizontal deformation of the foundation. Hence, a full 3D model is more suitable.

The properties of the PVDs are similar to those described in the first example (Section 5.1), and the smear-zone is not considered. The surcharge load is 150 kPa, and the total consolidation time is 100 days. The calculation step is 1 day with no sub-step. The drained boundary condition is set along the PVDs and on the top boundary. Soil properties are as follows:  $k_h = 1 \times 10^{-9}$  m/s;  $k_v = 5 \times 10^{-10}$  m/s; Bulk modulus  $K = 500$  kN/m<sup>2</sup> and Poisson's ratio  $\nu = 0.2$ . The determined correction factor  $C_d$  is 0.741.

Fig. 12 shows the horizontal deformation and the excess pore pressure of the last calculation step (after 100 days). The maximum horizontal deformation is quite large (0.271 m). If an axisymmetric model is used for the analysis, this deformation is ignored, which is inappropriate in reality.

The calculation was performed with a core i7-6800k and 64 GB RAM system. The total degree of freedom is almost half a million. The calculation program allocates less than 21 GB of RAM for the direct sparse matrix solver. Each calculation step takes nearly 85 s and the correction factor  $C_d$  was found within four minutes.

If the actual shape or the equivalent zones of the PVDs are considered, the used computer cannot handle the mesh and the matrix solver. Thus, the advantage of the VT concept is apparent.

6. Discussion

The study proposed a new method based on the Vimoke–Taylor concept, which has not been applied before, for modelling 3D PVDs systems. Instead of considering the actual size of the PVD and the smear-zone, which results in very small elements around the PVD, the drained-zone is used to represent both the PVD and the smear-zone, in which the horizontal hydraulic conductivity of the drained-zone is modified by a correction factor  $C_d$ . The method is simple, and it can be integrated easily into any numerical software. When applying the proposed approach, the number of nodes decreases, and computational

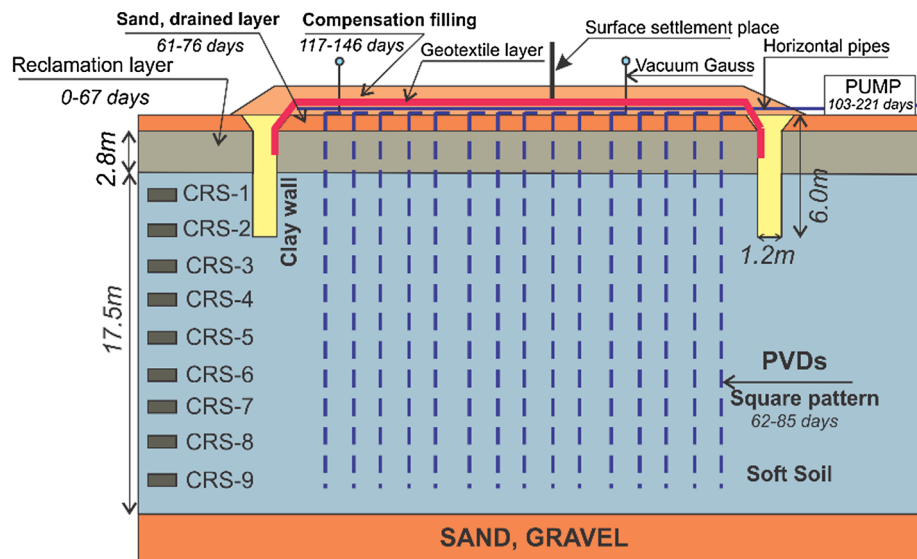


Fig. 8. Project scheme.

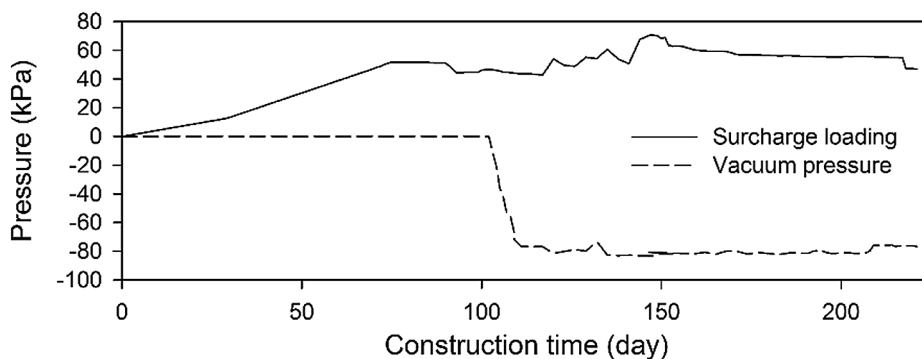


Fig. 9. The total load during construction time.

costs can be reduced significantly.

Section 5.2 presents an example of consolidation analyses, which can benefit from this study. Rather than using a plane strain model that cannot fully capture 3D effects or cannot consider a non-uniform load, the PVD system can be studied with a full 3D model. Other applications can be named here such as circular or square foundations, embankments with complicated sloping stratigraphy or varied soil layer thickness.

With a specific dataset, a correction factor  $C_d$  always can be determined by fitting numerical results with analytical solutions of a simple unit cell model. When applying the VT concept for 2D models, Fipps [6] concluded that the correction factor is affected by a square mesh surrounding a drain and a radius of the drain. From patch test results, a similar conclusion can be drawn.

First, instead of the square mesh of 2D models, the  $C_d$  factor for a 3D model depends on the size of the drained-zone. PT1 shows that when the drained-zone is smaller, the error is smaller. However, a small size leads to an increase in the number of elements. Hence, the size of the drained-zone can be adjusted according to a required accuracy of the model.

Second, the drained-zone should have a symmetrical and uniform mesh. Unlike 2D models, the drained-zone of a 3D model is a “box.” Hence, there are many types of 3D elements that can be used to mesh the drained-zone. To keep the mesh of the drained-zone uniform, it is better to use hexahedral elements or prismatic elements. The mesh is created by extruding two 2D elements along the PVD. PT2 shows that different element types of the drained-zone requires a different value of the correction factor. Additionally, tetrahedral elements should be avoided because it is difficult to have a uniform mesh with this element type. However, the element type of the soil-zone has not much effect on

the  $C_d$ .

Third, similar to the radius of the drain in groundwater models, the size of the PVD and the smear-zone affect the correction factor  $C_d$ . Results from PT3 indicate that  $C_d$  is unique for each dataset of the PVD and the smear-zone. It is reasonable because both the PVD and the smear-zone are represented by one centre line and one drained-zone. When the size of the drained-zone is given in advance, changing the size of the PVDs and the smear-zone results in changes of the drainage rate of the drained-zone. Hence, the  $C_d$  must be modified to adapt to these changes.

Four, from PT4, although the mesh size does not significantly impact the correction factor, it is always suggested that the meshes of the unit cell and the upscale model have a similar element size.

Finally, from PT5 and PT6, it is concluded that soil properties (i.e. the vertical hydraulic conductivity and the consolidation coefficient) and the discharge capacity of PVDs do not affect the  $C_d$  factor. As the major idea behind the VT concept is to manage the radial flow around the open space that does not depend on both soil properties and the discharge capacity, changing these parameters alter neither water flow direction nor the dimension of the drain.

Because the correction factor does not depend on the soil properties, the proposed method is valid for any geotechnical model that use Biot’s equations for consolidation analysis, for instance, the elastic-plastic model, or Cam–Clay model. In this study, Barron’s solutions were used. However, they can be replaced by any analytical solution without any problem. For example, Hansbo’s solution [2] can be used to simplify the analytical calculation, or Indraratna’s solution [22] is suitable when dealing with vacuum pressure. In general, the procedure in Section 3.2 is capable of being applied to other analyses that have the same issues as 3D models of PVD systems. PVDs can be replaced by sand columns or

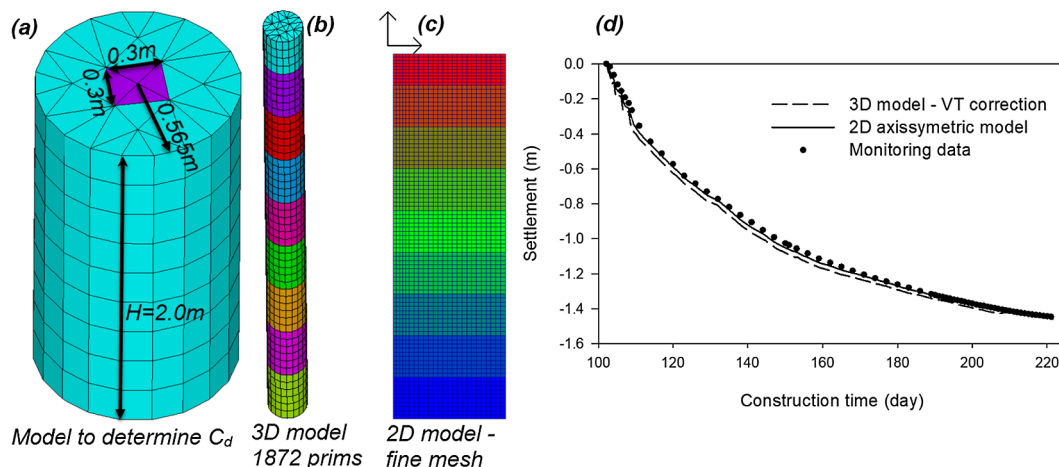


Fig. 10. (a) The simple unit cell model; (b) model-1: the full 3D unit model; (c) model-2: the 2D axisymmetric model – coarse mesh (the horizontal coordinate is exaggerated 10 times); (d) comparison among the 3D model, the 2D model and field data during the vacuum pumping period.

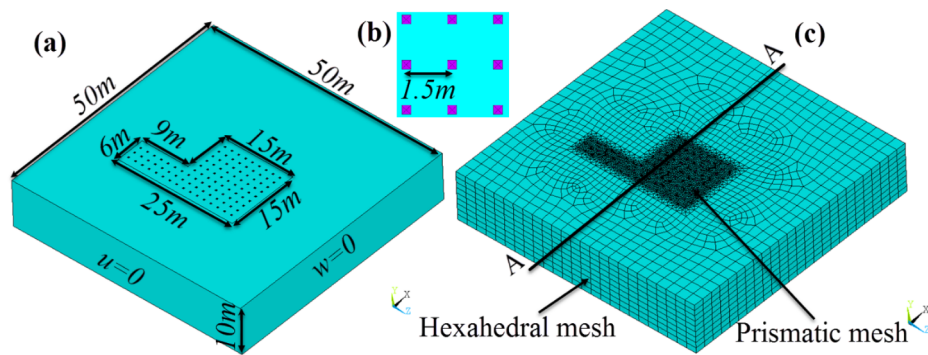


Fig. 11. The test case model; (a) Model dimensions; (b) the installation pattern of the PVDs; (c) 3D FE mesh.

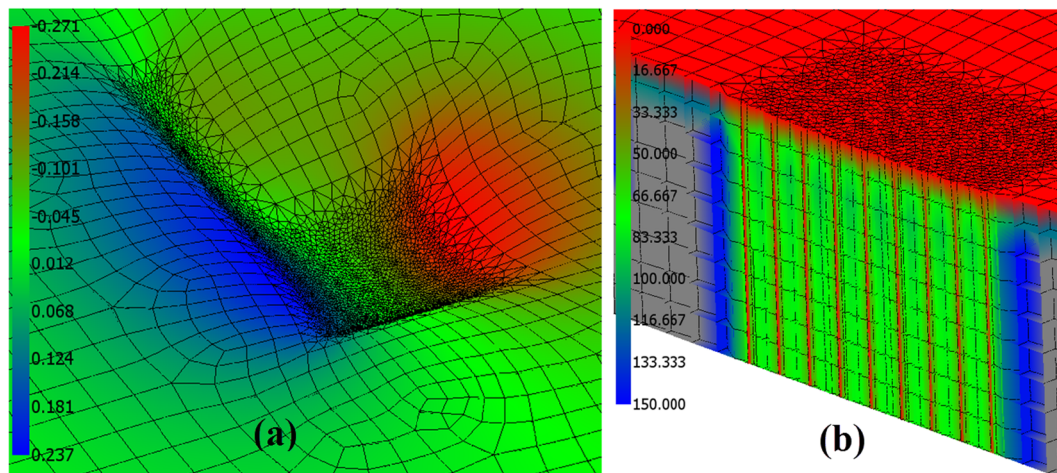


Fig. 12. The results after 100 days; (a) the horizontal deformation (five times exaggeration); (b) excess pore pressure (view A-A).

wells in land subsidence due to groundwater extraction models.

## 7. Conclusion

In conclusion, with a calculation domain with many PVDs, detailed steps to apply the Vimoke–Taylor concept for a fully coupled 3D model can be summarised as follows:

- **Step 1:** At the centre position of each PVD, creating a drained-zone block, which has the cross-section.
- **Step 2:** Meshing the drained-zone with prismatic elements or hexahedral elements.
- **Step 3:** Meshing the rest of the domain with any element type.
- **Step 4:** Modifying the horizontal hydraulic conductivity of the drained-zone with a correction factor  $C_d$ , or  $k_{hd} = C_d k_h$ .

The correction factor is determined for each specific case by the procedure described in Section 3.2. By minimising error between numerical results and analytical solutions of a simple unit cell with an optimising algorithm, the  $C_d$  factor is always found. Six patch tests were performed to study factors that can affect the correction factor. The results of the patch tests indicate that the  $C_d$  value depends mainly on three factors: the size of the drained-zone, the size of the PVD and the smear-zone and the mesh characteristic of the drained-zone. When one of these factors changes,  $C_d$  must be recalculated. Conversely,  $C_d$  is not affected by changes in the soil properties and the discharge capacity of the PVD.

The patch tests showed that applying the VT concept for 3D models of unit cells leads to the average error between numerical models and analytical solutions, which is less than 2%. For a real case study in

Section 5.1, the 3D model with the coarse mesh produced almost the same results obtained from the 2D axisymmetric model with the dense mesh. Results from the patch tests and the case study prove that the VT concept is the effective approach for 3D models of PVDs systems.

Additionally, open-source software was developed for determining the correction factor. All information about the software can be found on GitHub via [https://github.com/pham-hung/VimokeTaylor\\_PVDs](https://github.com/pham-hung/VimokeTaylor_PVDs).

## Acknowledgement

Hung Tien Pham is funded by NaWaM, a program of German Academic Exchange Service (DAAD).

## Appendix A. Supplementary material

Supplementary data to this article can be found online at <https://doi.org/10.1016/j.compgeo.2019.103201>.

## References

- [1] Barron RA. Consolidation of fine-grained soils by drain wells. *Trans Am Soc Civil Eng* 1948;113(1):718–42.
- [2] Hansbo S. Consolidation of fine-grained soils by prefabricated drains. In: Proceedings of the 10th international conference on soil mechanics and foundation engineering, Stockholm: AA Balkema Rotterdam, The Netherlands; 1981. p. 677–82.
- [3] Rujikiatkamjorn C, Indraratna B. Three-dimensional numerical modeling of soft soil consolidation improved by prefabricated vertical drains. *Ground Modification and Seismic Mitigation* 2006.
- [4] Rujikiatkamjorn C, Indraratna B, Chu J. 2D and 3D numerical modeling of combined surcharge and vacuum preloading with vertical drains. *Int J Geomech* 2008;8(2):144–56.
- [5] Wong J. Comparison of drainage line elements in PLAXIS 2D and 3D applied in

- consolidating marine clay deposits soft soil engineering international conference 2013 Kuching, Sarawak, Malaysia; 2013.
- [6] Fipps G, Skaggs R, Nieber J. Drains as a boundary condition in finite elements. *Water Resour Res* 1986;22(11):1613–21.
- [7] Vimoke B, Tyra T, Thiel T, Taylor G. Improvements in construction and use of resistance networks for studying drainage problems. *Soil Sci Soc Am J* 1962;26(2):203–7.
- [8] Heinen M. Correction of the Vimoke-Taylor Concept Representing Drains in a Numerical Simulation Model. *Vadose Zone J* 2014;13(10).
- [9] Long RP, Covo A. Equivalent diameter of vertical drains with an oblong cross section. *J Geotech Eng* 1994;120(9):1625–30.
- [10] Biot MA. General theory of three-dimensional consolidation. *J Appl Phys* 1941;12(2):155–64.
- [11] Biot MA. Theory of elasticity and consolidation for a porous anisotropic solid. *J Appl Phys* 1955;26(2):182–5.
- [12] Verruijt A. *PoroElasticity*: <http://geo.verruijt.net/>; 2016.
- [13] Rühaak W, Bense VF, Sass I. 3D hydro-mechanically coupled groundwater flow modelling of Pleistocene glaciation effects. *Comput Geosci* 2014;67:89–99.
- [14] Reed MB. An investigation of numerical errors in the analysis of consolidation by finite elements. *Int J Numer Anal Meth Geomech* 1984;8(3):243–57.
- [15] Wang WD, Wang JG, Wang ZL, Nogami T. An unequal-order radial interpolation meshless method for Biot's consolidation theory. *Comput Geotech* 2007;34(2):61–70.
- [16] Pham HT, Rühaak W, Schuster V, Sass I. Fully hydro-mechanical coupled Plug-in (SUB+) in FEFLOW for analysis of land subsidence due to groundwater extraction. *SoftwareX* 2019;9:15–9.
- [17] Kiefer J. Sequential minimax search for a maximum. *Proc Am Math Soc* 1953;4(3):502–6.
- [18] Hird CC, Pyrah IC, Russel D. Finite element modelling of vertical drains beneath embankments on soft ground. *Géotechnique* 1992;42(3):499–511.
- [19] D4186-89 AS. *Standard Test Method for One-dimensional Consolidation Properties of Saturated Cohesive Soils Using Controlled-strain Loading*. ASTM International, 1998.
- [20] Bergado DT, Asakami H, Alfaro MC, Balasubramaniam AS. Smear effects of vertical drains on soft Bangkok clay. *J Geotech Eng* 1991;117(10):1509–30.
- [21] Nguyen C-O, Tran TT. Consolidation analysis of Vietnam soft marine clay by finite difference method with application of constant rate of strain consolidation test. *Geotechnique, Constr Mater Environ Osaka, Japan* 2015:271–6.
- [22] Indraratna B, Sathananthan I, Rujikiatkamjorn C, Balasubramaniam AS. Analytical and numerical modeling of soft soil stabilized by prefabricated vertical drains incorporating vacuum preloading. *Int J Geomech* 2005;5(2):114–24.

---

## 6. Discussion and outlook

---

Chapter 3 presented the plug-in for FEFLOW to calculate land subsidence magnitude due to groundwater extraction based on Biot's theory. Currently, input parameters for models are constant; hence, further developments will consider nonlinear parameters (stress or void ratio dependent) that are more appropriate for shallow aquifers and shallow aquitards that have a low-stress level. Furthermore, to model earth fissure problems also originated from groundwater extraction, a plastic soil constitutive model needs to be added.

In this dissertation, Pardiso direct solver was used to solve the linear algebra system from Biot's coupled equations. Although this solver is preferable for Biot's theory because of the ill-conditioned stiffness matrix, it is not suitable for a large model that has millions of degree of freedom; as it requires a large amount of RAM to achieve the best efficiency. Therefore, an iterative solver should be considered in this case.

Chapter 4 proposed to use directly stress-dependent parameters obtained from the CRST. This approach is suitable for cases whose consolidation process is loading process (i.e. effective stress increases gradually). However, when an unloading process takes place, the unloading bulk modulus is usually larger than the loading bulk modulus. Hence, using only stress-dependent curves lead to an overestimation of deformations during the unloading process. A possible solution for this problem is to combine both the proposed approach and the traditional method, i.e. using the stress-dependent parameters for the loading process and using the recompression index  $C_r$  for the unloading process. Furthermore, although a soil failure criterion is not essential for unit cell models as soils deform only vertically, a failure criterion such as Mohr-Coulomb criterion must be used along with stress-dependent parameters for 2D and 3D models to capture realistic behaviours of soils.

Additionally, the back analysis scheme for the CRST assumes that all elements have the same properties (bulk modulus and hydraulic conductivity) at a given time during the test. However, for very soft soils such as slurry, the effective stress varies greatly from the top to the bottom of the soil sample. This leads to different values of the bulk modulus across the depth of the sample. Hence, another nonlinear back analysis scheme needs to be considered to handle this situation. The nonlinear CRST theory of Umehara (Umehara & Zen, 1980) will be a useful reference.

Also, in chapter 4, CONAXIS was developed with the main focuses on the CRST and unit cell models. It can be expanded to handle data from Rowe's cell (horizontal consolidation test) as there are many commons between the CRST and Rowe's cell test. To gain more popularity, other soil constitutive models such as the perfect elastoplastic model, the modified Cam-Clay model should be further included in CONAXIS. Therefore, users can have a choice and can compare results from different approaches.

Chapter 5 demonstrated the advantages of Vimoke–Taylor concept for 3D models of PVD systems. The procedure to determine the correction factor can be applied for other analyses that share the same difficulties with PVD systems. For instance, PVDs can be replaced with sand or stone columns, wells in land subsidence models in chapter 3 or borehole heat exchangers. Though the proposed approach was verified with analytical solutions and the unit cell model of the field project, it is desirable to validate the method with another real case that is similar to the second example in chapter 5.

---



---

## Appendix

---

### Appendix A: Stiffness matrices of 3D models

The matrix form of the coupled equation set is:

$$\begin{bmatrix} [A] & [B] & [C] & [D] \\ [B]^T & [F] & [G] & [H] \\ [C]^T & [I] & [J] & [S] \\ -[D]^T & -[H]^T & -[S]^T & [M] + \Delta t \times [P] \end{bmatrix} \begin{Bmatrix} \Delta u \\ \Delta v \\ \Delta w \\ \Delta p \end{Bmatrix} = \begin{Bmatrix} \Delta F_x \\ \Delta F_y \\ \Delta F_z \\ -\Delta t \times [P] \times p_0 + \Delta t \times Q \end{Bmatrix}$$

where:

$$[A] = \sum_1^{noe} [A_i] = \sum_1^{noe} \left[ \left( K + \frac{4}{3} G \right) \iiint_V \frac{\partial N_d^T}{\partial x} \frac{\partial N}{\partial x} dV + G \iiint_V \frac{\partial N_d^T}{\partial y} \frac{\partial N}{\partial y} dV + G \iiint_V \frac{\partial N_d^T}{\partial z} \frac{\partial N}{\partial z} dV \right]$$

$$[B] = \sum_1^{noe} [B_i] = \sum_1^{noe} \left[ \left( K - \frac{2}{3} G \right) \iiint_V \frac{\partial N_d^T}{\partial x} \frac{\partial N}{\partial y} dV + G \iiint_V \frac{\partial N_d^T}{\partial y} \frac{\partial N}{\partial x} dV \right]$$

$$[C] = \sum_1^{noe} [C_i] = \sum_1^{noe} \left[ \left( K - \frac{2}{3} G \right) \iiint_V \frac{\partial N_d^T}{\partial x} \frac{\partial N}{\partial z} dV + G \iiint_V \frac{\partial N_d^T}{\partial z} \frac{\partial N}{\partial x} dV \right]$$

$$[D] = \sum_1^{noe} [D_i] = \sum_1^{noe} \left[ -\alpha \iiint_V \frac{\partial N_d^T}{\partial x} N_p dV \right]$$

$$[F] = \sum_1^{noe} [F_i] = \sum_1^{noe} \left[ \left( K + \frac{4}{3} G \right) \iiint_V \frac{\partial N_d^T}{\partial y} \frac{\partial N}{\partial y} dV + G \iiint_V \frac{\partial N_d^T}{\partial x} \frac{\partial N}{\partial x} dV + G \iiint_V \frac{\partial N_d^T}{\partial z} \frac{\partial N}{\partial z} dV \right]$$

$$[G] = \sum_1^{noe} [G_i] = \sum_1^{noe} \left[ \left( K - \frac{2}{3} G \right) \iiint_V \frac{\partial N_d^T}{\partial y} \frac{\partial N}{\partial z} dV + G \iiint_V \frac{\partial N_d^T}{\partial z} \frac{\partial N}{\partial y} dV \right]$$

$$[H] = \sum_1^{noe} [H_i] = \sum_1^{noe} \left[ -\alpha \iiint_V \frac{\partial N_d^T}{\partial y} N_p dV \right]$$

$$[I] = \sum_1^{noe} [I_i] = \sum_1^{noe} \left[ \left( K - \frac{2}{3} G \right) \iiint_V \frac{\partial N_d^T}{\partial z} \frac{\partial N}{\partial x} dV + G \iiint_V \frac{\partial N_d^T}{\partial x} \frac{\partial N}{\partial z} dV \right]$$

$$[J] = \sum_1^{noe} [J_i] = \sum_1^{noe} \left[ \left( K + \frac{4}{3} G \right) \iiint_V \frac{\partial N_d^T}{\partial z} \frac{\partial N}{\partial z} dV + G \iiint_V \frac{\partial N_d^T}{\partial x} \frac{\partial N}{\partial x} dV + G \iiint_V \frac{\partial N_d^T}{\partial y} \frac{\partial N}{\partial y} dV \right]$$

$$[K] = \sum_1^{noe} [K_i] = \sum_1^{noe} \left[ -\alpha \iiint_V \frac{\partial N_d^T}{\partial z} N_p dV \right]$$

$$[M] = \sum_1^{noe} [M_i] = \sum_1^{noe} S \iiint_{dV} N_p^T N_p dV$$

---

$$[P] = \sum_1^{noe} [P_i] = \sum_1^{noe} \left[ \frac{k_x}{\gamma_f} \iiint \frac{\partial N_p^T}{\partial x} \frac{\partial N_p}{\partial x} dV + \frac{k_y}{\gamma_f} \iiint \frac{\partial N_p^T}{\partial y} \frac{\partial N_p}{\partial y} dV + \frac{k_z}{\gamma_f} \iiint \frac{\partial N_p^T}{\partial z} \frac{\partial N_p}{\partial z} dV \right]$$

## Appendix B: Stiffness matrices of axisymmetric models

The matrix form of the coupled equation set is:

$$\begin{bmatrix} [A] & [B] & [C] \\ [B]^T & [D] & [E] \\ -[C]^T & -[E]^T & [M] + \Delta t \times [P] \end{bmatrix} \begin{Bmatrix} \Delta u \\ \Delta v \\ \Delta p \end{Bmatrix} = \begin{Bmatrix} \Delta F_r \\ \Delta F_z \\ -\Delta t \times [P] \times p_0 + \Delta t \times Q \end{Bmatrix}$$

where:

$$\begin{aligned} [A] &= \sum_1^{noe} [A_i] \\ &= \sum_1^{noe} \left[ \left( K + \frac{4}{3} G \right) \iint_R \left( \frac{\partial N_d^T}{\partial r} \frac{\partial N_d}{\partial r} + \frac{N_d^T}{r} \frac{N_d}{r} \right) rdR + \left( K - \frac{2}{3} G \right) \iint_R \left( \frac{\partial N_d^T}{\partial r} \frac{N_d}{r} + \frac{N_d^T}{r} \frac{\partial N_d}{\partial r} \right) rdR + G \iint_R \left( \frac{\partial N_d^T}{\partial z} \frac{\partial N_d}{z} \right) rdR \right] \end{aligned}$$

$$[B] = \sum_1^{noe} [B_i] = \sum_1^{noe} \left[ \left( K - \frac{2G}{3} \right) \iint_R \left( \frac{\partial N_d^T}{\partial r} \frac{\partial N_d}{\partial z} + \frac{N_d^T}{r} \frac{\partial N_d}{\partial z} \right) rdR + G \iint_R \left( \frac{\partial N_d^T}{\partial z} \frac{\partial N_d}{\partial r} \right) rdR \right]$$

$$[C] = \sum_1^{noe} [C_i] = \sum_1^{noe} \left[ -\alpha \iint_R \left( \frac{\partial N_d^T}{\partial r} N_p + \frac{N_d^T}{r} N_p \right) rdR \right]$$

$$\begin{aligned} [D] &= \sum_1^{noe} [D_i] \\ &= \sum_1^{noe} \left[ \left( K + \frac{4}{3} G \right) \iint_R \left( \frac{\partial N_d^T}{\partial z} \frac{\partial N_d}{\partial z} \right) rdR + G \iint_R \left( \frac{\partial N_d^T}{\partial r} \frac{\partial N_d}{r} \right) rdR \right] \end{aligned}$$

$$[E] = \sum_1^{noe} [E_i] = \sum_1^{noe} \left[ -\alpha \iint_R \left( \frac{\partial N_d^T}{\partial z} N_p \right) rdR \right]$$

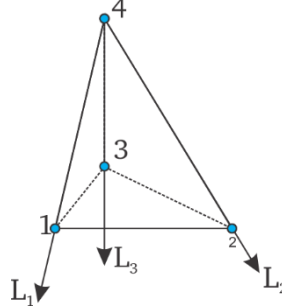
$$[M] = \sum_1^{noe} [M_i] = \sum_1^{noe} S \iint_R N_p^T N_p rdR$$

$$[P] = \sum_1^{noe} [P_i] = \sum_1^{noe} \left[ \frac{k_r}{\gamma_f} \iint_R \frac{\partial N_p^T}{\partial r} \frac{\partial N_p}{\partial r} rdR + \frac{k_z}{\gamma_f} \iint_R \frac{\partial N_p^T}{\partial z} \frac{\partial N_p}{\partial z} rdR \right]$$

## Appendix C: Shape functions and their derivations

The mix element approach with second-order elements for the displacement field and first-order elements for the pressure field was used in this dissertation.

### C.1. Tetrahedron 4 nodes (Tet4)



Tetrahedron 4 nodes – local coordinate (  $L_1, L_2, L_3$  )

Shape function:

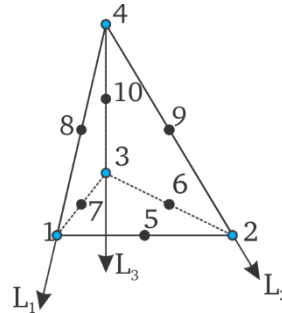
$$N = [N_1 \quad N_2 \quad N_3 \quad N_4]$$

$$N_1 = L_1; N_2 = L_2; N_3 = L_3; N_4 = 1 - L_1 - L_2 - L_3$$

Derivations:

$$\frac{\partial N}{\partial L_1} = [1 \quad 0 \quad 0 \quad -1]; \quad \frac{\partial N}{\partial L_2} = [0 \quad 1 \quad 0 \quad -1]; \quad \frac{\partial N}{\partial L_3} = [0 \quad 0 \quad 1 \quad -1]$$

### C.2. Tetrahedron 10 nodes (Tet10)



Tetrahedron 10 nodes – local coordinate (  $L_1, L_2, L_3$  )

Shape function:

$$N_1 = (2L_1 - 1)L_1; N_2 = (2L_2 - 1)L_2; N_3 = (2L_3 - 1)L_3; N_4 = (2L_4 - 1)L_4; L_4 = 1 - L_1 - L_2 - L_3$$

$$N_5 = 4L_1L_2; N_6 = 4L_2L_3; N_7 = 4L_1L_3; N_8 = 4L_1L_4; N_9 = 4L_2L_4; N_{10} = 4L_3L_4$$

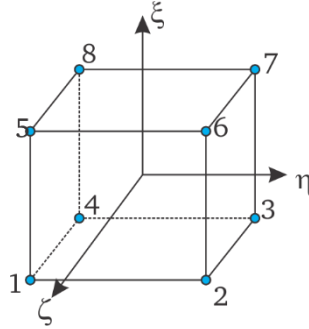
Derivations:

$$\frac{\partial N}{\partial L_1} = [4L_1 - 1 \quad 0 \quad 0 \quad 1 - 4L_4 \quad 4L_2 \quad 0 \quad 4L_3 \quad 4(L_4 - L_1) \quad -4L_2 \quad -4L_3]$$

$$\frac{\partial N}{\partial L_2} = [0 \quad 4L_2 - 1 \quad 0 \quad 1 - 4L_4 \quad 4L_1 \quad 4L_3 \quad 0 \quad -4L_1 \quad 4(L_4 - L_2) \quad -4L_3]$$

$$\frac{\partial N}{\partial L_3} = [0 \quad 0 \quad 4L_3 - 1 \quad 1 - 4L_4 \quad 0 \quad 4L_2 \quad 4L_1 \quad -4L_1 \quad -4L_2 \quad 4(L_4 - L_3)]$$

### C.3. Hexahedron 8 nodes (Hex8)



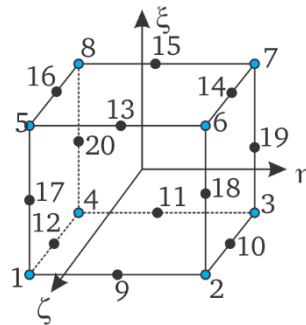
Hexahedron 8 nodes – local coordinate  $(\eta, \zeta, \xi)$

Shape function and derivations:

$N_1 = \frac{1}{8}(1-\xi)(1-\eta)(1-\zeta)$	$\frac{\partial N_1}{\partial \xi} = -\frac{1}{8}(1-\eta)(1-\zeta)$
$N_2 = \frac{1}{8}(1-\xi)(1-\eta)(1+\zeta)$	$\frac{\partial N_2}{\partial \xi} = -\frac{1}{8}(1-\eta)(1+\zeta)$
$N_3 = \frac{1}{8}(1+\xi)(1-\eta)(1+\zeta)$	$\frac{\partial N_3}{\partial \xi} = \frac{1}{8}(1-\eta)(1+\zeta)$
$N_4 = \frac{1}{8}(1+\xi)(1-\eta)(1-\zeta)$	$\frac{\partial N_4}{\partial \xi} = \frac{1}{8}(1-\eta)(1-\zeta)$
$N_5 = \frac{1}{8}(1-\xi)(1+\eta)(1-\zeta)$	$\frac{\partial N_5}{\partial \xi} = -\frac{1}{8}(1+\eta)(1-\zeta)$
$N_6 = \frac{1}{8}(1-\xi)(1+\eta)(1+\zeta)$	$\frac{\partial N_6}{\partial \xi} = -\frac{1}{8}(1+\eta)(1+\zeta)$
$N_7 = \frac{1}{8}(1+\xi)(1+\eta)(1+\zeta)$	$\frac{\partial N_7}{\partial \xi} = \frac{1}{8}(1+\eta)(1+\zeta)$
$N_8 = \frac{1}{8}(1+\xi)(1+\eta)(1-\zeta)$	$\frac{\partial N_8}{\partial \xi} = \frac{1}{8}(1+\eta)(1-\zeta)$

$$\begin{aligned} \frac{\partial N_1}{\partial \eta} &= -\frac{1}{8}(1-\xi)(1-\zeta) & \frac{\partial N_1}{\partial \zeta} &= -\frac{1}{8}(1-\xi)(1-\eta) \\ \frac{\partial N_2}{\partial \eta} &= -\frac{1}{8}(1-\xi)(1+\zeta) & \frac{\partial N_2}{\partial \zeta} &= \frac{1}{8}(1-\xi)(1-\eta) \\ \frac{\partial N_3}{\partial \eta} &= -\frac{1}{8}(1+\xi)(1+\zeta) & \frac{\partial N_3}{\partial \zeta} &= \frac{1}{8}(1+\xi)(1-\eta) \\ \frac{\partial N_4}{\partial \eta} &= -\frac{1}{8}(1+\xi)(1-\zeta) & \frac{\partial N_4}{\partial \zeta} &= -\frac{1}{8}(1+\xi)(1-\eta) \\ \frac{\partial N_5}{\partial \eta} &= \frac{1}{8}(1-\xi)(1-\zeta) & \frac{\partial N_5}{\partial \zeta} &= -\frac{1}{8}(1-\xi)(1+\eta) \\ \frac{\partial N_6}{\partial \eta} &= \frac{1}{8}(1-\xi)(1+\zeta) & \frac{\partial N_6}{\partial \zeta} &= \frac{1}{8}(1-\xi)(1+\eta) \\ \frac{\partial N_7}{\partial \eta} &= \frac{1}{8}(1+\xi)(1+\zeta) & \frac{\partial N_7}{\partial \zeta} &= \frac{1}{8}(1+\xi)(1+\eta) \\ \frac{\partial N_8}{\partial \eta} &= \frac{1}{8}(1+\xi)(1-\zeta) & \frac{\partial N_8}{\partial \zeta} &= -\frac{1}{8}(1+\xi)(1+\eta) \end{aligned}$$

#### C.4. Hexahedron 20 nodes (Hex20)



Hexahedron 20 nodes - local coordinate (  $\eta, \zeta, \xi$  )

Shape function:

$$\begin{aligned}
N_1 &= \frac{1}{8}(1-\xi)(1-\eta)(1-\zeta)(-\xi-\eta-\zeta-2) \\
N_2 &= \frac{1}{8}(1-\xi)(1-\eta)(1+\zeta)(-\xi-\eta+\zeta-2) \\
N_3 &= \frac{1}{8}(1+\xi)(1-\eta)(1+\zeta)(\xi-\eta+\zeta-2) \\
N_4 &= \frac{1}{8}(1+\xi)(1-\eta)(1-\zeta)(\xi-\eta-\zeta-2) \\
N_5 &= \frac{1}{8}(1-\xi)(1+\eta)(1-\zeta)(-\xi+\eta-\zeta-2) \\
N_6 &= \frac{1}{8}(1-\xi)(1+\eta)(1+\zeta)(-\xi+\eta+\zeta-2) \\
N_7 &= \frac{1}{8}(1+\xi)(1+\eta)(1+\zeta)(\xi+\eta+\zeta-2) \\
N_8 &= \frac{1}{8}(1+\xi)(1+\eta)(1-\zeta)(\xi+\eta-\zeta-2) \\
N_9 &= \frac{1}{4}(1-\xi)(1-\eta)(1-\zeta^2) \\
N_{10} &= \frac{1}{4}(1-\xi^2)(1-\eta)(1+\zeta) \\
N_{11} &= \frac{1}{4}(1+\xi)(1-\eta)(1-\zeta^2) \\
N_{12} &= \frac{1}{4}(1-\xi^2)(1-\eta)(1-\zeta) \\
N_{13} &= \frac{1}{4}(1-\xi)(1+\eta)(1-\zeta^2) \\
N_{14} &= \frac{1}{4}(1-\xi^2)(1+\eta)(1+\zeta) \\
N_{15} &= \frac{1}{4}(1+\xi)(1+\eta)(1-\zeta^2) \\
N_{16} &= \frac{1}{4}(1-\xi^2)(1+\eta)(1-\zeta) \\
N_{17} &= \frac{1}{4}(1-\xi)(1-\eta^2)(1-\zeta) \\
N_{18} &= \frac{1}{4}(1-\xi)(1-\eta^2)(1+\zeta) \\
N_{19} &= \frac{1}{4}(1+\xi)(1-\eta^2)(1+\zeta) \\
N_{20} &= \frac{1}{4}(1+\xi)(1-\eta^2)(1-\zeta)
\end{aligned}$$

---

Derivations:

$$\frac{\partial N_1}{\partial \xi} = \frac{1}{8}(1-\eta)(1-\zeta)[-1(-\xi-\eta-\zeta-2)-1(1-\xi)]$$

$$\frac{\partial N_2}{\partial \xi} = \frac{1}{8}(1-\eta)(1+\zeta)[-1(-\xi-\eta+\zeta-2)-1(1-\xi)]$$

$$\frac{\partial N_3}{\partial \xi} = \frac{1}{8}(1-\eta)(1+\zeta)[+1(+\xi-\eta+\zeta-2)+1(1+\xi)]$$

$$\frac{\partial N_4}{\partial \xi} = \frac{1}{8}(1-\eta)(1-\zeta)[+1(+\xi-\eta-\zeta-2)+1(1+\xi)]$$

$$\frac{\partial N_5}{\partial \xi} = \frac{1}{8}(1+\eta)(1-\zeta)[-1(-\xi+\eta-\zeta-2)-1(1-\xi)]$$

$$\frac{\partial N_6}{\partial \xi} = \frac{1}{8}(1+\eta)(1+\zeta)[-1(-\xi+\eta+\zeta-2)-1(1-\xi)]$$

$$\frac{\partial N_7}{\partial \xi} = \frac{1}{8}(1+\eta)(1+\zeta)[+1(+\xi+\eta+\zeta-2)+1(1+\xi)]$$

$$\frac{\partial N_8}{\partial \xi} = \frac{1}{8}(1+\eta)(1-\zeta)[+1(+\xi+\eta-\zeta-2)+1(1+\xi)]$$

$$\frac{\partial N_9}{\partial \xi} = -\frac{1}{4}(1-\eta)(1-\zeta^2)$$

$$\frac{\partial N_{10}}{\partial \xi} = -\frac{\xi}{2}(1-\eta)(1+\zeta)$$

$$\frac{\partial N_{11}}{\partial \xi} = \frac{1}{4}(1-\eta)(1-\zeta^2)$$

$$\frac{\partial N_{12}}{\partial \xi} = -\frac{\xi}{2}(1-\eta)(1-\zeta)$$

$$\frac{\partial N_{13}}{\partial \xi} = -\frac{1}{4}(1+\eta)(1-\zeta^2)$$

$$\frac{\partial N_{14}}{\partial \xi} = -\frac{\xi}{2}(1+\eta)(1+\zeta)$$

$$\frac{\partial N_{15}}{\partial \xi} = \frac{1}{4}(1+\eta)(1-\zeta^2)$$

$$\frac{\partial N_{16}}{\partial \xi} = -\frac{\xi}{2}(1+\eta)(1-\zeta)$$

$$\frac{\partial N_{17}}{\partial \xi} = -\frac{1}{4}(1-\eta^2)(1-\zeta)$$

$$\frac{\partial N_{18}}{\partial \xi} = -\frac{1}{4}(1-\eta^2)(1+\zeta)$$

$$\frac{\partial N_{19}}{\partial \xi} = \frac{1}{4}(1-\eta^2)(1+\zeta)$$

$$\frac{\partial N_{20}}{\partial \xi} = \frac{1}{4}(1-\eta^2)(1-\zeta)$$

---

$$\frac{\partial N_1}{\partial \eta} = \frac{1}{8}(1-\xi)(1-\zeta)[-1(-\xi-\eta-\zeta-2)-1(1-\eta)]$$

$$\frac{\partial N_2}{\partial \eta} = \frac{1}{8}(1-\xi)(1+\zeta)[-1(-\xi-\eta+\zeta-2)-1(1-\eta)]$$

$$\frac{\partial N_3}{\partial \eta} = \frac{1}{8}(1+\xi)(1+\zeta)[-1(\xi-\eta+\zeta-2)-1(1-\eta)]$$

$$\frac{\partial N_4}{\partial \eta} = \frac{1}{8}(1+\xi)(1-\zeta)[-1(\xi-\eta-\zeta-2)-1(1-\eta)]$$

$$\frac{\partial N_5}{\partial \eta} = \frac{1}{8}(1-\xi)(1-\zeta)[1(-\xi+\eta-\zeta-2)+1(1+\eta)]$$

$$\frac{\partial N_6}{\partial \eta} = \frac{1}{8}(1-\xi)(1+\zeta)[1(-\xi+\eta+\zeta-2)+1(1+\eta)]$$

$$\frac{\partial N_7}{\partial \eta} = \frac{1}{8}(1+\xi)(1+\zeta)[1(\xi+\eta+\zeta-2)+1(1+\eta)]$$

$$\frac{\partial N_8}{\partial \eta} = \frac{1}{8}(1+\xi)(1-\zeta)[1(\xi+\eta-\zeta-2)+1(1+\eta)]$$

$$\frac{\partial N_9}{\partial \eta} = -\frac{1}{4}(1-\xi)(1-\zeta^2)$$

$$\frac{\partial N_{10}}{\partial \eta} = -\frac{1}{4}(1-\xi^2)(1+\zeta)$$

$$\frac{\partial N_{11}}{\partial \eta} = -\frac{1}{4}(1+\xi)(1-\zeta^2)$$

$$\frac{\partial N_{12}}{\partial \eta} = -\frac{1}{4}(1-\xi^2)(1-\zeta)$$

$$\frac{\partial N_{13}}{\partial \eta} = \frac{1}{4}(1-\xi)(1-\zeta^2)$$

$$\frac{\partial N_{14}}{\partial \eta} = \frac{1}{4}(1-\xi^2)(1+\zeta)$$

$$\frac{\partial N_{15}}{\partial \eta} = \frac{1}{4}(1+\xi)(1-\zeta^2)$$

$$\frac{\partial N_{16}}{\partial \eta} = \frac{1}{4}(1-\xi^2)(1-\zeta)$$

$$\frac{\partial N_{17}}{\partial \eta} = -\frac{\eta}{2}(1-\xi)(1-\zeta)$$

$$\frac{\partial N_{18}}{\partial \eta} = -\frac{\eta}{2}(1-\xi)(1+\zeta)$$

$$\frac{\partial N_{19}}{\partial \eta} = -\frac{\eta}{2}(1+\xi)(1+\zeta)$$

$$\frac{\partial N_{20}}{\partial \eta} = -\frac{\eta}{2}(1+\xi)(1-\zeta)$$

$$\frac{\partial N_1}{\partial \zeta} = \frac{1}{8}(1-\xi)(1-\eta)[-1(-\xi-\eta-\zeta-2)-1(1-\zeta)]$$

$$\frac{\partial N_2}{\partial \zeta} = \frac{1}{8}(1-\xi)(1-\eta)[1(-\xi-\eta+\zeta-2)+1(1+\zeta)]$$

$$\frac{\partial N_3}{\partial \zeta} = \frac{1}{8}(1+\xi)(1-\eta)[1(\xi-\eta+\zeta-2)+1(1+\zeta)]$$

$$\frac{\partial N_4}{\partial \zeta} = \frac{1}{8}(1+\xi)(1-\eta)[-1(\xi-\eta-\zeta-2)-1(1-\zeta)]$$

$$\frac{\partial N_5}{\partial \zeta} = \frac{1}{8}(1-\xi)(1+\eta)[-1(-\xi+\eta-\zeta-2)-1(1-\zeta)]$$

$$\frac{\partial N_6}{\partial \zeta} = \frac{1}{8}(1-\xi)(1+\eta)[1(-\xi+\eta+\zeta-2)+1(1+\zeta)]$$

$$\frac{\partial N_7}{\partial \zeta} = \frac{1}{8}(1+\xi)(1+\eta)[1(\xi+\eta+\zeta-2)+1(1+\zeta)]$$

$$\frac{\partial N_8}{\partial \zeta} = \frac{1}{8}(1+\xi)(1+\eta)[-1(\xi+\eta-\zeta-2)-1(1-\zeta)]$$

$$\frac{\partial N_9}{\partial \zeta} = -\frac{\zeta}{2}(1-\xi)(1-\eta)$$

$$\frac{\partial N_{10}}{\partial \zeta} = \frac{1}{4}(1-\xi^2)(1-\eta)$$

$$\frac{\partial N_{11}}{\partial \zeta} = -\frac{\zeta}{2}(1+\xi)(1-\eta)$$

$$\frac{\partial N_{12}}{\partial \zeta} = -\frac{1}{4}(1-\xi^2)(1-\eta)$$

$$\frac{\partial N_{13}}{\partial \zeta} = -\frac{\zeta}{2}(1-\xi)(1+\eta)$$

$$\frac{\partial N_{14}}{\partial \zeta} = \frac{1}{4}(1-\xi^2)(1+\eta)$$

$$\frac{\partial N_{15}}{\partial \zeta} = -\frac{\zeta}{2}(1+\xi)(1+\eta)$$

$$\frac{\partial N_{16}}{\partial \zeta} = -\frac{1}{4}(1-\xi^2)(1+\eta)$$

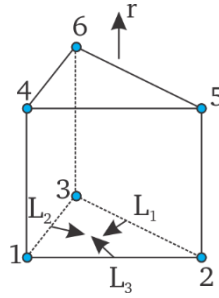
$$\frac{\partial N_{17}}{\partial \zeta} = -\frac{1}{4}(1-\xi)(1-\eta^2)$$

$$\frac{\partial N_{18}}{\partial \zeta} = \frac{1}{4}(1-\xi)(1-\eta^2)$$

$$\frac{\partial N_{19}}{\partial \zeta} = \frac{1}{4}(1+\xi)(1-\eta^2)$$

$$\frac{\partial N_{20}}{\partial \zeta} = -\frac{1}{4}(1+\xi)(1-\eta^2)$$

### C.5. Prism 6 nodes (Prism6)

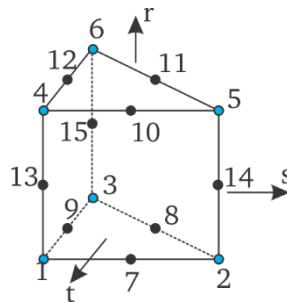


Prism 6 nodes – local coordinate  $(r, L_1, L_2)$

Shape function and derivations with  $L_3 = 1 - L_1 - L_2$  :

$N_1 = \frac{1}{2}L_1(1-r)$	$\frac{\partial N_1}{\partial L_1} = \frac{1}{2}(1-r)$	$\frac{\partial N_1}{\partial L_2} = 0$	$\frac{\partial N_1}{\partial r} = -\frac{1}{2}L_1$
$N_2 = \frac{1}{2}L_2(1-r)$	$\frac{\partial N_2}{\partial L_1} = 0$	$\frac{\partial N_2}{\partial L_2} = \frac{1}{2}(1-r)$	$\frac{\partial N_2}{\partial r} = -\frac{1}{2}L_2$
$N_3 = \frac{1}{2}L_3(1-r)$	$\frac{\partial N_3}{\partial L_1} = -\frac{1}{2}(1-r)$	$\frac{\partial N_3}{\partial L_2} = -\frac{1}{2}(1-r)$	$\frac{\partial N_3}{\partial r} = -\frac{1}{2}L_3$
$N_4 = \frac{1}{2}L_1(1+r)$	$\frac{\partial N_4}{\partial L_1} = \frac{1}{2}(1+r)$	$\frac{\partial N_4}{\partial L_2} = 0$	$\frac{\partial N_4}{\partial r} = \frac{1}{2}L_1$
$N_5 = \frac{1}{2}L_2(1+r)$	$\frac{\partial N_5}{\partial L_1} = 0$	$\frac{\partial N_5}{\partial L_2} = \frac{1}{2}(1+r)$	$\frac{\partial N_5}{\partial r} = \frac{1}{2}L_2$
$N_6 = \frac{1}{2}L_3(1+r)$	$\frac{\partial N_6}{\partial L_1} = -\frac{1}{2}(1+r)$	$\frac{\partial N_6}{\partial L_2} = -\frac{1}{2}(1+r)$	$\frac{\partial N_6}{\partial r} = \frac{1}{2}L_3$

### C.6. Prism 15 nodes (Prims15)



Prism 15 nodes – local coordinate  $(r, L_1, L_2)$

Shape function with  $L_3 = 1 - L_1 - L_2$  :

$$N_1 = \frac{1}{2} [L_1 (2L_1 - 1)(1-r) - L_1 (1-r^2)]$$

$$N_2 = \frac{1}{2} [L_2 (2L_2 - 1)(1-r) - L_2 (1-r^2)]$$

$$N_3 = \frac{1}{2} [L_3 (2L_3 - 1)(1-r) - L_3 (1-r^2)]$$

$$N_4 = \frac{1}{2} [L_1 (2L_1 - 1)(1+r) - L_1 (1-r^2)]$$

$$N_5 = \frac{1}{2} [L_2 (2L_2 - 1)(1+r) - L_2 (1-r^2)]$$

$$N_6 = \frac{1}{2} [L_3 (2L_3 - 1)(1+r) - L_3 (1-r^2)]$$

$$N_7 = 2L_1 L_2 (1-r)$$

$$N_8 = 2L_2 L_3 (1-r)$$

$$N_9 = 2L_3 L_1 (1-r)$$

$$N_{10} = 2L_1 L_2 (1+r)$$

$$N_{11} = 2L_2 L_3 (1+r)$$

$$N_{12} = 2L_3 L_1 (1+r)$$

$$N_{13} = L_1 (1-r^2)$$

$$N_{14} = L_2 (1-r^2)$$

$$N_{15} = L_3 (1-r^2)$$

$$\frac{\partial N_1}{\partial L_1} = \frac{1}{2} [(4L_1 - 1)(1-r) - (1-r^2)]$$

$$\frac{\partial N_2}{\partial L_1} = 0$$

$$\frac{\partial N_3}{\partial L_1} = \frac{1}{2} [(4L_1 + 4L_2 - 3)(1-r) + (1-r^2)]$$

$$\frac{\partial N_4}{\partial L_1} = \frac{1}{2} [(4L_1 - 1)(1+r) - (1-r^2)]$$

$$\frac{\partial N_5}{\partial L_1} = 0$$

$$\frac{\partial N_6}{\partial L_1} = \frac{1}{2} [(4L_1 + 4L_2 - 3)(1+r) + (1-r^2)]$$

$$\frac{\partial N_7}{\partial L_1} = 2L_2 (1-r)$$

$$\frac{\partial N_8}{\partial L_1} = -2L_2 (1-r)$$

$$\frac{\partial N_9}{\partial L_1} = 2(1 - 2L_1 - L_2)(1-r)$$

$$\frac{\partial N_{10}}{\partial L_1} = 2L_2 (1+r)$$

$$\frac{\partial N_{11}}{\partial L_1} = -2L_2 (1+r)$$

$$\frac{\partial N_{12}}{\partial L_1} = 2(1 - 2L_1 - L_2)(1+r)$$

$$\frac{\partial N_{13}}{\partial L_1} = (1-r^2)$$

$$\frac{\partial N_{14}}{\partial L_1} = (1-r^2)$$

$$\frac{\partial N_{15}}{\partial L_1} = -(1-r^2)$$

$$\frac{\partial N_1}{\partial L_2} = 0$$

$$\frac{\partial N_2}{\partial L_2} = \frac{1}{2}[(4L_2 - 1)(1-r) - (1-r^2)]$$

$$\frac{\partial N_3}{\partial L_2} = \frac{1}{2}[(4L_2 + 4L_1 - 3)(1-r) + (1-r^2)]$$

$$\frac{\partial N_4}{\partial L_2} = 0$$

$$\frac{\partial N_5}{\partial L_2} = \frac{1}{2}[(4L_2 - 1)(1+r) - (1-r^2)]$$

$$\frac{\partial N_6}{\partial L_2} = \frac{1}{2}[(4L_2 + 4L_1 - 3)(1+r) + (1-r^2)]$$

$$\frac{\partial N_7}{\partial L_2} = 2L_1(1-r)$$

$$\frac{\partial N_8}{\partial L_2} = 2(1-L_1-2L_2)(1-r)$$

$$\frac{\partial N_9}{\partial L_2} = -2L_1(1-r)$$

$$\frac{\partial N_{10}}{\partial L_2} = 2L_1(1+r)$$

$$\frac{\partial N_{11}}{\partial L_2} = 2(1-L_1-2L_2)(1+r)$$

$$\frac{\partial N_{12}}{\partial L_2} = -2L_1(1+r)$$

$$\frac{\partial N_{13}}{\partial L_2} = 0$$

$$\frac{\partial N_{14}}{\partial L_2} = (1-r^2)$$

$$\frac{\partial N_{15}}{\partial L_2} = -(1-r^2)$$

$$\frac{\partial N_1}{\partial r} = \frac{1}{2}[-L_1(2L_1 - 1) + 2rL_1]$$

$$\frac{\partial N_2}{\partial r} = \frac{1}{2}[-L_2(2L_2 - 1) + 2rL_2]$$

$$\frac{\partial N_3}{\partial r} = \frac{1}{2}[-L_3(2L_3 - 1) + 2rL_3]$$

$$\frac{\partial N_4}{\partial r} = \frac{1}{2}[L_1(2L_1 - 1) + 2rL_1]$$

$$\frac{\partial N_5}{\partial r} = \frac{1}{2}[L_2(2L_2 - 1) + 2rL_2]$$

$$\frac{\partial N_6}{\partial r} = \frac{1}{2}[L_3(2L_3 - 1) + 2rL_3]$$

$$\frac{\partial N_7}{\partial r} = -2L_1L_2$$

$$\frac{\partial N_8}{\partial r} = -2L_2L_3$$

$$\frac{\partial N_9}{\partial r} = -2L_3L_1$$

$$\frac{\partial N_{10}}{\partial r} = 2L_1L_2$$

$$\frac{\partial N_{11}}{\partial r} = 2L_2L_3$$

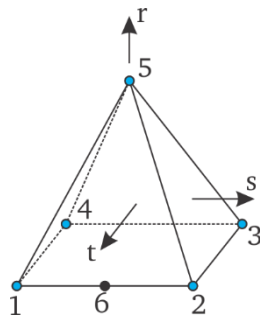
$$\frac{\partial N_{12}}{\partial r} = 2L_3L_1$$

$$\frac{\partial N_{13}}{\partial r} = -2rL_1$$

$$\frac{\partial N_{14}}{\partial r} = -2rL_2$$

$$\frac{\partial N_{15}}{\partial r} = -2rL_3$$

### C.7. Pyramid 5 nodes (Pyra6)



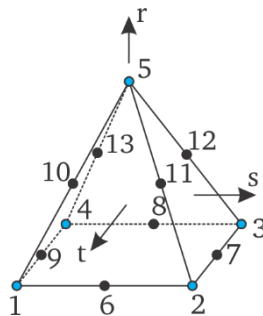
Pyramid 5 nodes - local coordinate  $(r, t, s)$

Shape function and derivations:

$$\begin{aligned}
 N_1 &= \frac{1}{8}(1-s)(1-t)(1-r) & \frac{\partial N_1}{\partial s} &= -\frac{1}{8}(1-t)(1-r) \\
 N_2 &= \frac{1}{8}(1+s)(1-t)(1-r) & \frac{\partial N_2}{\partial s} &= +\frac{1}{8}(1-t)(1-r) \\
 N_3 &= \frac{1}{8}(1+s)(1+t)(1-r) & \frac{\partial N_3}{\partial s} &= +\frac{1}{8}(1+t)(1-r) \\
 N_4 &= \frac{1}{8}(1-s)(1+t)(1-r) & \frac{\partial N_4}{\partial s} &= -\frac{1}{8}(1+t)(1-r) \\
 N_5 &= \frac{1}{2}(1+r) & \frac{\partial N_5}{\partial s} &= 0
 \end{aligned}$$

$$\begin{aligned}
 \frac{\partial N_1}{\partial t} &= -\frac{1}{8}(1-s)(1-r) & \frac{\partial N_1}{\partial r} &= -\frac{1}{8}(1-s)(1-t) \\
 \frac{\partial N_2}{\partial t} &= -\frac{1}{8}(1+s)(1-r) & \frac{\partial N_2}{\partial r} &= -\frac{1}{8}(1+s)(1-t) \\
 \frac{\partial N_3}{\partial t} &= +\frac{1}{8}(1+s)(1-r) & \frac{\partial N_3}{\partial r} &= -\frac{1}{8}(1+s)(1+t) \\
 \frac{\partial N_4}{\partial t} &= +\frac{1}{8}(1-s)(1-r) & \frac{\partial N_4}{\partial r} &= -\frac{1}{8}(1-s)(1+t) \\
 \frac{\partial N_5}{\partial t} &= 0 & \frac{\partial N_5}{\partial r} &= \frac{1}{2}
 \end{aligned}$$

### C.8. Pyramid 13 nodes (Pyra13)



Pyramid 13 nodes – local coordinate  $(r, t, s)$

Shape function and derivations:

---

$$N_1 = \frac{1}{16}(1-s)(1-t)(1-r)(-2-s+sr-t+tr)$$

$$N_2 = \frac{1}{16}(1+s)(1-t)(1-r)(-2+s-sr-t+tr)$$

$$N_3 = \frac{1}{16}(1+s)(1+t)(1-r)(-2+s-sr+t-tr)$$

$$N_4 = \frac{1}{16}(1-s)(1+t)(1-r)(-2-s+sr+t-tr)$$

$$N_5 = \frac{1}{2}r(1+r)$$

$$N_6 = \frac{1}{8}(1-s^2)(1-t)(1-2r+r^2)$$

$$N_7 = \frac{1}{8}(1+s)(1-t^2)(1-2r+r^2)$$

$$N_8 = \frac{1}{8}(1-s^2)(1+t)(1-2r+r^2)$$

$$N_9 = \frac{1}{8}(1-s)(1-t^2)(1-2r+r^2)$$

$$N_{10} = \frac{1}{4}(1-s-t+st)(1-r^2)$$

$$N_{11} = \frac{1}{4}(1+s-t-st)(1-r^2)$$

$$N_{12} = \frac{1}{4}(1+s+t+st)(1-r^2)$$

$$N_{13} = \frac{1}{4}(1-s+t-st)(1-r^2)$$

$$\frac{\partial N_1}{\partial s} = \frac{1}{16}(1-s)(1-t)(1-r)(-2-s+sr-t+tr)$$

$$\frac{\partial N_2}{\partial s} = \frac{1}{16}(1+s)(1-t)(1-r)(-2+s-sr-t+tr)$$

$$\frac{\partial N_3}{\partial s} = \frac{1}{16}(1+s)(1+t)(1-r)(-2+s-sr+t-tr)$$

$$\frac{\partial N_4}{\partial s} = \frac{1}{16}(1-s)(1+t)(1-r)(-2-s+sr+t-tr)$$

$$\frac{\partial N_5}{\partial s} = \frac{1}{2}r(1+r)$$

$$\frac{\partial N_6}{\partial s} = \frac{1}{8}(1-s^2)(1-t)(1-2r+r^2)$$

$$\frac{\partial N_7}{\partial s} = \frac{1}{8}(1+s)(1-t^2)(1-2r+r^2)$$

$$\frac{\partial N_8}{\partial s} = \frac{1}{8}(1-s^2)(1+t)(1-2r+r^2)$$

$$\frac{\partial N_9}{\partial s} = \frac{1}{8}(1-s)(1-t^2)(1-2r+r^2)$$

$$\frac{\partial N_{10}}{\partial s} = \frac{1}{4}(1-s-t+st)(1-r^2)$$

$$\frac{\partial N_{11}}{\partial s} = \frac{1}{4}(1+s-t-st)(1-r^2)$$

$$\frac{\partial N_{12}}{\partial s} = \frac{1}{4}(1+s+t+st)(1-r^2)$$

$$\frac{\partial N_{13}}{\partial s} = \frac{1}{4}(1-s+t-st)(1-r^2)$$

$$\frac{\partial N_1}{r} = \frac{1}{16}(1-s)(1-t)[-1(-2-s+sr-t+tr)+(1-r)(s+t)]$$

$$\frac{\partial N_2}{r} = \frac{1}{16}(1+s)(1-t)[-1(-2+s-sr-t+tr)+(1-r)(-s+t)]$$

$$\frac{\partial N_3}{r} = \frac{1}{16}(1+s)(1+t)[-1(-2+s-sr+t-tr)+(1-r)(-s-t)]$$

$$\frac{\partial N_4}{r} = \frac{1}{16}(1-s)(1+t)[-1(-2-s+sr+t-tr)+(1-r)(s-t)]$$

$$\frac{\partial N_5}{r} = \frac{1+2r}{2}; \quad \frac{\partial N_6}{r} = \frac{1}{4}(1-s^2)(1-t)(-1+r); \quad \frac{\partial N_7}{r} = \frac{1}{4}(1+s)(1-t^2)(-1+r)$$

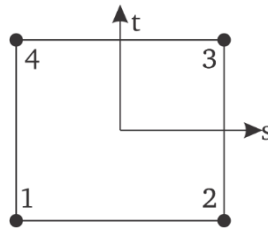
$$\frac{\partial N_8}{r} = \frac{1}{4}(1-s^2)(1+t)(-1+r); \quad \frac{\partial N_9}{r} = \frac{1}{4}(1-s)(1-t^2)(-1+r)$$

$$\frac{\partial N_{10}}{r} = \frac{-r}{2}(1-s-t+st); \quad \frac{\partial N_{11}}{r} = \frac{-r}{2}(1+s-t-st)$$

$$\frac{\partial N_{12}}{r} = \frac{-r}{2}(1+s+t+st); \quad \frac{\partial N_{13}}{r} = \frac{-r}{2}(1-s+t-st)$$

$$\begin{aligned} \frac{\partial N_1}{\partial t} &= \frac{1}{16}(1-s)(1-r)[-1(-2-s+sr-t+tr)+(1-t)(-1+r)] \\ \frac{\partial N_2}{\partial t} &= \frac{1}{16}(1+s)(1-r)[-1(-2+s-sr-t+tr)+(1-t)(-1+r)] \\ \frac{\partial N_3}{\partial t} &= \frac{1}{16}(1+s)(1-r)[+1(-2+s-sr+t-tr)+(1+t)(+1-r)] \\ \frac{\partial N_4}{\partial t} &= \frac{1}{16}(1-s)(1-r)[+1(-2-s+sr+t-tr)+(1+t)(+1-r)] \\ \frac{\partial N_5}{\partial t} &= 0; \frac{\partial N_6}{\partial t} = \frac{-1}{8}(1-s^2)(1-2r+r^2); \frac{\partial N_7}{\partial t} = \frac{-t}{4}(1+s)(1-2r+r^2) \\ \frac{\partial N_8}{\partial t} &= \frac{+1}{8}(1-s^2)(1-2r+r^2); \frac{\partial N_9}{\partial t} = \frac{-t}{4}(1-s)(1-2r+r^2) \\ \frac{\partial N_{10}}{\partial t} &= \frac{1}{4}(-1+s)(1-r^2); \frac{\partial N_{11}}{\partial t} = \frac{1}{4}(-1-s)(1-r^2) \\ \frac{\partial N_{12}}{\partial t} &= \frac{1}{4}(+1+s)(1-r^2); \frac{\partial N_{13}}{\partial t} = \frac{1}{4}(+1-s)(1-r^2) \end{aligned}$$

### C.9. Rectangle 4 nodes (Quad4)



Rectangle 4 nodes – local coordinate (t,s)

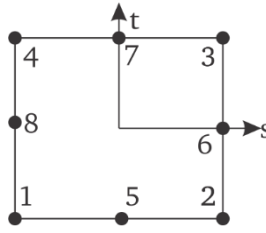
Shape function:

$$N = \left[ \frac{1}{4}(1-s)(1-t)t \quad \frac{1}{4}(1+s)(1-t) \quad \frac{1}{4}(1+s)(1+t) \quad \frac{1}{4}(1-s)(1+t) \right]$$

Derivations:

$$\begin{aligned} \frac{\partial N}{\partial s} &= \left[ -\frac{1}{4}(1-t) \quad \frac{1}{4}(1-t) \quad \frac{1}{4}(1+t) \quad -\frac{1}{4}(1+t) \right] \\ \frac{\partial N}{\partial t} &= \left[ -\frac{1}{4}(1-s) \quad -\frac{1}{4}(1+s) \quad \frac{1}{4}(1+s) \quad \frac{1}{4}(1-s) \right] \end{aligned}$$

### C.10. Rectangle 8 nodes (Quad8)



Rectangle 8 nodes – local coordinate (t,s)

Shape function:

$$N_1 = \frac{1}{4}(1-s)(1-t)(-s-t-1)$$

$$N_2 = \frac{1}{4}(1+s)(1-t)(s-t-1)$$

$$N_3 = \frac{1}{4}(1+s)(1+t)(s+t-1)$$

$$N_4 = \frac{1}{4}(1-s)(1+t)(-s+t-1)$$

$$N_5 = \frac{1}{2}(1-s^2)(1-t)$$

$$N_6 = \frac{1}{2}(1+s)(1-t^2)$$

$$N_7 = \frac{1}{2}(1-s^2)(1+t)$$

$$N_8 = \frac{1}{2}(1-s)(1-t^2)$$

Derivations:

$$\frac{\partial N_1}{\partial s} = \frac{1}{4}(1-t)[-(-s-t-1)-(1-s)]$$

$$\frac{\partial N_2}{\partial s} = \frac{1}{4}(1-t)[(s-t-1)+(1+s)]$$

$$\frac{\partial N_3}{\partial s} = \frac{1}{4}(1+t)[(s+t-1)+(1+s)]$$

$$\frac{\partial N_4}{\partial s} = \frac{1}{4}(1+t)[-(-s+t-1)-(1-s)]$$

$$\frac{\partial N_5}{\partial s} = -s(1-t)$$

$$\frac{\partial N_6}{\partial s} = \frac{1}{2}(1-t^2)$$

$$\frac{\partial N_7}{\partial s} = s(1+t)$$

$$\frac{\partial N_8}{\partial s} = -\frac{1}{2}(1-t^2)$$

$$\frac{\partial N_1}{\partial t} = \frac{1}{4}(1-s)[-(1-t)-(-s-t-1)]$$

$$\frac{\partial N_2}{\partial t} = \frac{1}{4}(1+s)[-(1-t)-(s-t-1)]$$

$$\frac{\partial N_3}{\partial t} = \frac{1}{4}(1+s)[(1+t)+(s+t-1)]$$

$$\frac{\partial N_4}{\partial t} = \frac{1}{4}(1-s)[(1+t)+(-s+t-1)]$$

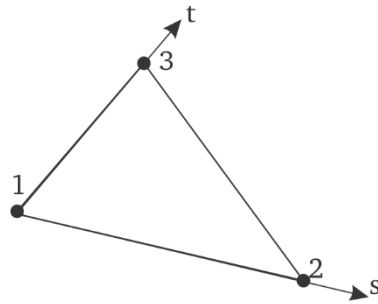
$$\frac{\partial N_5}{\partial t} = -\frac{1}{2}(1-s^2)$$

$$\frac{\partial N_6}{\partial t} = -t(1+s)$$

$$\frac{\partial N_7}{\partial t} = \frac{1}{2}(1-s^2)$$

$$\frac{\partial N_8}{\partial t} = -t(1-s)$$

### C.11. Triangle 3 nodes (Tri3)



Triangle 3 nodes – local coordinate (t,s)

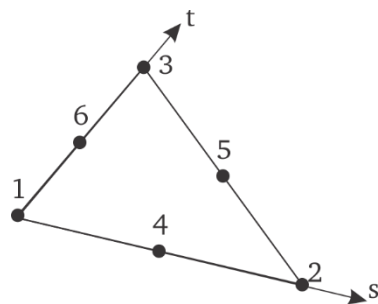
Shape function  $N = [1-s-t \quad s \quad t]$

Derivations:

$$\frac{\partial N}{\partial s} = [-1 \quad 1 \quad 0]$$

$$\frac{\partial N}{\partial t} = [-1 \quad 0 \quad 1]$$

### C.12. Triangle 6 nodes (Tri6)



Triangle 6 nodes – local coordinate (t,s)

Shape function:

$N = [(2v-1)v \quad (2s-1)s \quad (2t-1)t \quad 4sv \quad 4st \quad 4tv]$  where  $v = 1-s-t$

Derivations:

$$\frac{\partial N}{\partial s} = [1-4v \quad 4s-1 \quad 0 \quad 4(v-s) \quad 4t \quad -4t]$$

$$\frac{\partial N}{\partial t} = [1-4v \quad 0 \quad 4t-1 \quad -4s \quad 4s \quad 4(v-t)]$$

## Appendix D: Gaussian points

In Appendix A and B, integrations contain  $\partial N / \partial x, \partial N / \partial y, \partial N / \partial z$  (for 3D models) and  $\partial N / \partial r, \partial N / \partial z$  (for axisymmetric models) need to be calculated. Generally, for a 3D element with the local coordinate system  $(r, t, s)$  and an axisymmetric model with the local coordinate system  $(t, s)$ , these integrations can be calculated by:

$$\begin{bmatrix} \frac{\partial N}{\partial x} \\ \frac{\partial N}{\partial y} \\ \frac{\partial N}{\partial z} \end{bmatrix} = [J^{-1}] \begin{bmatrix} \frac{\partial N}{\partial r} \\ \frac{\partial N}{\partial t} \\ \frac{\partial N}{\partial s} \end{bmatrix} \text{ and } \begin{bmatrix} \frac{\partial N}{\partial r} \\ \frac{\partial N}{\partial z} \end{bmatrix} = [J^{-1}] \begin{bmatrix} \frac{\partial N}{\partial t} \\ \frac{\partial N}{\partial s} \end{bmatrix} \text{ where } [J] \text{ is a Jacobian matrix.}$$

$$\text{For a 3D element } [J] = \begin{bmatrix} \frac{\partial N}{\partial r} \\ \frac{\partial N}{\partial t} \\ \frac{\partial N}{\partial s} \end{bmatrix} \begin{bmatrix} x & y & z \end{bmatrix} \text{ and for a 2D element } [J] = \begin{bmatrix} \frac{\partial N}{\partial t} \\ \frac{\partial N}{\partial s} \end{bmatrix} \begin{bmatrix} r & z \end{bmatrix}.$$

Integrations in Appendix A and B are calculated using the Gaussian point method. For a 3D model, a general form of an integration can be written as  $\iiint_V f\left(\frac{\partial N}{\partial x}, \frac{\partial N}{\partial y}, \frac{\partial N}{\partial z}\right) dV$ . This can be approximated with the Gaussian point method:

$$\iiint_V f\left(\frac{\partial N}{\partial x}, \frac{\partial N}{\partial y}, \frac{\partial N}{\partial z}\right) dV = \sum_{i=1}^{nog} w_i f\left(\frac{\partial N}{\partial r_i}, \frac{\partial N}{\partial t_i}, \frac{\partial N}{\partial s_i}\right) \det(J_i)$$

where  $nog$  is the number of Gaussian points,  $w_i$  is the weight factor.

Similarly, for a 2D element:

$$\iint_R f\left(\frac{\partial N}{\partial r}, \frac{\partial N}{\partial z}\right) dR = \sum_{i=1}^{nog} w_i f\left(\frac{\partial N}{\partial t_i}, \frac{\partial N}{\partial s_i}\right) \det(J_i)$$

The following Gaussian points are used in this dissertation.

### Tet4 and Tet10: 4 Gaussian points

Point	$L_1$	$L_2$	$L_3$	$w_i$
1	0.585410	0.138197	0.138197	0.041667
2	0.138197	0.585410	0.138197	0.041667
3	0.138197	0.138197	0.585410	0.041667
4	0.138197	0.138197	0.138197	0.041667

**Hex8: 8 Gaussian points**

$$g_1 = 1/\sqrt{3}$$

Point	$r$	$t$	$s$	$w_i$
1	$-g_1$	$-g_1$	$-g_1$	1
2	$g_1$	$-g_1$	$-g_1$	1
3	$g_1$	$-g_1$	$g_1$	1
4	$-g_1$	$-g_1$	$g_1$	1
5	$-g_1$	$g_1$	$-g_1$	1
6	$g_1$	$g_1$	$-g_1$	1
7	$g_1$	$g_1$	$g_1$	1
8	$-g_1$	$g_1$	$g_1$	1

**Hex20, Pyra5 and Pyra13: 27 Gaussian points**

$$g_1 = -\sqrt{3}/5; g_2 = 0; g_3 = \sqrt{3}/5$$

$$w_1 = 5/9; w_2 = 8/9; w_3 = 5/9$$

Point	$r$	$t$	$s$	$w_i$
1	$g_1$	$g_1$	$g_1$	$w_1 \times w_1 \times w_1$
2	$g_1$	$g_1$	$g_2$	$w_2 \times w_1 \times w_2$
3	$g_1$	$g_1$	$g_3$	$w_1 \times w_1 \times w_3$
4	$g_1$	$g_2$	$g_1$	$w_1 \times w_2 \times w_1$
5	$g_1$	$g_2$	$g_2$	$w_1 \times w_2 \times w_2$
6	$g_1$	$g_2$	$g_3$	$w_1 \times w_2 \times w_3$
7	$g_2$	$g_1$	$g_1$	$w_2 \times w_1 \times w_1$
8	$g_2$	$g_1$	$g_2$	$w_2 \times w_1 \times w_2$
9	$g_2$	$g_1$	$g_3$	$w_2 \times w_1 \times w_3$
10	$g_2$	$g_2$	$g_1$	$w_2 \times w_2 \times w_1$
11	$g_2$	$g_2$	$g_2$	$w_2 \times w_2 \times w_2$
12	$g_2$	$g_2$	$g_3$	$w_2 \times w_2 \times w_3$
13	$g_3$	$g_1$	$g_1$	$w_3 \times w_1 \times w_1$
14	$g_3$	$g_1$	$g_2$	$w_3 \times w_1 \times w_2$
15	$g_3$	$g_1$	$g_3$	$w_3 \times w_1 \times w_3$
16	$g_3$	$g_2$	$g_1$	$w_3 \times w_2 \times w_1$
17	$g_3$	$g_2$	$g_2$	$w_3 \times w_2 \times w_2$
18	$g_3$	$g_2$	$g_3$	$w_3 \times w_2 \times w_3$
19	$g_3$	$g_3$	$g_1$	$w_3 \times w_3 \times w_1$
20	$g_3$	$g_3$	$g_2$	$w_3 \times w_3 \times w_2$
21	$g_3$	$g_3$	$g_3$	$w_3 \times w_3 \times w_3$
22	$g_1$	$g_3$	$g_1$	$w_1 \times w_3 \times w_1$
23	$g_1$	$g_3$	$g_2$	$w_1 \times w_3 \times w_2$
24	$g_1$	$g_3$	$g_3$	$w_1 \times w_3 \times w_3$
25	$g_2$	$g_3$	$g_1$	$w_2 \times w_3 \times w_1$
26	$g_2$	$g_3$	$g_2$	$w_2 \times w_3 \times w_2$
27	$g_2$	$g_3$	$g_3$	$w_2 \times w_3 \times w_3$

---

**Prism6 and Prism15: 9 Gaussian points**

Point	$t$	$s$	$r$	$w_i$
1	$1/6$	$1/6$	$-0.7746$	$0.0926$
2	$1/6$	$2/3$	$-0.7746$	$0.0926$
3	$2/3$	$1/6$	$-0.7746$	$0.0926$
4	$1/6$	$1/6$	$0$	$0.1482$
5	$1/6$	$2/3$	$0$	$0.1482$
6	$2/3$	$1/6$	$0$	$0.1482$
7	$1/6$	$1/6$	$0.7746$	$0.0926$
8	$1/6$	$2/3$	$0.7746$	$0.0926$
9	$2/3$	$1/6$	$0.7746$	$0.0926$

**Tri3 and Tri6: 3 Gaussian points**

Point	$t$	$s$	$w_i$
1	$1/6$	$1/6$	$1/6$
2	$2/3$	$1/6$	$1/6$
3	$1/6$	$2/3$	$1/6$

**Quad4 and Quad8: 4 Gaussian points**

Point	$t$	$s$	$w_i$
1	$0.57735$	$0.57735$	$1$
2	$0.57735$	$-0.57735$	$1$
3	$-0.57735$	$0.57735$	$1$
4	$-0.57735$	$-0.57735$	$1$

---

---

## References

---

- A. Bloomer, & S. Currie. (2001). *Effects of geothermal induced subsidence*. Paper presented at the New Zealand Geothermal Workshop 2001, New Zealand.
- Abidin, H. Z., Andreas, H., Gumilar, I., Fukuda, Y., Pohan, Y. E., & Deguchi, T. (2011). Land subsidence of Jakarta (Indonesia) and its relation with urban development. *Natural Hazards*, 59(3), 1753. doi:10.1007/s11069-011-9866-9
- Abousleiman, Y., Cheng, A. H.-D., Cui, L., Detournay, E., & Roegiers, J.-C. (1996). Mandel's problem revisited. *Géotechnique*, 46(2), 187-195. doi:10.1680/geot.1996.46.2.187
- ASTM-D2435. (2011). Standard Test Methods for One-Dimensional Consolidation Properties of Soils Using Incremental Loading. In. ASTM International.
- ASTM-D3080. (2011). Standard Test Method for Direct Shear Test of Soils Under Consolidated Drained Conditions. In.
- ASTM/D4186M-12e1. (2014). Standard Test Method for One-Dimensional Consolidation Properties of Saturated Cohesive Soils Using Controlled-Strain Loading. In. West Conshohocken, PA, 2012: ASTM International.
- ASTM/D7181-11. (2011). Method for Consolidated Drained Triaxial Compression Test for Soils. In.
- Barron, R. A. (1948). Consolidation of Fine-Grained Soils by Drain Wells. *Transactions of the American Society of Civil Engineers*, 113(1), 718-742.
- Been, K., & Sills, G. C. (1981). Self-weight consolidation of soft soils: an experimental and theoretical study. *Géotechnique*, 31(4), 519-535. doi:10.1680/geot.1981.31.4.519
- Bergado, D. T. (1996). *Soft ground improvement : in lowland and other environments*. New York, N.Y.: ASCE Press.
- Biot, M. (1956). General solutions of the equations of elasticity and consolidation for a porous material. *J. appl. Mech*, 23(1), 91-96.
- Biot, M. A. (1941). General theory of three-dimensional consolidation. *Journal of Applied Physics*, 12(2), 155-164.
- Bo, M. W., Arulrajah, A., Horpibulsuk, S., & Leong, M. (2015). Quality management of prefabricated vertical drain materials in mega land reclamation projects: A case study. *SOILS AND FOUNDATIONS*, 55(4), 895-905. doi:<https://doi.org/10.1016/j.sandf.2015.06.019>
- Butcher, J. C. (2016). *Numerical methods for ordinary differential equations* (Third edition. ed.). Chichester, West Sussex, United Kingdom: Wiley.
- Chai, J.-C., Shen, S.-L., Miura, N., & Bergado, D. T. (2001). Simple Method of Modeling PVD-Improved Subsoil. *Journal of Geotechnical and Geoenvironmental Engineering*, 127(11), 965-972. doi:doi:10.1061/(ASCE)1090-0241(2001)127:11(965)
- Chai, J., & Carter, J. P. (2011). *Deformation analysis in soft ground improvement*. Dordrecht: Springer.
- Chai, J., Horpibulsuk, S., Shen, S., & Carter, J. P. (2014). Consolidation analysis of clayey deposits under vacuum pressure with horizontal drains. *Geotextiles and Geomembranes*, 42(5), 437-444. doi:<https://doi.org/10.1016/j.geotexmem.2014.07.001>
- Chen, B., Gong, H., Lei, K., Li, J., Zhou, C., Gao, M., . . . Lv, W. (2019). Land subsidence lagging quantification in the main exploration aquifer layers in

- 
- Beijing plain, China. *International Journal of Applied Earth Observation and Geoinformation*, 75, 54-67. doi:<https://doi.org/10.1016/j.jag.2018.09.003>
- Cheng, A. H. D. (2016). *Poroelasticity*. New York, NY: Springer Science+Business Media.
- Colazas, X. C., & Strehle, R. W. (1995). Chapter 6 Subsidence in the Wilmington Oil Field, Long Beach, California, USA. In G. V. Chilingarian, E. C. Donaldson, & T. F. Yen (Eds.), *Developments in Petroleum Science* (Vol. 41, pp. 285-335): Elsevier.
- Detournay, E., & Cheng, A. H.-D. (1993). Fundamentals of poroelasticity. *Chapter 5 in Comprehensive Rock Engineering: Principles, Practice and Projects, II*, 113-171.
- Detournay, E., & Cheng, A. H. D. (1993). 5 - Fundamentals of Poroelasticity. In C. Fairhurst (Ed.), *Analysis and Design Methods* (pp. 113-171). Oxford: Pergamon.
- Diersch, H. J. G., Bauer, D., Heidemann, W., Rühaak, W., & Schätzl, P. (2011). Finite element modeling of borehole heat exchanger systems: Part 2. Numerical simulation. *Computers & Geosciences*, 37(8), 1136-1147. doi:<https://doi.org/10.1016/j.cageo.2010.08.002>
- Galloway, D. L., & Burbey, T. J. (2011). Review: Regional land subsidence accompanying groundwater extraction. *Hydrogeology Journal*, 19(8), 1459-1486. doi:10.1007/s10040-011-0775-5
- Hansbo, S. (1976). Consolidation of clay by band-shaped prefabricated drains. *Ground Engineering*, 12(5), 21.
- Hansbo, S. (1981). *Consolidation of fine-grained soils by prefabricated drains*. Paper presented at the Proceedings of the 10th international conference on soil mechanics and foundation engineering, Stockholm.
- Hiep, H., & Chung, S. G. (2018). Back-analysis of geotechnical parameters on PVD-improved ground in the Mekong Delta. *Geotextiles and Geomembranes*, 46(4), 402-413. doi:<https://doi.org/10.1016/j.geotexmem.2018.03.005>
- Hird, C. C., Pyrah, I. C., & Russel, D. (1992). Finite element modelling of vertical drains beneath embankments on soft ground. *Géotechnique*, 42(3), 499-511. doi:10.1680/geot.1992.42.3.499
- Indraratna, B., & Redana, I. W. (1997). Plane-Strain Modeling of Smear Effects Associated with Vertical Drains. *Journal of Geotechnical and Geoenvironmental Engineering*, 123(5), 474-478. doi:doi:10.1061/(ASCE)1090-0241(1997)123:5(474)
- Indraratna, B., Sathanathan, I., Rujikiatkamjorn, C., & Balasubramaniam, A. S. (2005). Analytical and Numerical Modeling of Soft Soil Stabilized by Prefabricated Vertical Drains Incorporating Vacuum Preloading. *International Journal of Geomechanics*, 5(2), 114-124. doi:doi:10.1061/(ASCE)1532-3641(2005)5:2(114)
- Jacob, C. E. (1940). On the flow of water in an elastic artesian aquifer. *Eos, Transactions American Geophysical Union*, 21(2), 574-586.
- Kumarage, P. I., & Gnanendran, C. T. (2019). Long-term performance predictions in ground improvements with vacuum assisted Prefabricated Vertical Drains. *Geotextiles and Geomembranes*, 47(2), 95-103. doi:<https://doi.org/10.1016/j.geotexmem.2018.11.002>
- Leake, S., & Galloway, D. (2007). *MODFLOW Ground-water Model: User Guide to the Subsidence and Aquifer-system Compaction Package (SUB-WT) for Water-table Aquifers*.

- Liu, K. W., & Rowe, R. K. (2015). Numerical modelling of prefabricated vertical drains and surcharge on reinforced floating column-supported embankment behaviour. *Geotextiles and Geomembranes*, 43(6), 493-505. doi:<https://doi.org/10.1016/j.geotexmem.2015.05.006>
- Nguyen, B.-P., & Kim, Y.-T. (2019). Radial consolidation of PVD-Installed normally consolidated soil with discharge capacity reduction using large-strain theory. *Geotextiles and Geomembranes*, 47(2), 243-254. doi:<https://doi.org/10.1016/j.geotexmem.2019.01.008>
- Nguyen, C.-O., Tran, T.-T., & Dao, V.-T. T. (2019). Consolidation Analysis with Application of Constant Rate of Strain Consolidation Tests for Vietnam Clays. *Geotechnical and Geological Engineering*. doi:10.1007/s10706-019-01068-9
- Nguyen, Q. T. (2016). The Main Causes of Land Subsidence in Ho Chi Minh City. *Procedia Engineering*, 142, 334-341. doi:<https://doi.org/10.1016/j.proeng.2016.02.058>
- Pham, H. T., Rühaak, W., Ngo, D. H., Nguyen, O. C., & Sass, I. (2019). Fully coupled analysis of consolidation by prefabricated vertical drains with applications of constant strain rate tests: Case studies and an open-source program. *Geotextiles and Geomembranes*. doi:<https://doi.org/10.1016/j.geotexmem.2019.12.009>
- Pham, H. T., Rühaak, W., Schulte, D., & Sass, I. (2019). Application of the Vimore-Taylor concept for fully coupled models of consolidation by prefabricated vertical drains. *Computers and Geotechnics*, 116, 103201. doi:<https://doi.org/10.1016/j.compgeo.2019.103201>
- Pham, H. T., Rühaak, W., Schuster, V., & Sass, I. (2019). Fully hydro-mechanical coupled Plug-in (SUB+) in FEFLOW for analysis of land subsidence due to groundwater extraction. *SoftwareX*, 9, 15-19. doi:<https://doi.org/10.1016/j.softx.2018.11.004>
- Phien-wej, N., Giao, P. H., & Nutalaya, P. (2006). Land subsidence in Bangkok, Thailand. *Engineering Geology*, 82(4), 187-201. doi:<https://doi.org/10.1016/j.enggeo.2005.10.004>
- Poland, J. F. (1984). Guidebook to studies of land subsidence due to ground-water withdrawal.
- Radhika, B. P., Krishnamoorthy, A., & Rao, A. U. (2017). A review on consolidation theories and its application. *International Journal of Geotechnical Engineering*, 1-7. doi:10.1080/19386362.2017.1390899
- Rivera, A., Ledoux, E., & De Marsily, G. (1991). Nonlinear modeling of groundwater flow and total subsidence of the Mexico City aquifer-aquitard system. In *Land subsidence* (Vol. 200, pp. 45-58): IAHS Publ.
- Rixner, J., Kramer, S., & Smith, A. (1986). Prefabricated vertical drains, Vol. II: Summary of research effort. *Research Rep. No. FHWA/RD-86*, 169.
- Rühaak, W., Bense, V. F., & Sass, I. (2014). 3D hydro-mechanically coupled groundwater flow modelling of Pleistocene glaciation effects. *Computers & Geosciences*, 67, 89-99. doi:<https://doi.org/10.1016/j.cageo.2014.03.001>
- Rühaak, W., Pei, L., Heldmann, C.-D., & Sass, I. (2017). Thermo-Hydro-Mechanical-Chemical Coupled Modeling of a Geothermally Used Fractured Limestone. *International Journal of Rock Mechanics and Mining Sciences*, 100, 40-47. Retrieved from <http://tubiblio.ulb.tu-darmstadt.de/89784/>

- 
- Rujikiatkamjorn, C., & Indraratna, B. (2006). Three-Dimensional Numerical Modeling of Soft Soil Consolidation Improved by Prefabricated Vertical Drains. In *Ground Modification and Seismic Mitigation*.
- Rujikiatkamjorn, C., Indraratna, B., & Chu, J. (2008). 2D and 3D Numerical Modeling of Combined Surcharge and Vacuum Preloading with Vertical Drains. *International Journal of Geomechanics*, 8(2), 144-156. doi:doi:10.1061/(ASCE)1532-3641(2008)8:2(144)
- Sharp, J. M., & Hill, D. W. (1995). Land subsidence along the northeastern Texas Gulf coast: Effects of deep hydrocarbon production. *Environmental Geology*, 25(3), 181-191. doi:10.1007/bf00768547
- Sheahan, T., & Watters, P. (1996). Using an Automated Rowe Cell for Constant Rate of Strain Consolidation Testing. *Geotechnical Testing Journal*, 19(4), 354-363. doi:10.1520/GTJ10713J
- Tajuddin, A., Azhar, S., Yusof, M. F., Bakar, I., Marto, A., Zakaria, M. N., & Abdullah, M. E. (2014). Numerical modeling of prefabricated vertical drain for soft clay using ABAQUS.
- Teatini, P., Ferronato, M., Gambolati, G., & Gonella, M. (2006). Groundwater pumping and land subsidence in the Emilia-Romagna coastland, Italy: Modeling the past occurrence and the future trend. *Water resources research*, 42(1).
- Terzaghi, K. (1943). *Theoretical soil mechanics* (Vol. 18): Wiley Online Library.
- Umehara, Y., & Zen, K. (1980). CONSTANT RATE OF STRAIN CONSOLIDATION FOR VERY SOFT CLAYEY SOILS. *SOILS AND FOUNDATIONS*, 20(2), 79-95. doi:10.3208/sandf1972.20.2\_79
- Verruijt, A. (2016). *PoroElasticity*: <http://geo.verruijt.net/>.
- Walker, R. T. (2011). Vertical drain consolidation analysis in one, two and three dimensions. *Computers and Geotechnics*, 38(8), 1069-1077.
- Wissa, A. (1971). Consolidation at constant rate of strain. *Journal of Soil Mechanics & Foundations Div.*
- Ye, S., Luo, Y., Wu, J., Yan, X., Wang, H., Jiao, X., & Teatini, P. (2016). Three-dimensional numerical modeling of land subsidence in Shanghai, China. *Hydrogeology Journal*, 24(3), 695-709. doi:10.1007/s10040-016-1382-2
- Zhou, W.-H., Lok, T. M.-H., Zhao, L.-S., Mei, G.-x., & Li, X.-B. (2017). Analytical solutions to the axisymmetric consolidation of a multi-layer soil system under surcharge combined with vacuum preloading. *Geotextiles and Geomembranes*, 45(5), 487-498. doi:<https://doi.org/10.1016/j.geotexmem.2017.06.003>



---

---

## Curriculum Vitae

---

### PHAM, HUNG TIEN

Born on 20.07.1988 in Hai Duong, Vietnam

#### EDUCATION

- Dec 2015 – May 2019* PhD student  
Institute of Applied Geosciences- Department of Geothermal Science and Technology, Technische Universität Darmstadt
- Aug 2013 – April 2014* Exchange student  
LWI Institute - TU Braunschweig – Germany
- Sep 2006 – April/2011* Master of Hydraulic Construction Engineering  
Hanoi Water Resources University, Hanoi, Vietnam
- Sep 2011 – Sep 2014* Bachelor of Hydraulic Construction Engineering  
Hanoi Water Resources University, Hanoi, Vietnam

---

#### WORK EXPERIENCE

- April 2011 – Now* Structural Engineer, Dams Engineer (Full-time and freelancer)  
Power Engineering Consulting Company I (PECC1), Hanoi, Vietnam

- 
- COMPUTER SKILLS** CAD: AutoCAD (2D, 3D)  
GIS: ArcGIS  
Finite element software: FeFlow, Ansys, Flac3D, Plaxis  
Coding: C++ (Qt, OpenGL), MATLAB

- 
- LANGUAGE SKILLS** Vietnamese (mother tongue)  
English (Professional proficiency)  
German (Elementary proficiency)

- 
- AWARDS** 2008: The second prize in curriculum theory of Vietnam Student Olympic  
2013: Exceed scholarship for Sustainable Water Management  
2015: Full DAAD PhD scholarship in TU Darmstadt